Summer 7-1-2017

Viscoelastic Effects in Carbon Fiber Reinforced Polymer Strain Energy Deployable Composite Tape Springs

Elisa C. Borowski
University of New Mexico

Elisa Claire Borowski

Candidate

Civil Engineering

Department

This thesis is approved, and it is acceptable in quality and form for publication:

Approved by the Thesis Committee:

Dr. Mahmoud Reda Taha , Chairperson

Dr. Timothy Ross

Dr. Thomas Murphey

VISCOELASTIC EFFECTS IN CARBON FIBER REINFORCED POLYMER STRAIN ENERGY DEPLOYABLE COMPOSITE TAPE SPRINGS

by

ELISA CLAIRE BOROWSKI

BACHELOR OF ARTS, ANTHROPOLOGY AND ENGLISH

THESIS

Submitted in Partial Fulfillment of the
Requirements for the Degree of

Master of Science
Civil Engineering

The University of New Mexico
Albuquerque, New Mexico

July, 2017

ACKNOWLEDGMENTS

I would like to express my gratitude to the many individuals who have contributed to my successful completion of this thesis. First and foremost, I would like to thank my graduate advisor and committee chair, Dr. Mahmoud Reda Taha, for his continuous guidance and support throughout the entirety of my master's level education. Thank you for welcoming me into the field of engineering, for presenting me with a vast array of unique opportunities from which to expand my knowledge and experiences, and for helping me to identify a personally meaningful role within the field.

I would like to thank my thesis committee members, Dr. Timothy Ross and Dr. Thomas Murphey. Thank you for the time, commitment, and insightful feedback you have offered to support my thesis research. In addition, I would like to acknowledge Dr. Murphey for the outstanding strides he has made in the development of deployable high strain composites and to express my gratitude for his approachability and willingness to converse upon this research.

I would like to thank my collaborators at the Air Force Research Laboratory in Albuquerque, NM for contributing their materials, equipment, and time in support of this research. I would like to thank Michael Peterson for the time he has dedicated to the filming of the deployment experiments reported in this thesis.

I would like to thank my teammates, Amy Garner and Dr. Arafat Khan, for their contributions to the advancement of our research and understanding of deployable aerospace composites. I would like to thank Amy Garner for her assistance with the epoxy stress relaxation experiments and Dr. Khan for his help developing the model subroutine. Thank you to Kenny Martinez and my colleagues at the University of New Mexico (UNM)

Structures Laboratory for training me to use equipment, assisting me with experimental setups, and providing me with the tools necessary to complete the experiments. I would like to thank Jason Church at the UNM Mechanical Engineering Machine Shop and James Love for machining various testing apparatuses to support this research. Thank you also to everyone working in the Civil Engineering Information Technologies department for applying their expertise to provide me with continuous access to necessary computational tools and equipment.

I would like to thank my mentor, Dr. Pania Newell, for her support and guidance and for continually pushing me to reach for the stars. Thank you to my dear parents and brothers for their unfaltering confidence in my abilities, their endless encouragement, and for inspiring me to use my education to make a difference in the world. I would like to thank my loving boyfriend, Hans Weeks, for his continuous support, patience, and humor. Finally, thank you to all of my family, friends, and colleagues who have supported me throughout this journey.

This research was supported by funding from the Air Force Office of Scientific Research (AFOSR) Award #FA9550-14-1-0021 and the New Mexico Space Grant Graduate Research Fellowship. I would like to express my gratitude for this support.

PREFACE

The following publications have been co-authored by the M.S. student during the course of study.

Journal Articles

[1] **Borowski, E.**, Soliman, E., Khan, A., and Reda Taha, M. M. "Stowage and Deployment of a Viscoelastic Orthotropic Carbon Fiber Composite Tape Spring," *AIAA Journal of Spacecraft and Rockets*, In Review, May 2017.

[2] Khan, A., **Borowski, E.**, Soliman, E., and Reda Taha, M. M. "Examining Energy Dissipation of Deployable Aerospace Composites Using Matrix Viscoelasticity," *ASCE Journal of Aerospace Engineering*, Accepted, April 2017.

[3] **Borowski, E.**, Soliman, E., Kandil, U., and Reda Taha, M. M. "Interlaminar Fracture Toughness of CFRP Laminates Incorporating Multi-Walled Carbon Nanotubes," *Polymers*, Vol. 7, No. 6, pp. 1020 – 1045, June 2015.

Technical Reports

[1] **Borowski, E.** and Newell, P. "Numerical Investigation of Fracture in Geomaterials," *Sandia Technical Report* SAND2015-7325, August 2015.

Conference Articles

[1] **Borowski, E.**, Khan, A., and Reda Taha, M. M. "Identifying Critical Design Variables and Domains for Design Optimization of Deployable Tape Springs for Controlled Deployment," *American Society for Composites 31st Technical Conference Proceedings*, Williamsburg, VA, September 2016.

[2] Khan, A., **Borowski, E.**, and Reda Taha, M. M. "Dynamic Deployment of Composite Tape Springs," *American Society for Composites 31st Technical Conference Proceedings*, Williamsburg, VA, September 2016.

[3] Taha, E., **Borowski, E.**, Kandil, U., Awadallah, A., Aboul-Enein, A., and Reda Taha, M. M. "Carbon Nanotubes to Improve Short Glass Fiber Composites," *American Society for Composites 31st Technical Conference Proceedings*, Williamsburg, VA, September 2016.

[4] Newell, P., **Borowski, E.**, Major, J. R., and Eichhubl, P. "Numerical Investigations of Fracture Propagation in Geomaterials," *AGU Fall Meeting*, San Francisco, CA, December 2015.

[5] Khan, A., **Borowski, E.**, Soliman, E., and Reda Taha, M. M. "Viscoelastic Energy Dissipation of Deployable Composite Structures," *10th International Conference on Composite Science and Technology Proceedings*, Lisbon, Portugal, September 2015.

[6] **Borowski, E.**, Aboubakr, S., Soliman, E., and Reda Taha, M. M. "Fracture Toughness of Carbon Fiber Laminates Including Carbon Nanotubes," *American Society for Composites 29th Technical Conference Proceedings*, San Diego, CA, September 2014.

In Preparation

[1] **Borowski, E.**, Soliman, E., Khan, A., and Reda Taha, M. M. "Examining Viscoelastic Effects of Long-Term Stowage on Deployable Aerospace Composites," *ASCE Journal of Aerospace Engineering*. In preparation to be submitted June 2017.

[2] **Borowski, E.**, Soliman, E., Vugrin, E., and Reda Taha, M. M. "Infrastructure Resilience: Definitions, Quantification Methods, and Research Needs (A Critical Review)," *ASCE Natural Hazards Review*. In preparation to be submitted July 2017.

VISCOELASTIC EFFECTS IN CARBON FIBER REINFORCED POLYMER STRAIN ENERGY DEPLOYABLE COMPOSITE TAPE SPRINGS

by

Elisa Claire Borowski

B.A., Anthropology and English, University of New Mexico, 2010

M.S., Civil Engineering, University of New Mexico, 2017

ABSTRACT

Strain energy deployable composite structures are of great importance to the aerospace community due to their light weight, high stiffness, impressive flexibility, compact stowage configuration, and ability to self-deploy. These attributes make composite deployable hinges ideal for aerospace applications that can benefit from decreased payload and decreased structural complexity through a reduction in deployment parts. However, successful application of these deployable structures requires an in-depth understanding of their mechanical behavior throughout stowage and deployment processes. Upon release from a high strain stowage configuration, high deployment accelerations caused by a great amount of stored strain energy could potentially damage the structure or detach its supported accessories. Alternatively, insufficiently limited amounts of stored strain energy could result in the failure of the structure to achieve complete deployment. The mechanical response of the deployable composite during stowage contributes considerably to its deployment mechanics. The viscoelastic properties of the composite material affect the

amount of stored strain energy in the structure during stowage as a function of time, further complicating the predictability of the structure's deployment response. For these reasons, mechanical and numerical investigations are required prior to utilizing these structures in practical applications. Many challenges, including high costs and complex environmental controls, must be overcome if one is to recreate realistic space-like conditions in a laboratory setting in order to obtain a predictive measure of the structure's deployment response following stowage. Therefore, accurate and reliable numerical simulations depicting the mechanical response of these deployable composite structures are becoming increasingly desirable within the aerospace structures community.

The research presented herein provides a methodology for numerically simulating the stowage and deployment mechanics of a three-layer carbon fiber reinforced polymer composite strain energy deployable hinge using finite element modeling. Simulations are created using Abaqus/CAE software paired with a user-defined material subroutine. Simulation input parameters are determined through a series of material testing procedures. The model is validated using a novel experimental procedure performed with a tabletop testing apparatus designed specifically to capture the mechanical response of a deployable hinge structure throughout the phases of high strain stowage and dynamic deployment.

TABLE OF CONTENTS

LIST OF FIGURES

LIST OF TABLES

CHAPTER 1 INTRODUCTION

Deployable structures are commonly used in aerospace missions in an attempt to reduce payload and costs. These goals are achieved by the ability of the deployable structure to be packed into a small stowage volume during launch and its ability to self-deploy once the spacecraft reaches orbit to expose large surface areas that can house accessories necessary to the space mission, including solar panels, mirrors, cameras, and sensors. A common prototype of this variety of deployable mechanism is known as a *tape spring*, the design of which is based on the idea of a carpenter measuring tape. The typical shape of a deployable tape spring is shown in Figure 1.1.

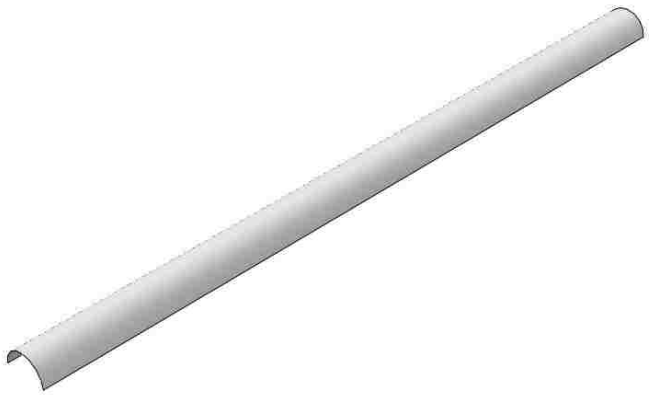

Figure 1.1: Typical shape of a deployable tape spring.

A tape spring is a long strip of an open cylindrical shell. Its thickness dimension is far less than its width or length, and it has a transversally curved cross-section. The thinness of the structure creates a highly geometrically-nonlinear response during bending and provides the tape spring with the capacity to undergo recoverable elastic deformation. A tape spring functions as a strain energy deployable mechanism, because it can easily be

folded or rolled up by flattening its cross-sectional curvature, and in the process, elastic strain energy is accumulated in the tape spring which can later be released to achieve deployment. Once the deformed tape spring is freed from its constraint in the stowed configuration, it can quickly self-actuate deployment and self-latch back into its original straight configuration. Many composite tape springs are *bistable*, meaning they are stable both in their stowage configuration and in their deployed configuration. Therefore, during stowage they are self-contained in a higher-energy yet stable state and do not require additional constraints or latching mechanisms to maintain this geometry.

There are a great number of benefits that come from using deployable tape spring components in aerospace applications, including lightness, high stiffness-to-weight ratios, increased stabilization, and reduced cost and complication of design. Tape spring technology has been applied to inflatable, motorized, and mechanically jointed structures, booms, hinges, extendable masts, antennas, telescopes, space optics, solar sails, sunshades, solar arrays, photovoltaic cells, radar arrays, reflectors, shape memory structures, solar space power systems, radiators, radio frequency reflectors, and other components of typically small satellites.

Traditionally composed of metallic materials, tape springs are now usually fabricated of composite laminates. A *composite* is a type of material that consists of at least two constituent materials that are disparate at the microscopic level. A commonly-used composite material for aerospace applications is a *fiber reinforced polymer* (FRP), which consists of a polymer matrix, such as a thermoset epoxy resin, reinforced by fibers often composed of glass or carbon. The benefits of fabricating tape springs with FRP composite materials include that it increases mass efficiency, increases the stiffness-to-mass ratio,

provides greater flexibility and customization, provides superior thermal expansion properties, increases strength and stiffness, decreases mass and packing volume, and enables high strain deformations without failure. The low coefficient of thermal expansion in *carbon fiber reinforced polymers* (CFRP) is important for aerospace applications, because in space there is a high likelihood that structures will be exposed to thermal gradients and thermal shock caused by the single-sided thermal loading radiation environment, shadowing of sub-systems, and Earth eclipses.

1.1 CHALLENGES OF STRAIN ENERGY DEPLOYABLE STRUCTURES

Due to the nature of their aerospace applications, tape springs are often stowed and stored for long durations (typically, a minimum of six months) while being exposed to changing temperature cycles. This can be especially problematic for FRP composite tape springs, because polymers are *viscoelastic* materials, meaning their material characteristics change with time and temperature. For this reason, the deployment behavior of FRP tape springs can be considerably affected by their stowage history. Specifically, the high-strain stowage configuration that these viscoelastic tape springs undergo supports energy dissipation in the structure over time. Furthermore, this phenomenon is accelerated by high temperatures. The energy dissipation caused by the viscoelastic response of the polymer matrix can limit deployment force, deployment moment, and shape precision of the deployed tape spring. Control of deployment is critical for the success of aerospace missions. If deployment happens too quickly, resulting from the sudden release of a great amount of stored strain energy, the tape spring can experience a severe dynamic effect, shock loads, detachment of the accessories originally attached to the tape spring, and potentially, damage to the

structure. If deployment happens too slowly, resulting from the release of a limited amount of stored strain energy or overdamping, the final fully-deployed configuration may never be achieved. Therefore, the goal of this research is to develop a reliable simulation method that can capture completely and accurately the many complexities affecting composite tape spring deployment and can predict the resultant deployment behavior.

As might be expected with any novel and burgeoning technology, the aerospace community has faced some unforeseen anomalies while performing in-flight deployment using high strain composite hinges. To further illustrate the need for accurate, predictive simulations of the stowage and deployment of composite tape springs, the following example is provided. First launched in 2003, the Mars Express spacecraft utilized a Mars Advanced Radar for Subsurface and Ionospheric Sounding (MARSIS) antenna that was composed of three foldable, flattenable tubes fabricated of Kevlar and fiberglass. These tubes or *dipole booms* were able to fold because of their ten high strain composite tape spring hinges which functioned as strain energy deployable mechanisms.

Prior to the deployment of the dipole booms in 2005, uncertainty began to emerge within the research team regarding the accuracy of a damping parameter that had been defined in the deployment simulations which might overestimate the degree of damping that the deployable booms would experience upon deployment. This suggested that the booms would deploy in an unaccounted-for energetic and chaotically dynamic manner that could introduce a degree of buckling that the booms had not been designed to withstand. However, when the first dipole boom deployed on May 4th, 2005, the opposite occurred. The deploying boom halted in partial completion as the last hinge stalled 40° shy of full deployment. It was quickly concluded that this deployment response was the result of a

frozen matrix in the final hinge, which had been kept in shadow and experienced inflight temperatures of $-70°C$ with regions of the hinge reaching less than $-140°C$. Later reports added that the problem was likely exacerbated by aging effects caused by the viscoelastic nature of the matrix which had been stowed in a high strain configuration and exposed to numerous temperature cycles over its two-year stowage period (Mobrem and Adams, 2009). This viscoelastic behavior had not been accounted for in the deployment model. Fortunately, the issue was efficiently resolved in-flight by reorienting the spacecraft to increase the angle of sunlight directed onto the hinge. Within five minutes of sunlight exposure, the boom completed deployment and locked into place. However, the lesson remains clear. Accurate numerical models of deployable composite structures are extremely important to the success and safety of their associated space missions.

1.2 THESIS PURPOSE AND WORKFLOW

The research presented herein includes experimental and numerical investigations to better understand the challenges of tape spring folding, stowage, and deployment and the role that viscoelasticity plays during all three stages of the tape spring life cycle. The objectives of this study are to: (1) characterize the material properties and viscoelastic behavior of a composite tape spring, (2) develop an experimental method to measure the effects of viscoelasticity on the deployment of the composite tape spring, (3) develop a verified and validated finite element model to simulate and predict the effects of viscoelasticity on tape spring deployment, and (4) use the model to predict the effects of viscoelasticity on the deployment of a tape spring containing various hypothetical epoxies representing different rates of relaxation to gain insight into the potential to tailor tape spring deployment.

The research presented herein is significant for its contribution toward developing a greater understanding of the deployment response of viscoelastic composite tape springs in an effort to prevent deployment anomalies from occurring in the future. The motivation for this work stems from recent achievements, challenges, and envisioned potentials regarding the applications of deployable aerospace structures. The main contribution of this work to the aerospace structures community is the development of a framework for analyzing and predicting viscoelastic composite tape spring deployment behavior following stowage. This study is intended for use in future design processes of deployable aerospace structures, because it aims to present a complete, accurate, and adaptable methodology for the simulation of deployable viscoelastic composite shell structures wherein the basic design variables can be adjusted and the resultant deployment behavior will be predicted.

The contents of this thesis are arranged as follows: Chapter 2 presents a review highlighting significant literature contributions to tape spring research to date and summarizes the fundamental theories and concepts necessary to the understanding of viscoelastic deployable composites analysis. Chapter 3 presents the experimental and numerical methods applied in this study. The experimental section describes material characterization techniques, the novel *tape spring stowage and deployment* (TSSD) testing apparatus designed specifically for collecting experimental long-term stowage and deployment measurements, and a summary of the stowage and deployment testing parameters. The numerical section explains the finite element simulation techniques developed to model the stowage and deployment behavior of the tape spring investigated in this study, including the development of a user-defined material subroutine. Chapter 4

presents the experimental and numerical simulation results for the material characterization process, the three testing phases which investigated stowage and deployment, and the hypothetical epoxy study. The chapter also provides a discussion of the research findings and possible inferences from the results. Chapter 5 summarizes the conclusions of the research presented herein, discusses the limitations of the study, and includes recommendations for future investigations.

CHAPTER 2 BACKGROUND

2.1 OVERVIEW OF RELEVANT TAPE SPRING RESEARCH TO DATE

Research on deployable composite tape spring structures first became prevalent in the early 21st century. The following is an overview of some of the experimental and numerical tape spring research deemed relevant to the focus of this thesis. Figure 2.1 presents a timeline of some of the highlights of tape spring research that will be discussed in the following review.

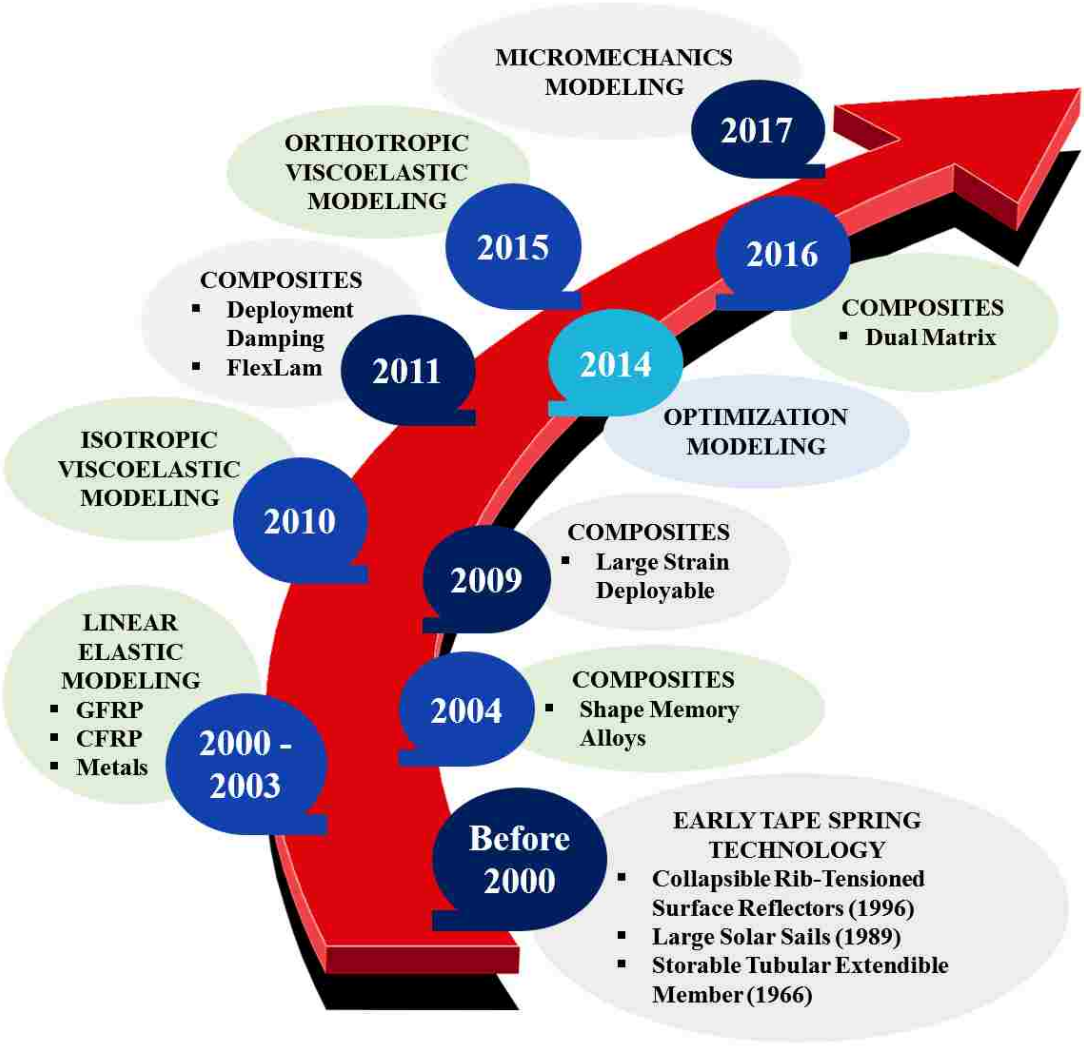

Figure 2.1: Timeline highlighting a few keystones of tape spring research.

2.1.1 EARLY TAPE SPRING TECHNOLOGY

In 1999, a study of the deployment dynamics of tape springs provided a useful review of the preceding history of tape spring structures (Seffen and Pellegrino, 1999). Tape springs in their most rudimentary form, recognized as carpenter measuring tapes, were first fashioned in the late 1920's. One of the earliest deployable boom prototypes, known as a storable tubular extendible member (STEM), is credited to Rimrott (1966). In the late 20th century, two novel tape spring hinge structures were developed for the purpose of actuating the deployment of large space structures: (1) the large solar sail designed by Cambridge Consultants in 1989 and (2) a collapsible rib-tensioned surface (CRTS) reflector developed by the European Space Agency in 1996. These inventions provided the ability of space structures to be launched efficiently in a compact volume and then utilized at full-scale once on orbit. At this time, tape spring structures were typically fabricated of beryllium-copper or steel (Seffen and Pellegrino, 1999).

Early on, the folding and deployment behaviors of metallic *curved* tape springs were also studied (Seffen et al., 2000). Curved tape springs are those which are longitudinally curved in addition to being transversely curved. In this research, the tape springs were used as ribs of a deployable reflector called the collapsible rib-tensioned surface (CRTS) reflector (Seffen et al., 2000).

2.1.2 DEVELOPMENT OF COMPOSITE TAPE SPRINGS

The advancement of *composite* tape springs contributed many additional benefits to deployable aerospace structures, including lightness, greater strength, and impressive stiffness. The discovery of *bistable* composite shells has been credited to Daton-Lovett in

1996 (Iqbal and Pellegrino, 2000). Early investigations into bistability involved a five-ply glass fiber polypropylene laminate with a layup of [+45/-45/0/+45/-45] which produced bistability through its anti-symmetric layup. *Bistability* is the quality of having two stable configurations. For an anti-symmetric tape spring, the two stable configurations are its rolled-up configuration and its straight configuration. Bistable structures cannot transfer between their two configurations without an input of energy, because both configurations represent local minima for potential energy. Flattening and bending simulations of the glass fiber polypropylene tape spring were also performed using Abaqus/Standard, wherein the material was assumed to be linear elastic, and the analysis was performed as static incorporating nonlinear geometry (Iqbal and Pellegrino, 2000).

The effect of composite layups on tape spring equilibrium and stability was studied through the use of slit tube tape springs composed of glass fiber reinforced polymer embedded in a polypropylene matrix (Galletly and Guest, 2000). One tape spring had a symmetric layup of $[+45/-45/0/-45/+45]$, and the other had an anti-symmetric layup of $[+45/-45/0/+45/-45]$. The results showed that both tape springs exhibited the same energy pattern consisting of two equilibrium points (that is, when either the local strain or global strain reached zero) (Galletly and Guest, 2000).

A theoretical analysis of bistability in steel and GFRP tape springs was performed and found that unstressed isotropic (such as steel) tape springs are only stable in their initial configuration, but FRP composite tape springs can be bistable (Guest and Pellegrino, 2006). If the composite is *antisymmetric* with respect to the mid-plane layup, it will be stable in its initial configuration and in a tight coil. If it is *symmetric*, the second stable configuration will be helical or twisted. Theoretical investigations were performed on an

isotropic steel tape spring and on three orthotropic GFRP tape springs made of five layers of uniaxial glass fibers in a polypropylene matrix. Antisymmetric and symmetric layups of $\pm 45°$ and $\pm 40°$ to the longitudinal axis were used to investigate bistability (Guest and Pellegrino, 2006).

Advancing from glass fiber composites, the development of *carbon fiber reinforced polymer* (CFRP) deployable ultra-lightweight booms began in the Institute of Structural Mechanics located in the German Aerospace Center, also known as Deutsches Zentrum für Luft- und Raumfahrt (DLR), for applications of solar sails (Herbeck et al., 2001). The CFRP booms consisted of unidirectional carbon fiber preimpregnated with an unspecified matrix material fabricated with an omega-shaped cross-section. Combinations of 0° and $\pm 45°$ plies were investigated for buckling, out-of-plane bending, in-plane bending, combined bending, and thermal analysis (Herbeck et al., 2001).

Bistable tape springs composed of various materials and configurations were studied to compare carbon fiber used for booms, E-glass used for antennae, and soft matrix antennae (Murphey et al., 2010). Strain energy density plots were created to identify unstable saddle equilibrium points that depicted the maximum strain energy that could be applied to a rolled tape spring before it would unroll (Murphey et al., 2010).

A self-contained linear meter-class deployable (SIMPLE) boom was developed that could deploy using bistable tape springs wherein deployment was initiated by a single burn-wire (Jeon and Murphey, 2011). The tuning of deployment forces was investigated to decrease the impact risk and deployment velocities caused by the continual acceleration and sudden stop upon completion of deployment. Three bistable tape springs were studied and compared. The first was used in the SIMPLE boom and was composed of a one-ply

plain weave 45° CFRP, the second was a three-ply tape spring consisting of a middle layer made of unidirectional 0° glass fiber and outer layers made of plain weave 45° glass fiber, and the third was a two-ply tape spring composed of $\pm 45°$ glass fiber with a nano-silica epoxy resin. For testing, each tape spring was folded parallel to itself to examine its deployment force. The potential of bistable tape springs to support three- and four-beam boom designs was also discussed (Jeon and Murphey, 2011).

Various composite materials have been studied for use in large strain deployable space structures, including carbon fiber composites, metals (such as aluminum, nickel titanium, and steel), and silicon dioxide (such as quarts and glass fiber composites), while two techniques for deployable structures have been defined: (1) distributed strain, *i.e.* deformations that are distributed uniformly throughout the structure, and (2) concentrated strain, *i.e.* flexure hinges concentrating strain into discrete hinge locations (Murphey, 2009). Carbon fiber -based systems have been studied with heat softenable matrix materials such that when heated, the structures could be folded to large strains repeatedly without degradation to their unfolded ability to resist buckling. This technology was cited as being most successfully developed by L'Garde Incorporated, ILC Dover LP, and Composite Technology Development Incorporated. The findings showed that fiberglass reinforced epoxy was four times less efficient than high modulus materials, such as carbon fiber reinforced epoxy (Murphey, 2009).

Ply layup orientations have been studied in woven CFRP tape springs through the incorporation of finite element modeling (Yee et al., 2004). The strain levels in two-ply plain weave tape spring laminates were investigated and compared for two different layups. The results showed that a $[\pm 45°/0°, 90°]$ layup (wherein the $\pm 45°$ ply was on the concave

side of the tape spring) had a lower strain level compared to a $[0°, 90°/\pm 45°]$ layup (wherein the $\pm 45°$ ply was on the convex side of the tape spring) in the case of either bending sense. The moment-rotation behavior has been described mathematically as linear-elastic for minor rotations and constant-moment for extensive rotations (Yee et al., 2004).

A CFRP tape spring structure called an Ultra-Light Mechanism for Advanced Antenna Systems (ULMAAS) has been studied using a finite element simulation to capture the geometrically nonlinear folding and deployment response of the tape spring using ANSYS and PamCrash explicit solver, as well as through experimental investigations (Boesch et al., 2008). The CFRP composite consisted of three to four plies, including eight layups: $[0°, +45°, -45°, 90°]$, $[0°, -45°, +45°, 90°]$, $[0°, +60°, -60°]$, $[0°, -60°, +60°]$, $[0°, +45°, -45°]$, $[0°, -45°, +45°]$, $[90°, +45°, -45°, 0°]$, and $[90°, -45°, +45°, 0°]$. The finite element analysis was used to investigate thermal gradients, and the experimental setup was used to identify weak points in the hinge arrangement through stiffness and deployment testing. The results showed that deployment torque could be reduced through changes in the composite layup (Boesch et al., 2008).

An experimental investigation was performed to study large strain behavior in unidirectional CFRP laminates made of Hexcel IM7 PAN-based carbon fiber pre-impregnated with Hexcel 855-2 toughened epoxy (Sanford et al., 2010). The composite structures were folded into a U-shape and tested in compression between parallel plates to measure the load to failure to consider fiber nonlinearity and geometric structural stabilization of fibers during compression. Bending failure strains of 2.5% were determined and greater than anticipated (Sanford et al., 2010).

The strength of a rollable composite square shell reflector with a doubly-curved surface during stowage and deployment was investigated (Keil and Banik, 2011). Two CFRP layups were compared: $[0°, \pm 45°, 0°]$ and $[\pm 45°, 0°, \pm 45°]$. The intention behind the first configuration was to resist creep effects, but the result was that it was too stiff to be rolled by hand. The second configuration was easier to roll and could achieve a much tighter roll radius. However, it exhibited severe creep effects after just five days of stowage at room temperature. Full-scale testing and finite element simulations were performed (Keil and Banik, 2011).

A characterization of a composite material designed by L'Garde to withstand high strain was performed using unidirectional carbon fibers inside a silicone matrix (Maqueda et al., 2012). The silicone matrix was very soft which allowed for sharp kinks to form in the composite with very minor damage. Fibers relieved the stress through elastic microbuckling. The study investigated the accuracy of the rule of mixtures for determining the moduli in tension, bending, and compression, in addition to Poisson's ratio, and the accuracy of determining strength from a Weibull distribution of a single fiber using simple bundle theory by comparing calculated values to experimental measurements (Maqueda et al., 2012).

A quasi-static explicit finite element model was developed to investigate the effects of inevitable variations in geometric thickness during the manufacture of two-ply $\pm 45°$ plain weave CFRP tube booms with open C-shaped cross-sections (Barbera and Laurenzi, 2015). Results showed that at 100% imperfections, the critical load was 53 N, and a more realistic manufacture imperfection percentage of 10% variation resulted in a critical load of 55 N, which was considered good for nanosatellite applications. The results also showed

that a 5 mm coiling radius for stowage guaranteed integrity of the laminate (Barbera and Laurenzi, 2015).

CFRP slot-tube tape springs, which consisted of a long, straight tube with two or three slots cut into of the surface where the tube was intended to bend, have also been studied (Yee and Pellegrino, 2005). One- or two-ply $\pm 45°$ plain weave CFRP hinges were tested to determine the maximum surface bending strain. The findings showed that in tension, the composite failed at an average strain of 1.0%. The average maximum compressive strain was 0.7%, displaying failure mechanisms of delamination, end brooming, and bedding-in deformation. In bending, the maximum surface strains for a one-ply specimen was 2.8% and for a two-ply was 1.9%. Results also showed that specimens with off-axis fibers could be bent to a much tighter radius than those with on-axis fibers (Yee and Pellegrino, 2005).

Experimental testing of CFRP tape springs with and without a metal hinge insert was performed to investigate deployment precision for optical applications (Black et al., 2006). The CFRP composite tape springs consisted of two plies of woven carbon fiber fabrics oriented at $[+45°/-45°]$ with exception at the hinge location where only a single ply of carbon fiber was used. Deployment repeatability was tested and compared between tape springs with and without the metal strip insert at the hinge location. Both single tape spring 2D bending and 3D tripod configurations were investigated. The use of the metal hinge improved repeatability for the 2D configuration but not for the 3D configuration. The findings also showed that 3D tripod configurations had a more accurate deployment precision compared to single tape springs in 2D bending (Black et al., 2006).

Dual-matrix composite booms have been studied, such as those composed of continuous plain weave $[\pm 45°/0/\pm 45°]$ glass fiber composites with a soft, elastomer matrix (such as silicone) located in specified hinge regions, while a traditional stiff matrix (such as Patz Materials & Technologies epoxy) was used elsewhere, an idea first introduced by L'Garde (Sakovsky et al., 2016). Moment-rotation data was gather experimentally and simulated using finite element analysis. The models closely matched the experimental results with the exception of under-predicting the peak moment and steady state values (Sakovsky et al., 2016).

Shape memory alloys have been applied to composite tape spring technology to develop an actuated composite tape spring, known as a neutrally elastic mechanism (NEM) (Murphey and Pellegrino, 2004). The graphite fiber and epoxy resin composite tape spring maintained neutral stability in all configurations, meaning it was stable in a partially-rolled configuration and static in its entire array of possible positions. The tape springs were fabricated by bonding together two curved laminae such that the convex surfaces were touching and the axes of curvature were perpendicular to one another. The two actuation designs that were investigated included a nickel titanium shape memory alloy and a polyvinylidene fluoride piezoelectric film (Murphey and Pellegrino, 2004).

A deployable elastic composite shape memory alloy reinforced (DECSMAR) structure was developed, composed of CFRP tape springs with embedded shape memory alloy fixtures (Pollard and Murphey, 2006). The composite laminates consisted of $\pm 45°$ plain weave carbon fiber laminae, and investigations included a finite element model to study buckling load and maximum moment. Two nickel titanium wire hinges were

embedded in the fold region of the tape spring to enable fiber strains of 1.48% and shape memory alloy strains of 8.48% (Pollard and Murphey, 2006).

The properties of monolithic articulated concentrated strain elastic structures (MACSES) were investigated using trusses made of CFRP tubes and hinges made of CFRP embedded with shape memory alloy (Pollard, 2007). A finite element model of the MACSES was created to further investigate strength-stability, stiffness, bending, and buckling (Pollard, 2007).

In 2013, a tape spring was designed that made significant strides toward the final FlexLam product that was used for the research conducted in this thesis (Peterson and Murphey, 2013). The tape spring consisted of two unidirectional carbon fiber plies at 0° sandwiched between two plies of $\pm 45°$ glass fiber plain weave, *i.e.* $[\pm 45°/0°/0°/\pm 45°]$. This balanced and symmetric layup was created with the intention that the two different ply types would serve different functions. The unidirectional plies would provide high axial stiffness and bending stiffness while adding benefits of a small coefficient of thermal expansion and creep resistance, but it came with the cost of having a low buckling strength, making it difficult to fold without failure. The off-axis plain weave plies would provide shear stiffness, local bending stiffness, twisting stiffness, and torsional stiffness at the cost of being susceptible to creep and not adding any axial stiffness. Therefore, the combined effect was that the unidirectional plies would contribute to deployment force and axial stiffness so that the creep effects in the plain weave layers would not prevent deployment. Large deformation bending experiments were performed, and bending stiffnesses and failure bending strains were measured (Peterson and Murphey, 2013).

2.1.3 LINEAR ELASTIC TAPE SPRING MODELING

With the use of deployable space structures growing in popularity, along with the complexity and high costs associated with experimental testing of these deployables, the demand for finite element simulations soon became apparent. Early models of deployable tape springs, even those simulating composites, were often defined as linear elastic for simplicity. One such model came from a theoretical investigation of tape springs composed of an unspecified linear elastic material (Seffen, 2001). The study considered the quasi-static moment-rotation response that occurs during an opposite-sense fold using a finite element analysis in Abaqus. An *opposite-sense* fold was defined as one in which the longitudinal curvature formed by the fold is in a sense opposite of the natural transverse curvature of the tape spring. Conversely, an *equal-sense* fold is one in which the longitudinal curvature formed by the fold is in the same sense as the natural transverse curvature of the tape spring. The fold was achieved by applied end couples at each free end of the tape spring. Then a force was applied to push the two ends toward each other. Findings showed that stretching effects in the tape spring were minor compared to bending effects, the transverse curvature throughout the fold region was zero, and if unbalanced loads were applied to the ends of the tape spring, the fold region would travel along the length of the tape spring (Seffen, 2001).

Finite element analysis of CFRP tape springs using Abaqus software included foldable composite structures consisting of a hollow tube with tape spring hinges at its midsection (Yee and Pellegrino, 2003). The hinges were created by cutting three parallel slots into the tube at the desired folding location, and a single tape spring from the tube hinge was modeled in opposite sense bending. The CFRP tube was fabricated using one or

two plies at an orientation of $\pm 45°$. The material was assumed to be linear elastic. Principal strains and shear strains were investigated on the tape spring surface under opposite- and equal-sense bending throughout the bending process for each of the three tape springs made up of one and two plies. The findings showed that for one ply the maximum fiber strain was barely within the material limits, but for two plies it was well-exceeding the limits (Yee and Pellegrino, 2003).

The correction capacity of a deployable tape spring hexapod composed of six rolled steel tape springs was studied using linear elastic finite element modeling and experimental testing (Aridon et al., 2008). The experimental setup of the hexapod prototype was used to measure the tape springs' natural frequencies. Accurate deployment positioning was achieved by eliminating a degree of freedom at the upper junction and by using thicker blades (Aridon et al., 2008).

A finite element analysis of CFRP tape springs was developed to include deployment in addition to folding of two-ply $\pm 45°$ plain weave slot-tube tape spring hinges with two slots (Mallikarachchi and Pellegrino, 2008). The quasi-static finite element model depicted the folding and deployment behavior of the slot-tube hinges. The model assumed a linear elastic material. Moment versus deployment angle were compared between experiment and model to validate the model (Mallikarachchi and Pellegrino, 2008).

A two-ply plain weave CFRP two-slotted tube tape spring hinge was studied using an experimental setup consisting of a CFRP tape spring hinge connected to an aluminum tube (Mallikarachchi and Pellegrino, 2009). The dynamic deployment finite element simulation was verified experimentally to examine deployment angle versus deployment time. The model was used to investigate the margin of safety for fiber failure by finding

the five configurations with the largest mid-plane strain and identifying two critical failure regions for each. The model results showed that although the boom latched immediately following deployment in the gravity simulation, it took four oscillations to latch in the zero-gravity simulation (Mallikarachchi and Pellegrino, 2009).

The design of a one-meter-long boom intended to be folded to encircle a spacecraft was made of two plies of plain weave CFRP (Mallikarachchi and Pellegrino, 2011b). Finite element simulations examined the stowage and deployment behavior and were experimentally validated. Concern was expressed over the harmful dynamic effects upon deployment completion that could potentially damage the tape spring, while on the other hand, slow, significantly damped deployment could stall the tape spring before achieving a completely deployed configuration. Thermal and viscoelastic effects were not taken into account in the simulation (Mallikarachchi and Pellegrino, 2011b).

An experimental and numerical study of a two-ply $\pm 45°$ plain weave CFRP tape spring hinge in folding and deployment was performed using a quasi-static finite element model, which did not include viscoelastic effects (Mallikarachchi and Pellegrino, 2011c). The simulation began with a micromechanical model of the woven laminate, and it resulted in an overestimated snapback, overestimated rotation angle, and underestimated deployment-moment average, possibly due to the lack of viscoelasticity included in the model, as well as experimental tow misalignment and deadband effects in the machine (Mallikarachchi and Pellegrino, 2011c).

Two bistable CFRP tape springs were simulated (one twill and one plain weave) as simplified unit cells (Prigent et al., 2011). In *plain weave* fabric, odd bundles of fibers pass over one and under one of the perpendicular bundles, while in *twill*, odd bundles of fibers

pass over two and under one perpendicular bundle. The finite element simulation was based on a unit cell model to more accurately simulate bending, but it did not simulate creep, sensitivity to low temperatures, or deployment friction (Prigent et al., 2011).

Ultrathin two-slot booms incorporating tape spring hinges composed of two plies of plain weave CFRP were also studied (Mallikarachchi and Pellegrino, 2014a). Deployment experiments indicated that the initial deployment and vibration behaviors were repeatable, but the latching behavior contained noticeable scatter. Quasi-static finite element simulations of folding and deployment were produced to compare deployment, latching attempts, and vibration to that of the experiment. Viscoelasticity, air drag, and acoustic emissions were not investigated (Mallikarachchi and Pellegrino, 2014a).

2.1.4 ISOTROPIC VISCOELASTIC TAPE SPRING MODELING

After the need became apparent for viscoelasticity to be considered in finite element simulations to accurately predict deployment, viscoelastic models began to be developed but were limited to isotropic materials. The modeling of viscoelastic effects on stowage and deployment in tape springs using Abaqus was performed following an experimental study of viscoelastic tape springs made of low density polyethylene (LDPE) at room temperature (Kwok and Pellegrino, 2010). The viscoelastic behavior was explained using rheological mechanical models, and Prony series values were determined through creep tests to achieve isotropic linear viscoelastic finite element modeling in Abaqus (Kwok and Pellegrino, 2010). LDPE was likely a convenient material for a preliminary investigation of finite element modeling of the viscoelastic effects in deployable tape springs, because it is an isotropic material, and the simulation of stress relaxation in isotropic materials is

supported by commercially available finite element software such as Abaqus. However, it is unlikely that this material would be used in real-life deployment applications due to its low structural stiffness and strength. Fiber reinforced polymers are much more common for deployable components in aerospace applications.

The study of viscoelastic effects on folding, stowage, and deployment of LDPE tape springs was continued with stowage experiments in which the tape spring was folded and stowed for 5,000 seconds at temperatures of $15°C$ and $22°C$ (Kwok and Pellegrino, 2011). Deployment experiments were performed in which the tape spring was folded, stowed for 983 seconds at room temperature, and then deployed. The linear viscoelastic behavior was modeled using finite element methods by applying the Prony series of the LDPE material. The Prony series coefficients were found by developing a master curve at $22°C$ and then fitting the Prony series equation to the master curve through application of the Levenberg-Marquardt optimization algorithm. For a linear isotropic material, the Prony series coefficients could be entered directly into Abaqus to model the viscoelastic behavior, and a user subroutine was used to describe the temperature shift factor. The load relaxation versus time plot matched well between the experiment and simulation at both temperatures. However, the transient dynamic response produced some discrepancies (Kwok and Pellegrino, 2011).

Investigations on modeling the effects of viscoelasticity on folding, stowage, and deployment of LDPE tape springs were continued through the simulation of homogeneous linear viscoelastic tape springs using finite element modeling incorporating Prony series coefficients (Kwok and Pellegrino, 2013). The finite element model showed good

agreement with the experimental results, but it was limited to homogenous viscoelastic materials (Kwok and Pellegrino, 2013).

2.1.5 ORTHOTROPIC VISCOELASTIC TAPE SPRING MODELING

Up to this point, very little work had been done on the modeling of orthotropic viscoelastic tape springs in stowage and deployment. One of the first experimental investigations into the effects of composite tape spring material viscoelasticity was performed on a three-ply $\pm 45°$ plain weave CFRP three-slotted tube tape spring hinge (Soykasap, 2009). Deployment was modeled using a quasi-static finite element analysis and verified experimentally to examine deployment angle versus time. To perform the deployment experiment, the tape spring boom was fixed to a steel cylinder with a jubilee clamp on one end and tied with a string into a right angle folded configuration. Once released, deployment was filmed using a high speed video camera positioned against an angular scale to track the tape spring's deployment angle versus time. First, the deployment experiment was performed by releasing the folded tape spring without a stowage period. Then, stowage effects were preliminarily investigated by removing the tape spring from the testing rig, folding it into a right angle, and storing it in a furnace for 3 days at $50℃$. After stowage was completed, the tape spring was reattached to the testing rig to repeat the original deployment experiment at room temperature. The experimental results showed that the deployment frequency had decreased by 21.8%. This result was due to stiffness loss caused by accelerated creep effects (Soykasap, 2009).

The viscoelastic energy dissipation of deployable composite structures was studied via the development of a user-defined material subroutine to simulate stress relaxation in a

plain weave CFRP composite lamina using Abaqus as a first step toward modeling viscoelasticity in CFRP tape springs (Khan et al., 2015). The model results showed good agreement with the stress relaxation tension test performed experimentally (Khan et al., 2015).

The effect of multi-walled carbon nanotubes (MWCNTs) on creep of epoxy in CFRP deployable composite tape springs was investigated through stress relaxation testing of epoxy to determine the Prony series coefficients of both neat epoxy and that incorporating MWCNTs (Garner et al., 2015). A finite element model was developed to simulate stress relaxation in the outer layer of a folded FlexLam tape spring. The results showed that the incorporation of MWCNTs in the tape spring's epoxy matrix increased the amount of stress relaxation response it displayed (Garner et al., 2015).

Deployment after long-term stowage of unidirectional CFRP tape springs composed of outer plies oriented at $\pm 45°$ was also studied (Brinkmeyer et al., 2016). Experiments were performed to compare deployment after a stowage period of zero seconds at $22°C$, after 3 hours at $60°C$, and after 3 hours at $100°C$ in a thermal chamber. The results showed that the time period of deployment increased with longer stowage times and higher temperatures. In cases of excessive stress relaxation, such as for 3 hours at $100°C$, the tape spring was unable to deploy autonomously. However, only one specimen was used for all three tests, wherein it was allowed to recover for one day after room temperature stowage testing and for one week after higher-temperature stowage testing, which may have led to hysteretic effects and inaccuracies (Brinkmeyer et al., 2016).

The dynamic deployment of CFRP composite tape springs was studied by experimental testing in folding and deployment without stowage and the development of a

finite element model to simulate the deployment (Khan et al., 2016). The model and experiment were in close agreement. The model was also used to predict the effects of stress relaxation on deployment following stowage, showing that increased relaxation would delay the initial rate of deployment (Khan et al., 2016).

The possible control of energy dissipation of composite tape springs was studied by applying changes to the matrix viscoelasticity (Khan et al., 2017). First, a finite element model was created to simulate stress relaxation in a stowed tape spring through the use of a user-defined material subroutine. After the model was verified experimentally, two hypothetical epoxies with higher rates of stress relaxation were examined. The results showed that changes in the epoxy did not result in noticeable changes to the amount of strain energy dissipation in the tape spring during stowage (Khan et al., 2017).

2.1.6 MICROMECHANICS MODELING OF TAPE SPRINGS

Another approach to modeling stowage and deployment of orthotropic viscoelastic tape springs was micromechanics modeling. The modeling of viscoelastic effects on the deployment and shape recovery of stowed tape springs was extended to include CFRP materials through the use of micromechanical finite element modeling of two unit cells, one consisting of a unidirectional fiber tow and the other of a plain weave lamina (Kwok and Pellegrino, 2012). A homogenization scheme was used to determine effective viscoelastic properties for a $\pm 45°$ plain weave CFRP tape spring stowed for 8 hours at both $60°C$ and $23°C$ and then deployed. The model showed good agreement with experimental results with the exception of a slightly over-predicted overshoot and deployment oscillations (Kwok and Pellegrino, 2012).

A micromechanics approach to modeling a viscoelastic plain weave composite tape spring was also performed on a specimen composed of a T300-1k carbon fiber fabric preimpregnated with Patz Materials & Technologies PMT-F4 epoxy resin (Kwok and Pellegrino, 2017). The authors developed a finite element model to simulate the viscoelastic response of a single-ply orthotropic tape spring after stowage. The fibers were assumed to be linear elastic and the epoxy matrix linear viscoelastic. The Prony series coefficients were determined through finite element -based homogenizations at the fiber/matrix scale and the tow scale. The weave geometry was characterized using optical microscopy. Tensile creep tests were performed on the neat epoxy resin to obtain its master curve. Finite element models of a single tow and complete unit cell were developed. The model results were in good agreement with the experimental results after a stowage period of eight hours at $23°C$ and at $60°C$ (Kwok and Pellegrino, 2017).

2.1.7 OPTIMIZATION MODELING OF TAPE SPRINGS

Future advances in tape spring design may be accelerated through optimization modeling. An optimization study of a two-ply $\pm 45°$ plain weave CFRP tape spring hinge was performed using a finite element model to investigate the sensitivity of folding and deployment due to geometry (length and thickness) and material (number of plies, ply arrangement, fabric type, and plain weave or tri-axial weave) with the goal of reducing the maximum mid-plane strain (Mallikarachchi and Pellegrino, 2011a). Results showed that optimal length and thickness could each reduce the maximum mid-plane strain by a factor of five (Mallikarachchi and Pellegrino, 2011a).

Finite element simulations were also used to analyze the quasi-static folding and dynamic deployment behavior of two-slot tube booms made of two-ply plain weave CFRP that wrapped around small spacecraft (Mallikarachchi and Pellegrino, 2014b). The finite element model was used to optimize the tape spring slot boom hinge design by adjusting one variable at a time and comparing the maximum value of each failure index. The results showed that shorter tape spring hinges minimized the potential for uncontrolled deployment and incomplete latching (Mallikarachchi and Pellegrino, 2014b).

An optimization study on a titanium-nickel alloy two-slot tube with tape spring hinges was performed (Hui et al., 2014). Slot length and width were examined to determine their effect on peak moment during folding and deployment using a quasi-static finite element simulation in Abaqus along with a multidisciplinary optimization software ISIGHT to apply a non-dominated sorting genetic algorithm. The results showed that the maximum Von Mises stress during folding was more responsive to slot length than slot width. During folding, the shorter the slot length or narrower the slot width, the greater the peak moment. During deployment, the longer the slot length, the lower the peak moment, while the narrower the slot width, the greater the peak moment (Hui et al., 2014).

A multi-objective optimization design of single-layer and double-layer titanium-nickel alloy tape spring hinges under folding and deployment was also performed (Yang et al., 2015). Finite element simulations were used along with non-dominated sorting genetic algorithms where the limiting points of the Pareto curve were described as two single-objective optimization problems. Both the geometric configuration and the measured and predicted moment-rotation profiles of the double-layer hinges were in good agreement, but discrepancy was seen in the slope from peak moment to steady state

moment due to the rigid clamp ends enhancing the bending stiffness of the hinge and a small angle of twist present in the test caused by installation or manufacturing errors. The final selected optimized design parameters included a separation distance between the bottom to the top of the clamp holder end of 19.844 mm, a tape spring section radius of 17.046 mm, and a central angle of 84.698° such that the maximum concentrated stress during folding was small enough to allow for repeated use, the locking moment was small enough to avoid excess shock or overshooting, and the driving moment was large enough to ensure full deployment (Yang et al., 2015).

The mechanical behavior of a deployable tape spring for solar panel reflectors was modeled to optimize the tape spring geometry (including thickness, radius of curvature, and subtended angle) to achieve minimal stress and motion amplitude (Dewalque et al., 2016). The material was beryllium copper, and the analysis was performed as linear elastic. The results showed that hysteresis was more noticeable in opposite-sense bending and larger stresses were present in equal-sense bending (Dewalque et al., 2016).

Critical design variables and domains for design optimization of deployable tape springs for controlled deployment were identified through a parametric study performed by making both uniform and gradient changes in thickness, width, stiffness, density, and ply angle to investigate their effects on deployment (Borowski et al., 2016). The results showed that uniform changes in thickness and gradient changes in width had the strongest effects on initial deployment speed (Borowski et al., 2016).

2.2 VISCOELASTICITY THEORY

2.2.1 RHEOLOGICAL MODELS

2.2.1.1 Viscoelastic Phenomena

Viscoelastic materials are those that exhibit time-dependent and temperature-dependent responses (Findley, 1976). For example, polymers are highly viscoelastic. The epoxy matrix investigated in this study consists of a polymer, which is an isotropic, linear viscoelastic material. The two fundamental types of viscoelasticity are stress relaxation and creep. *Stress relaxation* results when a material is constrained to a constant strain, and the stress required to sustain that strain lessens with time, as depicted in Figure 2.2.

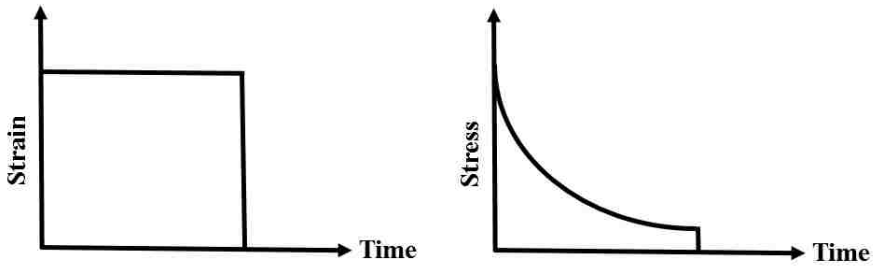

Figure 2.2. Schematic of the stress relaxation phenomenon.

For linear elastic materials, the spring behavior is defined using *Hooke's Law*. As such, linear springs are defined by (Findley, 1976):

$$\sigma = E\varepsilon \tag{2.1}$$

where E is defined as Young's modulus, σ is stress, and ε is strain. The relaxation modulus $E(t)$ is defined as (Findley, 1976):

$$E(t) = \frac{\sigma(t)}{\varepsilon_0} \tag{2.2}$$

Creep occurs when a material is subjected to a constant stress, causing an increase in strain over time, as depicted in Figure 2.3.

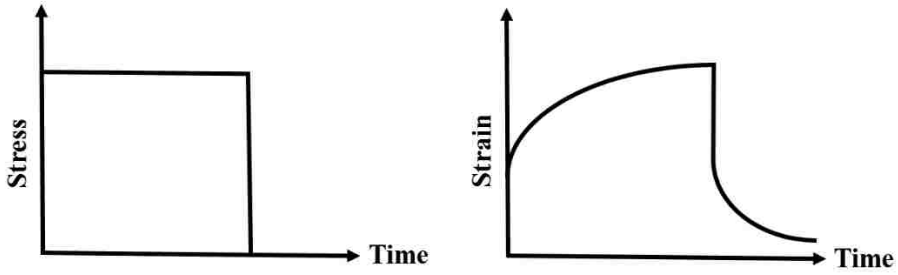

Figure 2.3. Schematic of the creep phenomenon.

The inverse of Young's modulus is represented by compliance *D*, such that:

$$\varepsilon = D\sigma \tag{2.3}$$

Creep compliance $D(t)$ is defined as (Findley, 1976):

$$D(t) = \frac{\varepsilon(t)}{\sigma_0} \tag{2.4}$$

2.2.1.2 Maxwell and Kelvin-Voigt Models

Linear viscoelastic models are described using a combination of two symbols: a spring and a dashpot. The linear *spring* is the symbol for the elastic response, and the linear *dashpot* is the symbol for the viscous response. Linear dashpot behavior is described by a viscosity parameter η and a time-dependent change in strain (Findley, 1976):

$$\sigma = \eta \frac{d\varepsilon}{dt} \tag{2.5}$$

While standard viscoelastic phenomena occurs under constant strain or stress, both phenomena also occur under variable (increasing or decreasing) stress or strain.

The two most prevalent linear viscoelastic models are Maxwell and Kelvin-Voigt. *Maxwell* is composed of a single spring and dashpot positioned in series, as depicted in Figure 2.4.

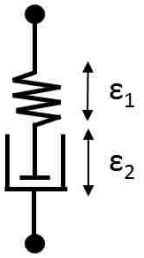

Figure 2.4. Schematic of the Maxwell model.

If a load is applied to the system, the spring and dashpot will experience a constant stress σ throughout the system, and the total strain will be the sum of the strain caused by deformations in both the spring ε_1 and the dashpot ε_2. The overall strain response with respect to time is the sum of the strain responses with respect to time of the two components (Findley, 1976). In the case of the linear spring, stress is also a function of time, because the two change together at the same rate. Therefore, a common representation of the Maxwell model is:

$$\varepsilon_T = \varepsilon_1 + \varepsilon_2 \tag{2.6}$$

$$\frac{d\varepsilon}{dt} = \frac{1}{E}\frac{d\sigma}{dt} + \frac{\sigma}{\eta} \tag{2.7}$$

The *Kelvin-Voigt* model consists of a single spring and dashpot in parallel, as shown in Figure 2.5.

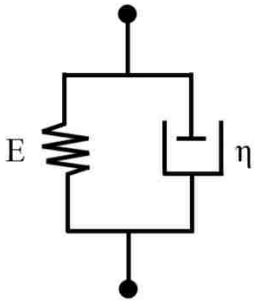

Figure 2.5. Schematic of the Kelvin-Voigt model.

When a load is applied to the spring and dashpot in parallel, the strain will be equal across both elements, and the stress response for the system will be the sum of the stress responses of each component. In the case of the viscous response, strain is a function of time, because it changes under constant stress. Therefore, a common numerical representation of the Kelvin-Voigt model is:

$$\sigma_T = \sigma_1 + \sigma_2 \tag{2.8}$$

$$\sigma = E\varepsilon + \eta\frac{\partial\varepsilon}{\partial t} \tag{2.9}$$

2.2.1.3 The Prony Series

The Prony series is a mathematical expression depicting the stress relaxation phenomenon and can be generated with data gathered from experimental relaxation or creep tests. To derive the Prony series equations, one may start with the Maxwell model (Eq. 2.7) and integrate it for a constant strain, as in the case of stress relaxation. As such, Eq. 2.7 can be rewritten as (Findley, 1976):

$$\int_{t_0}^{t}\left(\frac{d\varepsilon}{dt}\right)dt = \int_{t_0}^{t}\left(\frac{1}{E}\frac{d\sigma}{dt} + \frac{\sigma}{\eta}\right)dt \tag{2.10}$$

$$0 = \int_{t_0}^{t}\left(\frac{d\sigma}{dt} + \frac{E}{\eta}\sigma\right)dt \tag{2.11}$$

Applying linear first-order ordinary differential equations, the solution to the integration is of the form:

$$0 = \int_{t_0}^{t}\left(\dot{\sigma} + \lambda\sigma\right)dt \tag{2.12}$$

$$\sigma(t) = Ae^{-\lambda t} \tag{2.13}$$

$$\sigma(t) = Ae^{-\left(\frac{E}{\eta}\right)t} \tag{2.14}$$

Given that at time zero, the stress must be equal to σ_0, and by applying Hooke's Law shown in Eq. 2.1:

$$\sigma(0) = \sigma_0 \tag{2.15}$$

$$A = \sigma_0 \tag{2.16}$$

$$\sigma(t) = \sigma_0 e^{-\left(\frac{E}{\eta}\right)t} \tag{2.17}$$

$$\sigma(t) = E\varepsilon_0 e^{-\left(\frac{E}{\eta}\right)t} \tag{2.18}$$

If τ is used to describe the relaxation time and is equal to $\frac{\eta}{E}$, the equation becomes:

$$\sigma(t) = E\varepsilon_0 e^{-\left(\frac{t}{\tau}\right)} \tag{2.19}$$

Finally, if one were to divide through by strain and represent the exponential decay function as a step function acting on the long-term modulus E_∞, the result would be the Prony series expression of the relaxation modulus:

$$E(t) = E_\infty + \sum_{i=1}^{N} k_i e^{-\left(\frac{t}{\tau_i}\right)} \tag{2.20}$$

where k_i represents the relaxation coefficients and τ_i represents the relaxation times.

The Prony series representation for creep compliance can be derived in a similar manner, but one begins with the Kelvin-Voigt model and integrates for a constant stress, as in the case of creep. First, one begins with the Kelvin-Voigt model, divides through by Young's modulus, and writes the equation in terms of strain:

$$\sigma_0 = E\varepsilon + \eta\frac{\partial\varepsilon}{\partial t} \tag{2.21}$$

$$\varepsilon = \frac{\sigma_0}{E} - \frac{\eta}{E}\frac{\partial\varepsilon}{\partial t} \tag{2.22}$$

By applying linear first-order ordinary differential equations and integrating for a constant applied stress with respect to time, the equation becomes of the form:

$$\varepsilon(t) = Ae^{-\lambda t} + \frac{\sigma_0}{E} \tag{2.23}$$

$$\varepsilon(t) = Ae^{-\left(\frac{E}{\eta}\right)t} + \frac{\sigma_0}{E} \tag{2.24}$$

Given that at time zero, the strain must be equal to zero and by simplifying:

$$0 = A + \frac{\sigma_0}{E} \tag{2.25}$$

$$\varepsilon(t) = -\frac{\sigma_0}{E}e^{-\left(\frac{E}{\eta}\right)t} + \frac{\sigma_0}{E} \tag{2.26}$$

$$\varepsilon(t) = \frac{\sigma_0}{E}\left[1 - e^{-\left(\frac{E}{\eta}\right)t}\right] \tag{2.27}$$

If τ is used to describe the relaxation time equal to $\frac{\eta}{E}$, the equation becomes:

$$\varepsilon(t) = \frac{\sigma_0}{E}\left[1 - e^{-\left(\frac{t}{\tau}\right)}\right] \tag{2.28}$$

Finally, if one were to divide through by stress and represent the exponential growth function as a step function acting on the instantaneous compliance D, the result is the Prony series representation of the creep compliance:

$$D(t) = D_0 + \sum_{j=1}^{N} D_j\left(1 - e^{-\left(\frac{t}{\tau_j}\right)}\right) \tag{2.29}$$

2.2.2 THE BOLTZMANN SUPERPOSITION PRINCIPLE

The *Boltzmann superposition principle*, or linear superposition principle, applies to a circumstance in which a structure is exposed to arbitrary time-varying stress or strain or a history of different loadings applied in a series of incremental steps. For example, a

constant stress may be applied for some duration followed by an additional stress applied at a later time. In the case of two consecutively applied stresses, the overall strain response is a combined value resulting from both individual stresses. In other words, the material response of the structure to a given stress or strain is independent of its response to that which came before or after. Therefore, the Boltzmann superposition principle states that the overall strain can be calculated as the value of the strain caused by the first stress added to the value of the strain caused by the second stress, and so on, as though each stress was acting separately (Findley, 1976). Conversely, if the strain applied is constant for each step, the structure will experience a relaxation response resulting in a change in stress during each step. For this, the principle assumes that the relaxation responses are linearly independent and can be superimposed. From Hooke's Law and its inverse, shown in Eqs. 2.2 and 2.4, the equations described by the Boltzmann superposition principle are derived as follows. If a stress σ_0 or strain ε_0 is applied at time zero, the resultant creep or stress relaxation can be described as:

$$\sigma(t) = E(t)\varepsilon_0 \tag{2.30}$$

$$\varepsilon(t) = D(t)\sigma_0 \tag{2.31}$$

If a stress σ_1 or strain ε_1 is applied at time u, the resultant creep or stress relaxation can be described as:

$$\varepsilon(t) = D(t-u)\sigma_0 \tag{2.32}$$

$$\sigma(t) = E(t-u)\varepsilon_0 \tag{2.33}$$

If stress σ_i or strain ε_i is applied as a series of increments i of quantity N starting at time zero, creep or stress relaxation can be described as:

$$\varepsilon(t) = \sum_{i=0}^{N} D(t-u)\sigma_i \tag{2.34}$$

$$\sigma(t) = \sum_{i=0}^{N} E(t-u)\varepsilon_i \tag{2.35}$$

Finally, in limit, the equations that represent the Boltzmann superposition principle are described as:

$$\varepsilon(t) = \int_0^N D(t-u)\frac{d\sigma(u)}{du}du \tag{2.36}$$

$$\sigma(t) = \int_0^N E(t-u)\frac{d\varepsilon(u)}{du}du \tag{2.37}$$

2.2.3 TIME-TEMPERATURE SUPERPOSITION PRINCIPLE

In addition to time-dependent behavior, viscoelastic materials also exhibit temperature-dependent behaviors. Therefore, the creep compliance and relaxation modulus, while represented as functions of time, are also functions of temperature. The *time temperature superposition principle* (TTSP) is an expression of time and temperature equivalence. To be applicable the material must be *thermorheologically simple*, meaning the material's response at a high temperature over a short period of time is the same as that at a lower temperature over a longer period of time. The principle describes that for any time t and temperature T, there exists a reduced time ξ and reference temperature T_0 that can be used to describe the same creep compliance or relaxation modulus. For example, for stress relaxation, the principle can be expressed as:

$$E(T,t) = E(T_0,\xi) \tag{2.38}$$

meaning that a material's relaxation modulus at any given temperature and time is equivalent to its relaxation modulus at a reference temperature and a reduced time. This allows data collected from short-term testing to be used to predict the long-term response of viscoelastic materials. The relationship can also be expressed by a shift factor a_T, which describes the ratio of relaxation time τ at one temperature T to the relaxation time at a reference temperature T_0:

$$\alpha_T = \frac{\tau(T)}{\tau(T_0)} \tag{2.39}$$

The *Williams Landel Ferry* (WLF) equation describes an empirical relation that can be applied to solve for α_T in order to shift any relaxation or creep data to a desired reference temperature (Meyers, 2009):

$$\log(a_T) = \frac{-c_1(T - T_0)}{c_2 + (T - T_0)} \tag{2.40}$$

where c_1 and c_2 are unique material constants.

The TTSP and shift factor can be used in conjunction to produce a *master curve* to describe the relaxation behavior of a viscoelastic material. The master curve can be generated for any temperature of interest by collecting short-term relaxation test data at many temperatures ranging below and above the material's glass transition temperature. The relaxation modulus data from each temperature investigated is then shifted using a shift factor such that the data points for temperatures above the reference temperature are shifted to the right and data points for temperatures below the reference temperature are shifted to the left until a continuous curve is formed.

2.2.4 A NOTE ON POISSON'S RATIO

Poisson's ratio v exhibits a time-dependent behavior and is often defined in terms of transverse ε_t and longitudinal ε_l strains as functions of time (Kwok, 2012):

$$\nu(t) = -\frac{\varepsilon_t(t)}{\varepsilon_l(t)} \tag{2.41}$$

However, for simplicity, Poisson's ratio is often considered to be time-independent. Arguably, this assumption may only be valid for homogeneous materials at constant temperatures (Hilton, 2001). However, experimental determination of Poisson's ratio would require the measurements of multiple material properties to be taken simultaneously on the same specimen to achieve uniformity in testing conditions, such as temperature, moisture, preparation, and conditioning. Due to the difficulty that such a process presents, the assumption that Poisson's ratio is constant is often extended to orthotropic materials with the understanding that the model may not portray a completely realistic material response in this regard.

2.3 COMPOSITE THEORY

2.3.1 FLEXLAM TAPE SPRING DESIGN CONCEPT

The tape spring used in this research is known as a *FlexLam*. The theory behind the design is that it consists of an on-axis elastic lamina that supplies the deployment force and two off-axis viscoelastic laminae which lessen the deployment force with time during stowage through stress relaxation. These unique lamina responses are arrived at by utilizing the differences in behavior of the composite constituent materials. Carbon fibers are elastic materials and epoxy is a viscoelastic material, so the orientation of the composite materials will determine each lamina's dominant response. When fabricated, the tape spring is stress-

free and stable, but when folded or rolled into its stowage configuration, strain energy is gained in the system due to the external work applied to produce its deformation. In the on-axis ply, the linear elastic fibers store the strain energy during deformation, and in the off-axis plies, the viscoelastic epoxy stores the strain energy. Therefore, the on-axis lamina does not relax, but the off-axis laminae do relax, causing a dissipation of energy in the tape spring and affecting its final deployment behavior. Given its application the tape spring may remain stowed for several years throughout spacecraft assembly, component integration, and launch, only to deploy once on orbit. Once deployed, the structure will remain deployed for the remainder of its lifespan. The composite response during stowage is complex, because as the strain energy in the viscoelastic laminae dissipates, the strain in the elastic laminae redistributes.

The fiber orientation in the FlexLam layup is arranged as $[\pm 45°/0°/\pm 45°]$, as shown in Figure 2.6. The outer layers are a plain weave carbon fiber fabric preimpregnated with an epoxy resin. The fibers are oriented at $\pm 45°$ to the longitudinal axis of the tape spring and are identical in material. The middle ply is a unidirectional carbon fiber preimpregnated with an epoxy resin, and the fibers run parallel with the longitudinal axis. The layup is *symmetric*, because the ply orientations are mirrored about the structural mid-plane, and *balanced*, because the outer plies are located an equal distance from the mid-plane. The unidirectional ply is able to provide high axial stiffness and bending stiffness, limited thermal expansion, and creep resistance. However, unidirectional plies alone have low buckling strength, minor transverse bending stiffness, and low shear stiffness, and they are more prone to failure when handling and folding. The off-axis plain weave plies provide the benefit of added shear stiffness and local bending stiffness. However, the plain weave

plies experience pure shear when rolled or folded, which generates high strains in the matrix but minimal strains in the fibers. The stress-strain behavior in these plies is almost solely a function of the epoxy matrix. By contrast, during bending or folding, the middle ply behavior is fiber-dominated as the fibers are stretched and compressed. The final FlexLam composite tape spring has high axial stiffness, dimensional stability in its deployed configuration, and the ability to withstand large flexural strains.

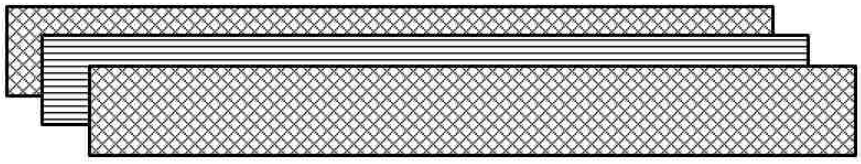

Figure 2.6: FlexLam tape spring layup.

2.3.2 COMPOSITE MICROMECHANICS

2.3.2.1 Rule of Mixtures

The *rule of mixtures* model, also known as the strength of materials model or the Voigt model, or can be applied to represent the engineering material properties of a composite lamina (Hyer, 2009). This model is based on a *1-2-3* principle coordinate system such that the *1*-direction is in the direction of the fibers, the *2*-direction is the direction perpendicular to the fibers, and the *3*-direction is the out-of-plane direction. The engineering material properties can be defined in terms of the individual fiber f and matrix m component properties weighted by their volume fractions V, such that the fiber volume fraction is the volume of fiber relative to the total volume of the composite, and the matrix volume fraction is the volume of matrix relative to the total volume of the composite, or:

$$V^m = 1 - V^f \tag{2.42}$$

For example, Young's modulus E in the direction of the fibers can be expressed as:

$$E_1 = E_1^f V^f + E^m(1 - V^f) \tag{2.43}$$

Poisson's ratio in the *1-2* plane can similarly be expressed as:

$$\nu_{12} = \nu_{12}^f V^f + \nu_{12}^m(1 - V^f) \tag{2.44}$$

The composite transverse modulus can be defined by the transverse stress and the transverse strain and can be expressed as:

$$E_2 = \frac{E_2^f}{V^f} + \frac{E^m}{(1 - V^f)} \tag{2.45}$$

The axial shear modulus of the composite can be expressed in terms of the shear modulus of the fiber and matrix components and their respective volume fractions, resulting in:

$$G_{12} = \frac{G_{12}^f}{V^f} + \frac{G^m}{(1 - V^f)} \tag{2.46}$$

For linear elastic materials, such as carbon fibers, the shear modulus can be defined by the elastic modulus and Poisson's ratio:

$$G_{12}^f = \frac{E_1^f}{2\left(1 + \nu_{12}^f\right)} \tag{2.47}$$

For a plain weave lamina with fibers oriented perpendicularly to each other, the Young's modulus in the *1*-direction and *2*-direction are taken to be equal and can be calculated as (Soykasap, 2011):

$$E_1^{PW} = E_2^{PW} = \frac{1}{2} V^f \left(E_1^f + E_2^f\right) + E^m(1 - V^f) \tag{2.48}$$

For an isotropic viscoelastic matrix material, the Prony series equation must be used to solve for the relaxation modulus of the epoxy matrix with respect to time:

$$E^m(t) = E_0^m \left[1 - \sum_{i=1}^{N} k_i \left(1 - e^{-\left(\frac{t}{\tau_i}\right)}\right)\right] \tag{2.49}$$

Assuming a constant Poisson's ratio, the shear modulus of the matrix changes with time at the same rate as the relaxation modulus, such that:

$$G^m(t) = \frac{E^m(t)}{2(1+\nu^m)} \tag{2.50}$$

Since the dimensions of the composite change according to the cumulative changes in the fibers and the epoxy matrix, Poisson's ratio of the composite is defined as:

$$\nu_{12} = \nu^m(1 - V^f) + \nu^f V^f \tag{2.51}$$

Poisson's ratio of the composite describing the change in strain in the *1*-direction caused by a stress applied in the *2*-direction can be expressed by applying a multiplicative factor to Poisson's ratio in the *1-2* plane that is the ratio of the transverse modulus to the longitudinal modulus of the lamina, shown as:

$$\nu_{21} = \frac{E_2}{E_1}\nu_{12} \tag{2.52}$$

2.3.2.2 Models for Composite Shear Modulus

One common criticism of the rule of mixtures is that greatly underestimates the shear modulus G_{12} of the lamina. Younes et al. (2012) presented a comparison of phenomenological models, semi-empirical models, elasticity approach models, and homogenization models for calculating composite material properties, including G_{12}, and compared them to the rule of mixtures. The Chamis micromechanical model showed promising results and was reported as the most used and trusted model for calculating the material properties of interest in the paper. For this reason, the Chamis model was applied to find G_{12} of the lamina:

$$G_{12} = \frac{G^m}{1 - \sqrt{V^f}\left(1 - \frac{G^m}{G^f}\right)} \tag{2.53}$$

2.3.2.3 The Stiffness Matrix

The stiffness of a two-dimensional composite lamina can be represented using the *stiffness matrix*, defined as (Hyer, 2009):

$$\begin{Bmatrix} \sigma_1 \\ \sigma_2 \\ \sigma_3 \\ \tau_{23} \\ \tau_{13} \\ \tau_{12} \end{Bmatrix} = \begin{bmatrix} C_{11} & C_{12} & C_{13} & 0 & 0 & 0 \\ C_{21} & C_{22} & C_{23} & 0 & 0 & 0 \\ C_{31} & C_{32} & C_{33} & 0 & 0 & 0 \\ 0 & 0 & 0 & C_{44} & 0 & 0 \\ 0 & 0 & 0 & 0 & C_{55} & 0 \\ 0 & 0 & 0 & 0 & 0 & C_{66} \end{bmatrix} \begin{Bmatrix} \varepsilon_1 \\ \varepsilon_2 \\ \varepsilon_3 \\ \gamma_{23} \\ \gamma_{13} \\ \gamma_{12} \end{Bmatrix} \tag{2.54}$$

For the analysis of a composite plate with a *plane stress* assumption, meaning that one dimension is at least an order of magnitude smaller than the other two dimensions, as in the case of the tape spring, the stress components perpendicular to the plane (*i.e.* σ_3, τ_{23}, and τ_{13}) can be assumed to be zero. This results in a 3 x 3 matrix called the *reduced stiffness matrix*:

$$\begin{Bmatrix} \sigma_1 \\ \sigma_2 \\ \tau_{12} \end{Bmatrix} = \begin{bmatrix} Q_{11} & Q_{12} & 0 \\ Q_{12} & Q_{22} & 0 \\ 0 & 0 & Q_{66} \end{bmatrix} \begin{Bmatrix} \varepsilon_1 \\ \varepsilon_2 \\ \gamma_{12} \end{Bmatrix} \tag{2.55}$$

or:

$$\begin{Bmatrix} \sigma_1 \\ \sigma_2 \\ \tau_{12} \end{Bmatrix} = \begin{bmatrix} \frac{E_1}{1 - \nu_{12}\nu_{21}} & \frac{E_2\nu_{12}}{1 - \nu_{12}\nu_{21}} & 0 \\ \frac{E_2\nu_{12}}{1 - \nu_{12}\nu_{21}} & \frac{E_2}{1 - \nu_{12}\nu_{21}} & 0 \\ 0 & 0 & G_{12} \end{bmatrix} \begin{Bmatrix} \varepsilon_1 \\ \varepsilon_2 \\ \gamma_{12} \end{Bmatrix} \tag{2.56}$$

The *transformation matrix* is used to transform global stresses or strains to local stresses or strains, and the inverse of the transformation is used to transform local values into global values. The *inverse transformation matrix* is defined as:

$$[T]^{-1} = \begin{bmatrix} m^2 & n^2 & -2mn \\ n^2 & m^2 & 2mn \\ mn & -mn & m^2 - n^2 \end{bmatrix} \tag{2.57}$$

where $m = cos(\theta)$ and $n = sin(\theta)$. Therefore, to transform local stresses and strains to global values, the following can be applied:

$$\begin{Bmatrix} \sigma_x \\ \sigma_y \\ \tau_{xy} \end{Bmatrix} = \begin{bmatrix} m^2 & n^2 & -2mn \\ n^2 & m^2 & 2mn \\ mn & -mn & m^2 - n^2 \end{bmatrix} \begin{Bmatrix} \sigma_1 \\ \sigma_2 \\ \tau_{12} \end{Bmatrix} \tag{2.58}$$

$$\begin{Bmatrix} \varepsilon_x \\ \varepsilon_y \\ \frac{1}{2}\gamma_{xy} \end{Bmatrix} = \begin{bmatrix} m^2 & n^2 & -2mn \\ n^2 & m^2 & 2mn \\ mn & -mn & m^2 - n^2 \end{bmatrix} \begin{Bmatrix} \varepsilon_1 \\ \varepsilon_2 \\ \frac{1}{2}\gamma_{12} \end{Bmatrix} \tag{2.59}$$

CHAPTER 3 METHODS

3.1 EXPERIMENTAL METHODS

3.1.1 FLEXLAM SLIT TUBE FABRICATION

3.1.1.1 Composite Slit Tube Layup Procedure

A full-size FlexLam slit tube of roughly six meters in length was fabricated in the Integrated Structural Systems' Composites Laboratory within the Air Force Research Laboratory (AFRL) Space Vehicles Directorate located at Kirtland Air Force Base, NM. The laminate was composed of three plies consisting of unidirectional (UD) and plain weave (PW) carbon fiber preimpregnated ("prepreg") composite materials, shown in Figure 3.1, arranged in a layup of $[\pm 45°PW/0°UD/\pm 45°PW]$. The unidirectional lamina consisted of an IM7 carbon fiber prepreg with Patz Materials & Technologies PMT-F7 toughened epoxy resin (Patz, 2014). The plain weave fabric was a 6k tow IM7 GP carbon fiber fabric prepreg with Patz Materials & Technologies GP2-61-2 resin. Although the GP2-61-2 resin has since been discontinued, the PMT-F7 was reported by Patz Materials & Technologies to be a comparable epoxy resin.

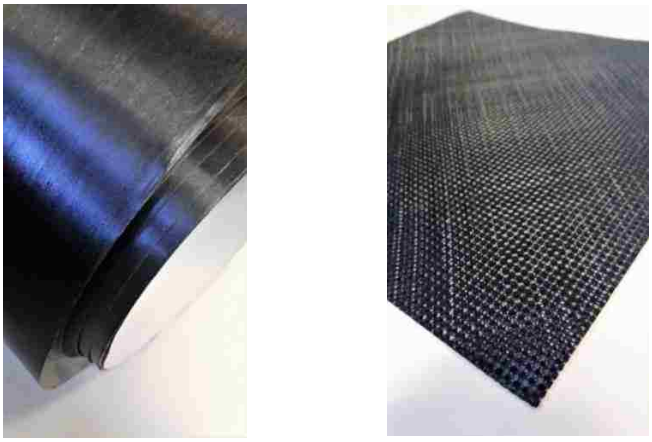

(a) (b)

Figure 3.1: (a) Unidirectional carbon fiber prepreg, and (b) plain weave carbon fiber fabric prepreg.

First, the prepreg composite materials were removed from a freezer and thawed inside their packaging. Each type of material was then cut into a sheet of required dimensions including splicing features required in the biased plain weave plies to meet overall length specifications. A hollow cylindrical steel mandrel with a 101.6 mm outer diameter was treated with a mold release agent and preheated in a large autoclave to $49°C$. The carbon fiber prepreg plies were layered atop a precision-leveled rolling table following the sequence and orientations specified in the layup schedule. The laminate stack was then aligned and rolled onto the heated mandrel, immediately followed by a layer of non-perforated release ply. The entire setup was then layered with breather fabric, placed inside a vacuum bag, and transported to an autoclave for curing. The curing cycle consisted of a one hour soak at $107°C$ under 0.138 MPa of pressure followed by three hours at $177°C$ under 0.552 MPa of pressure. After the composite laminate had returned to room temperature, it was separated from the mandrel and machine-trimmed to its final dimensions. The resultant 101.6 mm diameter CFRP slit tubes are shown below in Figure 3.2.

(a) (b)

Figure 3.2: CFRP slit tube tape springs with a 101.6 mm diameter in the Integrated Structural Systems' Composites Laboratory at AFRL shown in their (a) deployed configuration and (b) stowed configuration. Images courtesy of Michael Peterson.

The full-length slit tube was then cut both longitudinally and transversely to produce smaller tape springs for testing purposes with dimensions specified in Table 1, where L is the length, w is the width, R is the cross-sectional radius, α is the subtending angle, and t is the thickness. The test specimens, prepared by waterjet cutting, are shown in Figure 3.3.

Table 1. Dimensions of tape spring test specimens.

L	304.8 mm
w	25.06 mm
R	50.8 mm
α	29°
t	0.48 mm

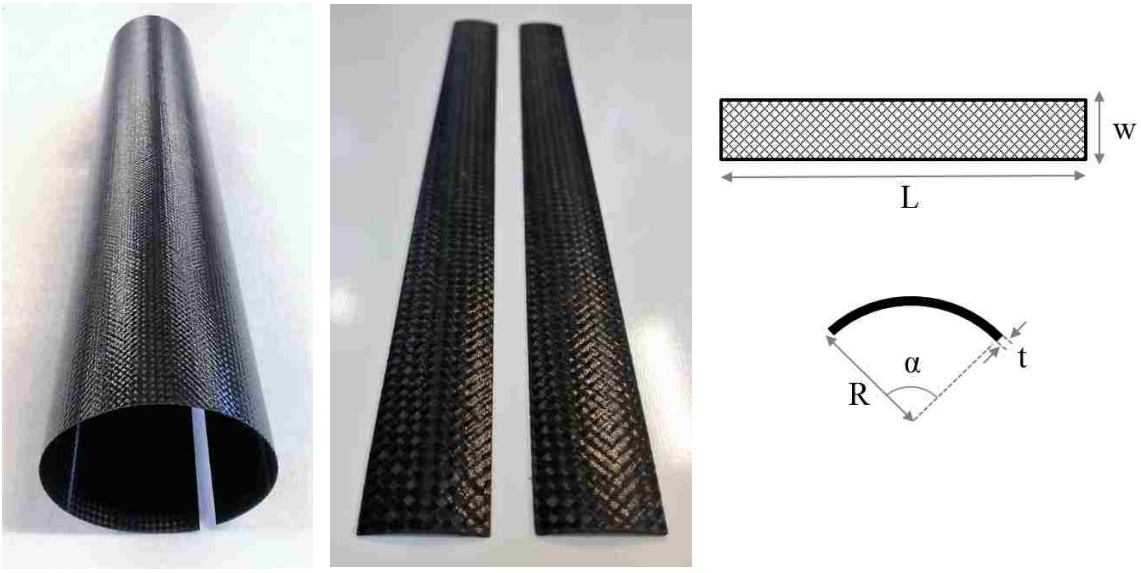

(a) (b) (c)

Figure 3.3: (a) Section of CFRP slit tube, (b) tape spring test specimens cut from slit tube, and (c) tape spring test specimen schematics.

3.1.2 MATERIAL CHARACTERIZATION TESTING

3.1.2.1 Plain Weave Coupon Tension Tests

A two-ply plain weave CFRP laminate plate was fabricated using Patz Materials & Technologies IM7 GP-6k carbon fiber fabric prepreg with GP2-61-2 resin. A Stahl's Hotronix heat press was used to cure the plate, shown in Figure 3.4(a), by pressing it for one hour at $107°C$ under 0.138 MPa of pressure followed by three hours at $177°C$ under 0.552 MPa of pressure. After allowing the plate to return to room temperature, the plate was cut into coupons with dimensions shown in Figure 3.4(b). Coupon tension testing was performed in accordance with ASTM 3518/D3518M-94.

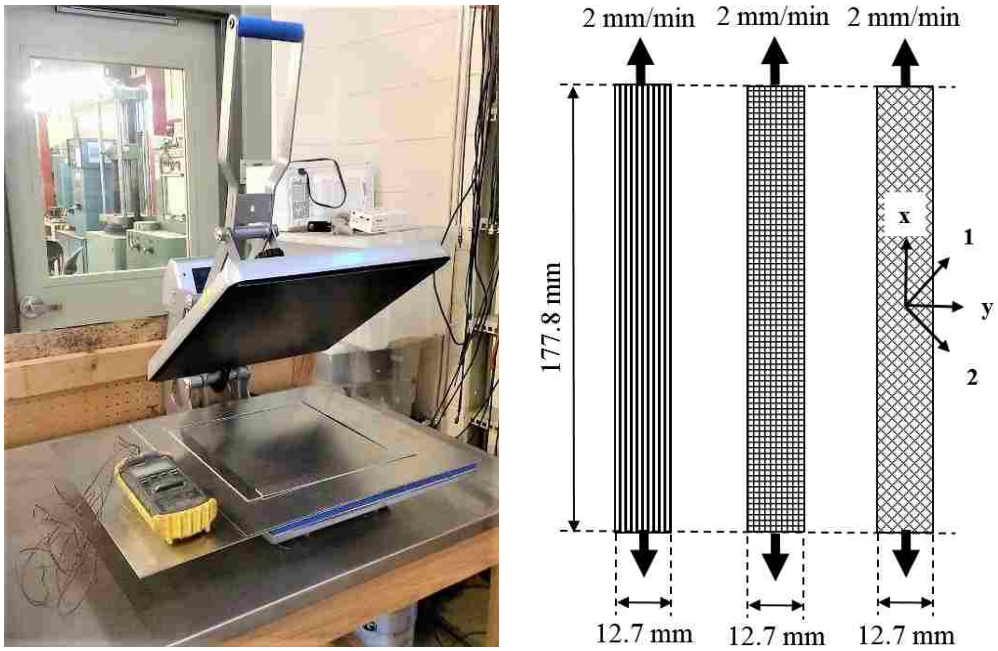

(a) (b)

Figure 3.4: (a) Heat press setup for fabricating flat coupons, and (b) schematics of tensions tests for unidirectional on-axis, plain weave on-axis, and plain weave off-axis coupons.

The coupon dimensions were 12.7 mm by 177.8 mm with fibers oriented at either $0°$ or $\pm 45°$ to the loading direction. Gripping tabs were glued to the ends of the coupons to prevent slippage, and the coupons were tested in tension using an MTS Bionix servo-hydraulic machine, shown in Figure 3.5(a). Two Digi-Key CEA linear strain gages were fastened to the middle of each specimen to measure the strain in the loading and transverse directions, as shown in Figure 3.5(b). Strain was measured within a range of $\pm 5\%$ with a resistance of 350 Ohms and a resistance tolerance of $\pm 0.3\%$. Displacement control was applied with a crosshead rate set to 2 mm/minute.

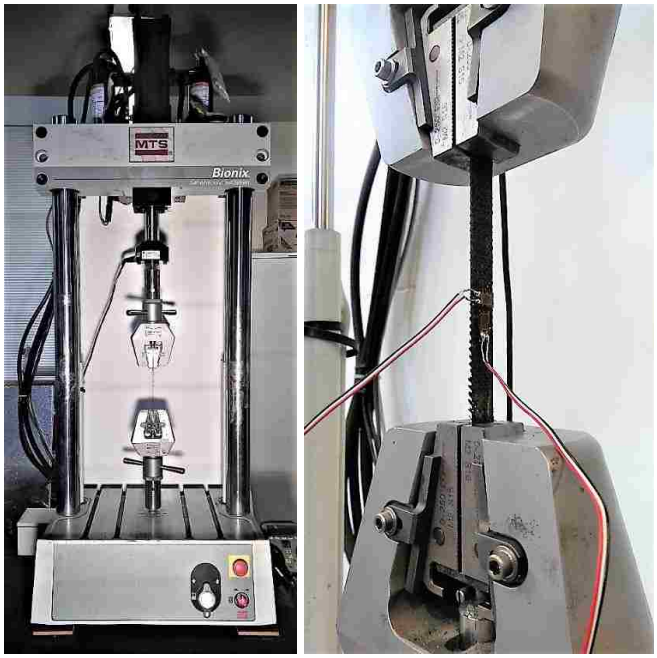

(a) (b)

Figure 3.5: (a) MTS Bionix testing machine, and (b) a close-up of a plain weave coupon tested in tension.

The variables recorded during testing were load P, axial displacement δ, longitudinal normal strain ε_x, and lateral normal strain ε_y. Shear stress τ_{12} was calculated as:

$$\tau_{12} = \frac{P}{2A} \tag{3.1}$$

where A is defined as the cross-sectional area of the coupon. Shear strain γ_{12} was calculated as:

$$\gamma_{12} = \varepsilon_x - \varepsilon_y \tag{3.2}$$

The in-plane shear modulus of elasticity G^{chord} was calculated using the following equation:

$$G_{12}^{chord} = \frac{\Delta\tau_{12}}{\Delta\gamma_{12}} \tag{3.3}$$

where $\Delta\gamma_{12}$ is the difference between two shear strain data points in the linear portion of the shear strain plot, and $\Delta\tau_{12}$ is the difference in applied stress between the two data points in the linear portion of the plot. Ultimate in-plane shear strength S_{12} was calculated using:

$$S_{12} = \frac{P_{max}}{2A} \tag{3.4}$$

where P_{max} is the maximum load before specimen failure. Additionally, ultimate tensile strength $+S_{11}$ was calculated by dividing the peak load by the cross-sectional area of the coupon. Young's modulus in the fill tow direction E_{11} and Young's modulus in the warp tow direction E_{22} were taken to be equal and calculated as the initial linear slope of the stress versus axial strain plot. The in-plane Poisson's ratio ν_{12} was determined by the difference between two points of the transverse strain data along the initial linear portion of the transverse strain versus axial strain plot divided by the difference between the two data points of axial strain.

3.1.2.2 Unidirectional Coupon Tension Tests

The coupons used for the unidirectional material testing were fabricated following the same procedure as for the plain weave CFRP coupons except for the material used. The

unidirectional material was an IM7 carbon fiber preimpregnated with an 8552 epoxy resin. The coupons were tabbed and cut with the same dimensions as the plain weave coupons with the fibers oriented parallel to the loading direction. Testing was performed in accordance with ASTM D3039/D3039M–14. The ultimate tensile strength $+S_{11}$, Young's modulus in the fill tow direction E_{11}, and the in-plane Poisson's ratio ν_{12} were determined following the same procedure as described for the plain weave material testing.

3.1.2.3 Fiber Volume Fraction Tests

Determination of the fiber volume fraction of the three-layer FlexLam CFRP laminate was performed in accordance with ASTM D3171–15 using nitric acid to dissolve the epoxy matrix. Specimens of the tape spring laminate were cut to dimensions of approximately 25 mm by 25 mm, as shown in Figure 3.6(a), which weighed on average 0.4776 grams. Each specimen was placed into a glass beaker with approximately 100 mL of 69.5% nitric acid from KMG Electronic Chemicals, Inc. and heated to $80°C$ for 6 hours. The mixture was then filtered and vacuumed, rinsed three times with distilled water, and cleaned with acetone. The remaining fibers were placed on a ceramic plate, covered with perforated aluminum foil, and heated at $100°C$ for 1 hour. The cooled fibers from each specimen, shown in Figure 3.6(b), were then weighed.

(a) (b)

Figure 3.6: (a) Tape spring laminate specimen before testing, and (b) carbon fibers of specimen after epoxy disintegration.

The fiber volume fraction was calculated as:

$$V_r = \frac{M_f}{M_i} \times 100 \times \frac{\rho_c}{\rho_r} \tag{3.5}$$

where V_r is the fiber volume fraction, M_f is the final mass of the fibers, M_i is the initial mass of the laminate specimen, ρ_c is the density of the composite, and ρ_r is the density of the IM7 carbon fibers, reported by Hexcel to be 1.78 g/cm^3 (Hexcel, 2014).

3.1.2.4 Epoxy Master Curves

To numerically describe the stress relaxation behavior of the CFRP tape spring, a master curve of the epoxy used in the matrix of the plain weave laminae was developed. This was done through a series of stress relaxation tests performed with a dynamic mechanical analysis (DMA) machine, shown in Figure 3.7, in the Polymers and Composites Laboratory at the University of New Mexico (UNM). The PMT-F7 resin specimens were first molded and cured by Patz Materials & Technologies at $177°C$ for two hours (Patz, 2014). The cured epoxy was then transported to the UNM Physics Laboratory where it was cut and shaved down to rectangular specimens with dimensions of 20 mm by 5 mm by 1 mm. The epoxy specimens were then tested for stress relaxation in tension using the DMA, TA Instruments Q800 (Garner et al., 2015). Throughout testing the temperature was increased from $30°C$ to $240°C$ by increments of $5°C$. After the machine equilibrated at each temperature for 5 minutes, the specimen was displaced 0.1 µm over 10 minutes before the temperature was increased to the next value and the specimen displacement was reset to zero. The modulus of the epoxy was measured as a function of time for each temperature investigated. Using the time-temperature superposition principle (TTSP) (Findley, 1976), the modulus versus time data for each temperature of testing was shifted to generate the master curve of the epoxy with a reference temperature of $30°C$.

(a) (b)

Figure 3.7: (a) DMA machine, and (b) an epoxy specimen tested for stress relaxation in tension. Images courtesy of Amy Garner.

3.1.3 TAPE SPRING STOWAGE AND DEPLOYMENT FIXTURE

The tape spring stowage and deployment (TSSD) aluminum fixture, shown schematically in Figure 3.8, was specially designed to provide a repeatable means by which to investigate the high strain stowage and dynamic deployment behavior of composite tape springs with precise regulation and the collection of the variables of interest. Therefore, the TSSD fixture was designed to fulfill a detailed set of requirements. It needed to be able to: 1) securely constrain the specimen in a high shear strain configuration for an extended period of time, 2) maintain a fixed strain in the specimen throughout stowage, 3) prevent any damage induction upon the specimen, 4) record and store load, strain, and temperature data over long periods of testing, 5) register minute changes in restoring force throughout stowage, 6) minimize vibrations, 7) remain undisturbed for up to months at a time, 8) allow for a sudden and unobtrusive release of boundary constraints, 9) enable rapid deployment,

and 10) allow for visual footage of the high-speed deployment procedure to be captured for microsecond tracking.

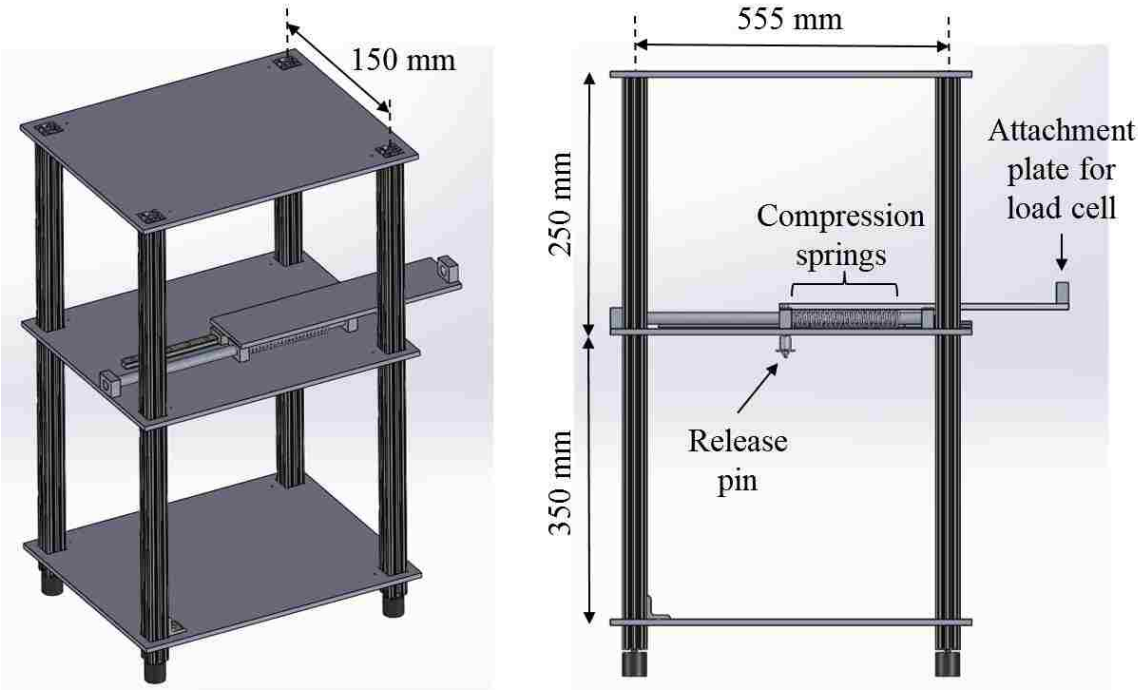

Figure 3.8: TSSD fixture schematics courtesy of James Love.

In addition to the TSSD fixture, the final TSSD setup, shown schematically in Figure 3.9, includes an aluminum cylinder which provides a fixed boundary condition for the tape spring, a radial chart for tracking displacement during deployment, and a desktop computer for collecting data over the entire period of testing. In the center of the setup, the tape spring is clamped to the aluminum pole at the start of the test. To achieve the stowage configuration, the tape spring is folded over and secured to the load cell plate with a tiny screw passing through the tape spring to prevent any slippage during the long-term stowage period. The load cell is connected to a horizontally sliding plate housing two compression springs. During stowage, the springs are compressed and locked into place with a release

pin. Throughout stowage, restoring force is collected via the load cell, temperature data is collected, and in some cases, strain data is collected via strain gages.

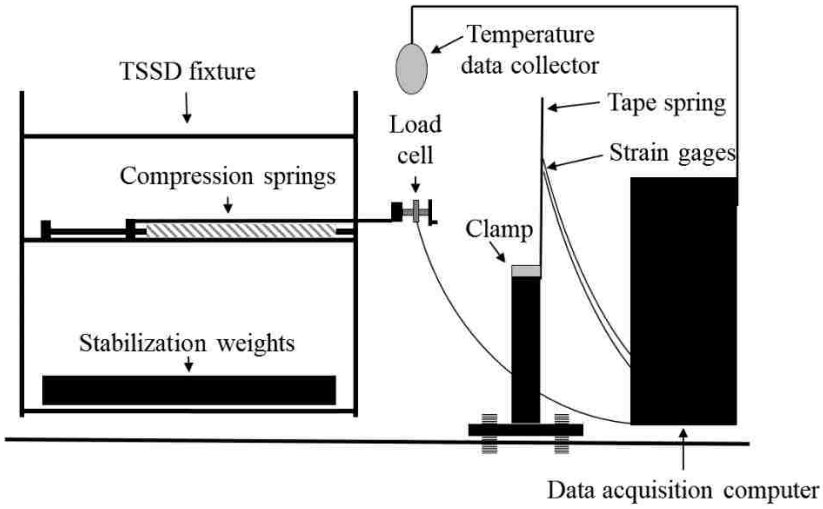

Figure 3.9: Final TSSD setup.

Before testing, an Omega subminiature tension and compression load cell with a diameter of 19.05 mm and a 111 N capacity was calibrated and screwed into the TSSD fixture, shown in Figure 3.10(a). An Omega USB in-line field calibratable signal conditioner was used to attach the load cell to a desktop computer to record and store load readings over time. The tape spring was fixed at one end to a 50.8 mm diameter aluminum cylinder with a stainless steel hose clamp, shown in Figure 3.10(b).

(a) (b)

Figure 3.10: (a) Compression load cell screwed into TSSD fixture, and (b) close-up of the clamped end of the tape spring.

A 4.40 mm diameter hole was drilled into the deployable end of the tape spring 57.47 mm from its free edge in order to secure it in place throughout the extended stowage period. This was done by running a M4-.70 screw through the hole and into the 29.6 mm long by 34.0 mm wide aluminum plate, shown in Figure 3.11. The load cell was screwed into the aluminum plate from the opposite side. The contact between the load cell and the plate was limited to a ledge that was 2.62 mm tall and 1.99 mm wide to improve contact accuracy for simulation purposes. The load cell was attached to a cable assembly and an IN-USBH which connected to a desktop computer to collect load data during stowage using Omega software Digital Transducer Application 2.2.1. The force with which the tape spring pushed against the load cell ("restoring force") was recorded over the entire stowage period. Load readings were taken once every minute.

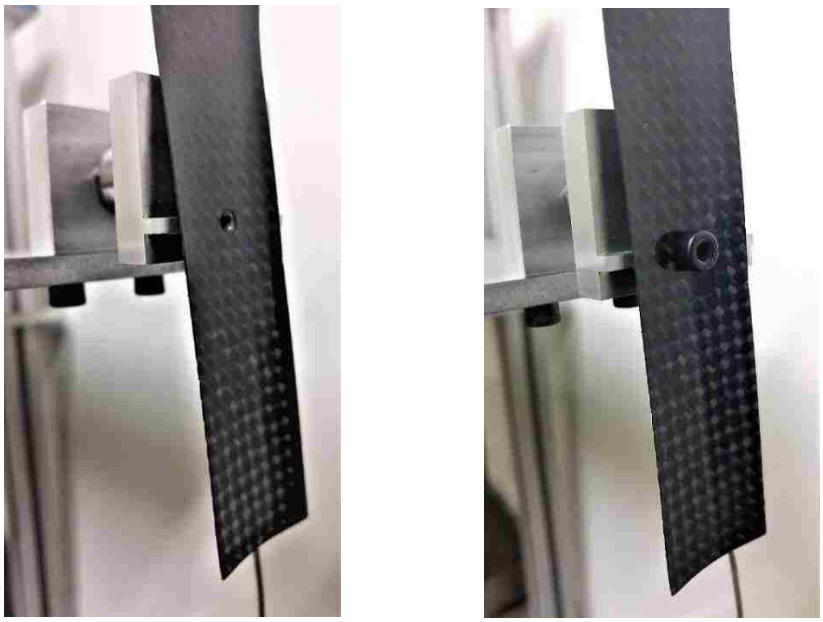

(a) (b)

Figure 3.11: Hole in free end of tape spring used to secure tape spring in stowage configuration over long-term stowage (a) without screw and (b) with screw in place.

Starting in a vertical position, shown in Figure 2.12(a), to initiate stowage, the deployable end of the tape spring was gently folded by hand so that it was parallel to its own fixed end. Then the deployable end was fixed in this configuration to the load cell plate with a screw. The moveable load cell boundary condition contained a spring-loaded release mechanism to enable it to quickly clear the path for the tape spring deployment. During stowage, the moveable boundary condition was fixed in place with springs compressed using a quick release pin, shown in Figure 3.12(b).

(a) (b)

Figure 3.12: (a) Clamped tape spring in deployed configuration, and (b) compressed springs in TSSD fixture locked in place.

Temperature data was collected throughout the stowage experiments using a Supco miniature data logger for temperature collection. Temperature readings were taken once every 10 minutes using the provided Supco Logger Interface software and a laptop. The temperature reader was suspended in the air approximately 1 meter from the stowed tape spring. The entire setup was contained in a room that was inaccessible except for data collection twice daily to limit any disturbance to the system.

3.1.4 STOWAGE TESTING

3.1.4.1 Phase One Stowage

During Phase One testing, the tape spring specimen was stowed in the TSSD fixture for 28 days at room temperature. Along the mid-span of the tape spring, two strain gages were attached using Loctite superglue ultragel control, as shown in Figure 3.13. One measured strain in the axial direction and the other in the transverse direction. The strain gages were Full Wheatstone Bridge strain gages from Omega. The first wire on the "1" end of the strain gage was attached to the red/brown wires of the cable assembly, the second wire of the strain gage to the green wire of the cable assembly, the third to the black/blue wires, and the last two to the white wire. These attachments were made using solder on an accessory terminal pad, which was also attached to the tape spring with superglue. The cable assembly was then attached to an IN-USBH which connected to a desktop computer to collect strain data over time using the Omega software Digital Transducer Application 2.2.1. Strain readings were taken once every minute.

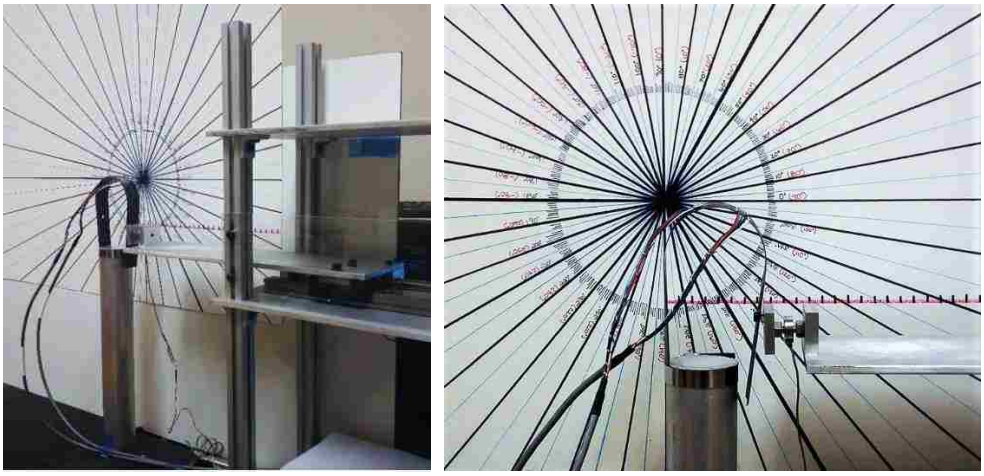

Figure 3.13: Phase One tape spring specimen in stowage configuration.

3.1.4.2 Phase Three Stowage

Once Phase One testing confirmed the presence of a constant strain throughout tape spring stowage, Phase Three testing was performed to eliminate the possible effect of strain gages on deployment. The Phase Three testing stowage setup, shown in Figure 3.14, and procedure were identical to the Phase One testing stowage setup with the exception of strain gages. During Phase Three testing, the tape spring specimen was stowed in the TSSD fixture for 34 days at room temperature without the use of strain gages.

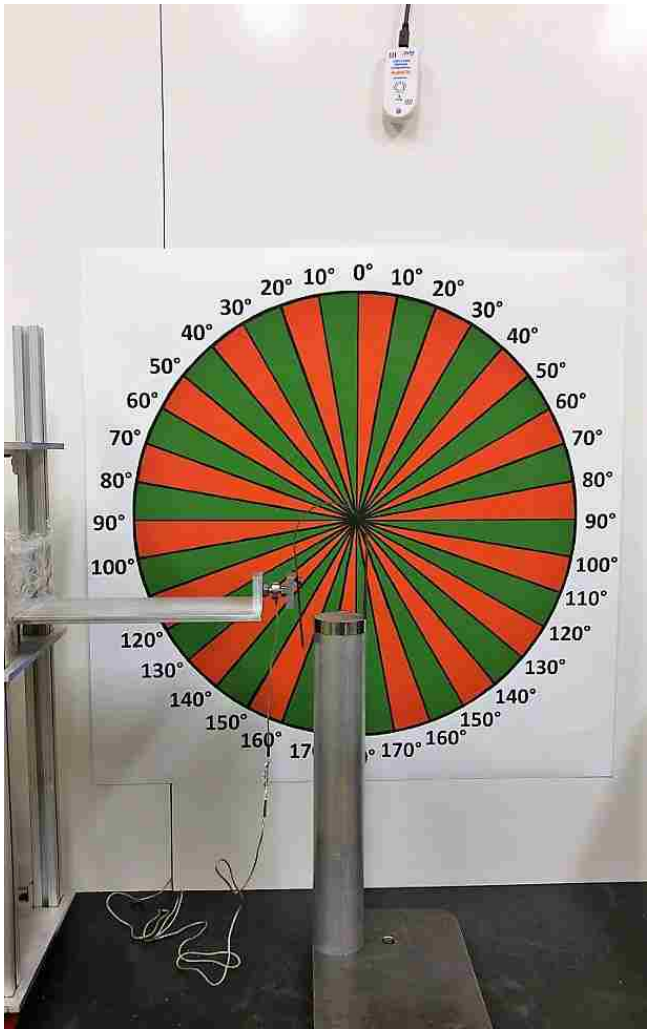

Figure 3.14: Phase Three tape spring specimen in stowage configuration.

3.1.5 DEPLOYMENT TESTING

3.1.5.1 Phase One Deployment

After the desired stowage time had been completed, deployment was initiated. First, a high speed digital camera was set up, as shown in Figure 3.15. The camera used was a Phantom Miro 110/111 with a resolution of 1280 x 800, a frame rate of 1600 frames per second, and an exposure of 300 μs. The lens used was a Canon UltraSonic EF 24 mm f/1.4L 11 USM. The camera was placed in front of the tape spring with a radial measurement screen in the background to correspond the deployment time to the angle of fold in the tape spring throughout the deployment process.

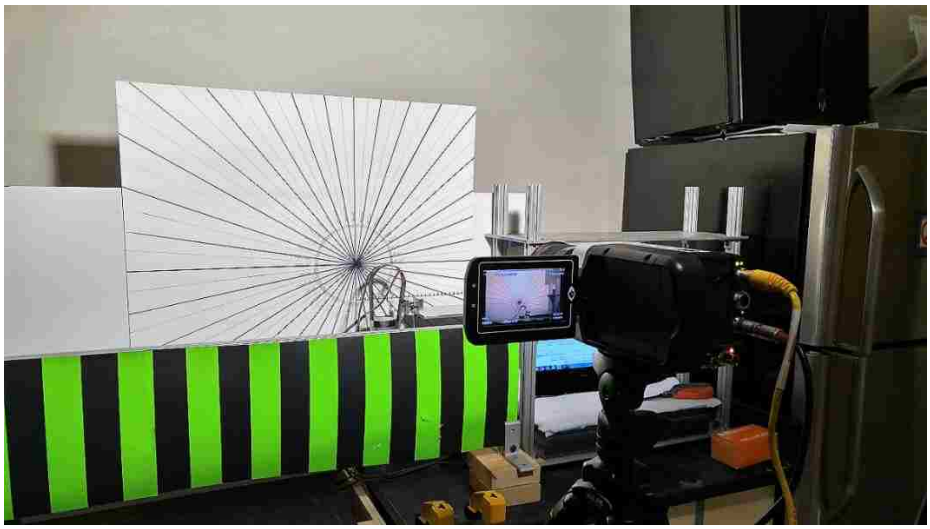

Figure 3.15: High-speed digital camera recording Phase One deployment.

Next, the small screw securing the specimen was carefully removed from the load cell plate, shown in Figure 3.16. The quick release pin trigger was then pulled to release the two highly-compressed springs within the fixture. The springs rapidly pushed the load cell plate away from the tape spring specimen horizontally to clear a path for its deployment. The entire deployment process was recorded using the high-speed digital camcorder.

(a) (b)

Figure 3.16: Deployable end of tape spring specimen (a) held in place against the load cell plate with a screw and (b) balanced in place with the screw removed.

Due to undergoing stress relaxation, a tape spring does not always return to its original deployed configuration immediately following initial deployment. This slow return to a straight configuration is known as *long-term viscoelastic recovery*, and it can take anywhere from several hours to several days. To capture the long-term viscoelastic recovery over several days following deployment, a Celestron handheld digital microscope camera, shown in Figure 3.17, was set up in front of the tape spring and left undisturbed to record one snapshot per hour of the deployed position of the tape spring.

Figure 3.17: Recording of long-term viscoelastic recovery following Phase One deployment testing.

3.1.5.2 Phase Two Deployment

The second phase of deployment testing was performed in the same manner as the Phase One deployment test with the exception of attaching strain gages or exposure to a stowage period. To conduct Phase Two deployment testing, a previously untested tape spring specimen was fastened into the TSSD fixture with the clamp, the deployable end was folded into place against the load cell plate, and then the spring-loaded release mechanism was activated to immediately initiate deployment without a stowage period. The tape spring deployment was filmed using a high-speed digital camera as in Phase One deployment testing. No long-term recovery was observed. Phase Two deployment testing was completed as a base case to compare the effect of viscoelasticity observed over a 28-day stowage period on deployment to tape spring deployment unaffected by viscoelasticity or stowage.

3.1.5.3 Phase Three Deployment

The same deployment procedure as that used in Phase One and Phase Two deployment testing was applied to Phase Three deployment testing without the attachment of strain gages and exposed to a 34-day stowage period. The high-speed digital camera setup is shown in Figure 3.18. The long-term recovery setup using the handheld digital microscope camera is shown in Figure 3.19.

Figure 3.18: High-speed digital camera recording Phase Three deployment testing.

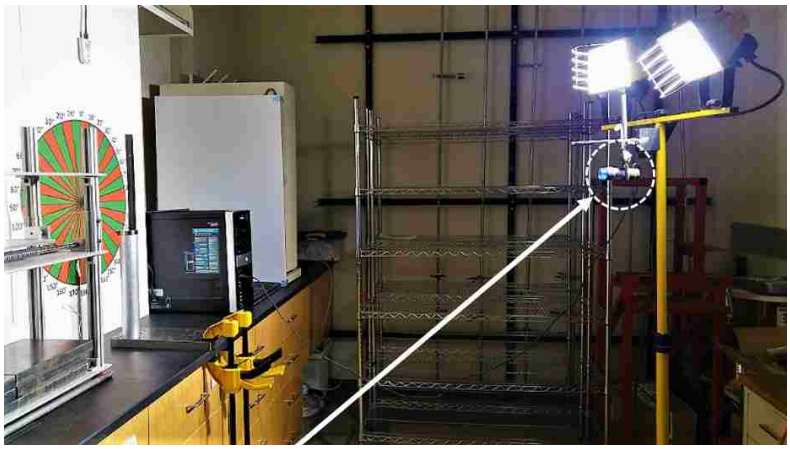

Figure 3.19: Recording of long-term viscoelastic recovery following Phase Three deployment testing.

3.2 NUMERICAL METHODS

3.2.1 SIMULATION INPUT VALUES

A finite element model was created using Abaqus/CAE (Simulia, 2014) to simulate the folding, stowage, and deployment behavior of the viscoelastic three-ply FlexLam composite tape spring.

3.2.1.1 Autodesk Simulation Composite Design

The material properties that could not be reasonably obtained through the experimental means discussed in Section 3.1.2 or through datasheets made available by the material manufactures were approximated with the assistance of Autodesk Simulation Composite Design, formerly known as Helius:MCT (Autodesk, 2014). The software provides a material library from which one can select a similar fiber and epoxy matrix to replicate the lamina tested experimentally. The final material properties for the plain weave and unidirectional laminae were determined through a combination of experimental testing,

model calibration, and reference to material datasheets and the Autodesk Simulation Composite Design material library, as shown in Table 2.

Table 2: Final material properties used in the finite element model.

Plain Weave		*Source*
Damping α	0.05	Default
Damping β	0	Default
Density (tonne/mm^3)	1.50 E-09	Testing
E_{1f} *(MPa)*	276,000	Hexcel IM7
E_{2f} *(MPa)*	19,000	Autodesk: IM7
E_{m0} *(MPa)*	2,101	Testing
v_m	0.34	Autodesk: 3501-6
v_f	0.2	Autodesk: IM7
V_f	0.53	Testing

Unidirectional		*Source*
Damping α	0.05	Default
Damping β	0.0029	Model calibration
Density (tonne/mm^3)	1.50 E-09	Testing
E_1 *(MPa)*	122,204	Testing
E_2 *(MPa)*	12,220	Typical ratio
v_{12}	0.27	Testing
G_{12} *(MPa)*	4,753	Autodesk: IM7-8552
G_{13} *(MPa)*	4,753	Autodesk: IM7-8552
G_{23} *(MPa)*	3,898	Autodesk: IM7-8552

3.2.1.2 Determination of Prony Series

To simulate the stress relaxation of the plain weave laminae, the Prony series coefficients needed to be determined. The Prony series equation (Eq. 2.20) was fit to the master curve developed for the PMT-F7 epoxy resin using a MatLab curve fitting tool that uses least squares optimization. The MatLab fit options allow for the upper and lower bounds per variable of interest to be defined. The quantity of terms in the Prony series equation should

reflect the number of decades of time represented by the master curve. In this case, fourteen relaxation coefficients and relaxation times were determined through the curve fitting procedure.

3.2.1.3 Additional Simulation Parameters

In the finite element model, the tape spring part was generated using a 3D deformable swept shell with a curved cross-section passing through the points (-12.53, 0), (12.53, 0), and (0, 1.57), as shown in Figure 3.20. The *path* sketch consisted of a line drawn between points (0, 0) and (304.8, 0) to extend the cross-section for the length of the tape spring.

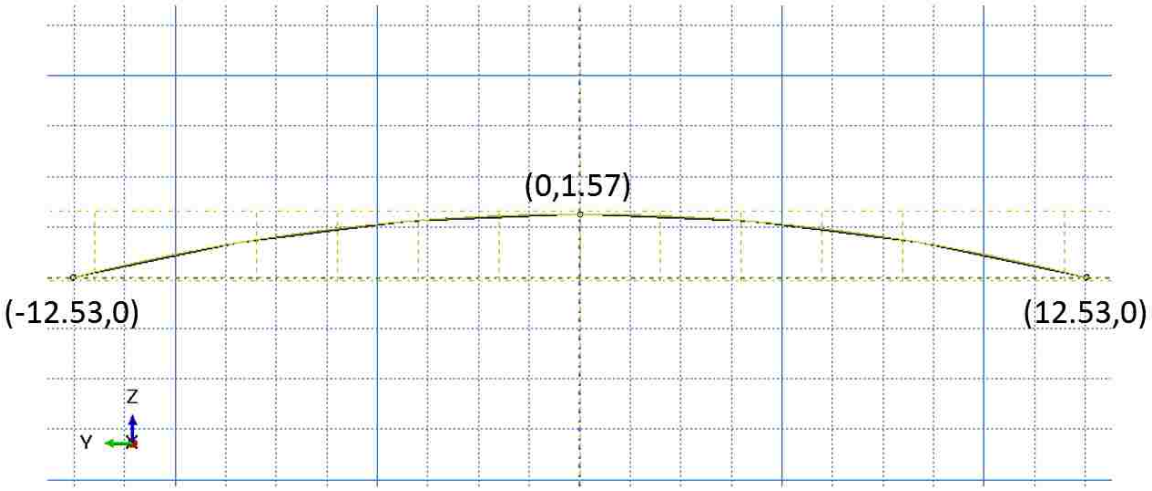

Figure 3.20: Sketch of the tape spring shell cross-section in Abaqus.

The topmost 12.9 mm of the aluminum cylinder, shown in Figure 3.21, was modeled to represent the contact surface between the tape spring and the cylinder which experimentally was applied by the steel hose clamp. The cylinder had a diameter of 50.8 mm, and its mesh consisted of 300 linear hexahedral elements with an approximate size of 5 mm. It was assigned typical aluminum material properties, including a mass density of 4×10^{-6} tonne/mm^3, an elastic modulus of 10,000 N/mm^2, and a Poisson's ratio of 0.33. The mesh of the tape spring consisted of 2,086 linear quadrilateral elements with an

approximate size of 2 mm. The element type used was a four-node doubly curved thin or thick shell element with reduced integration, hourglass control, and finite membrane strains.

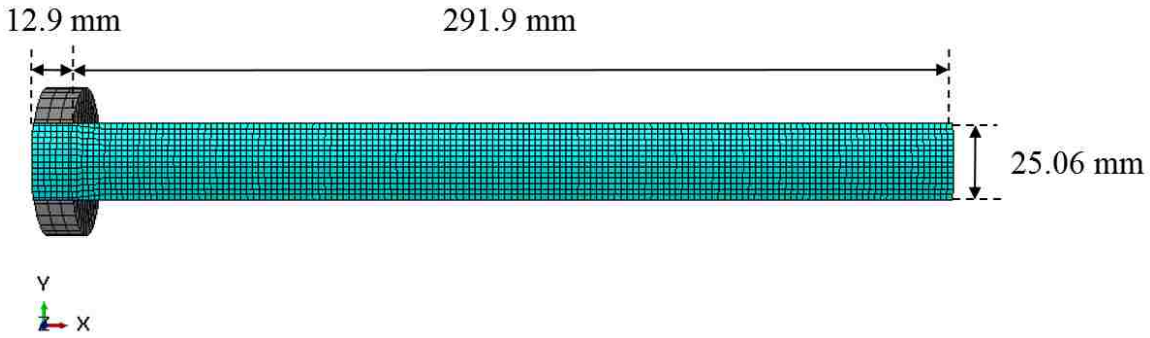

Figure 3.21: The model assembly consisting of tape spring and cylinder in Abaqus.

The first 12.9 mm of the tape spring was fixed using an encastre boundary condition throughout the entire simulation to represent the length of the tape spring that was held in place beneath the hose clamp during testing, shown in Figure 3.22.

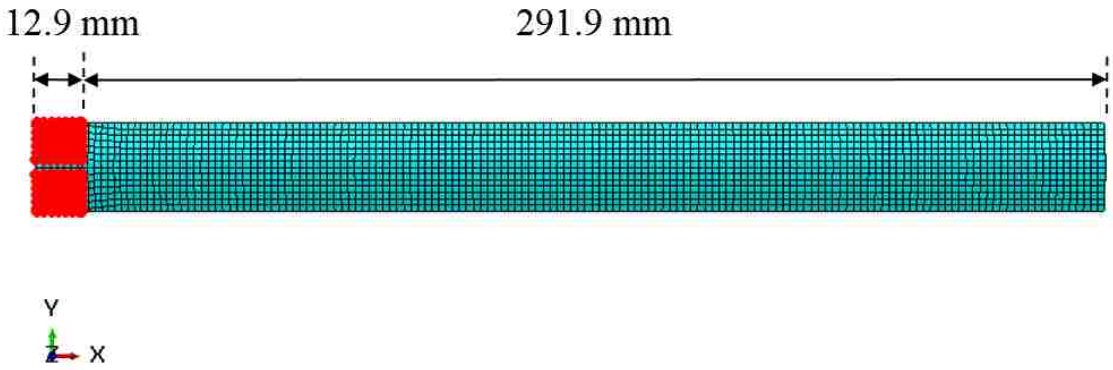

Figure 3.22: The fixed end boundary condition of tape spring defined in Abaqus.

It was observed experimentally that during deployment the bend in the tape spring did not travel beyond the lower 39 mm of the tape spring. Therefore, in the simulation, that length was held fix along the centerline of the tape spring during deployment, shown in Figure 3.23, to reproduce the behavior that was observed experimentally.

Figure 3.23. The fixed end of tape spring extended to replicate the travel range of the bend observed experimentally during deployment in Abaqus.

The center node at the deployable end of the tape spring was defined as Node A, shown in Figure 3.24. This node was used to assign folding displacements to the tape spring and to track rotational displacement during deployment.

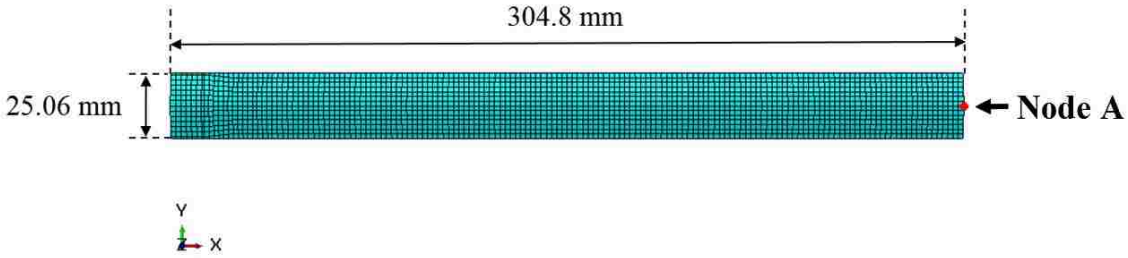

Figure 3.24: Node A used to track the deployment displacement of the tape spring in Abaqus.

The center node that was 57.47 mm from the deployable end of the tape spring was defined as the location that the screw was placed through the tape spring specimen experimentally to fix it in place during stowage, named Node B_1. Closer to the deployable end by 2 mm was Node B_2, shown in Figure 3.25. This node represented the surface area of the tape spring that became pressed against the head of the screw as it was tightened causing the free end of the tape spring to rest more vertically. During stowage, both Nodes B_1 and B_2

were assigned fixed boundary conditions. This was to ensure that no translation or rotation occurred at those locations, which represented the surrounding edges of the small hole that had been drilled into the tape spring. This fixed constraint was maintained experimentally using the small screw that passed through the hole of the tape spring and was secured into the ledge of the aluminum load cell plate.

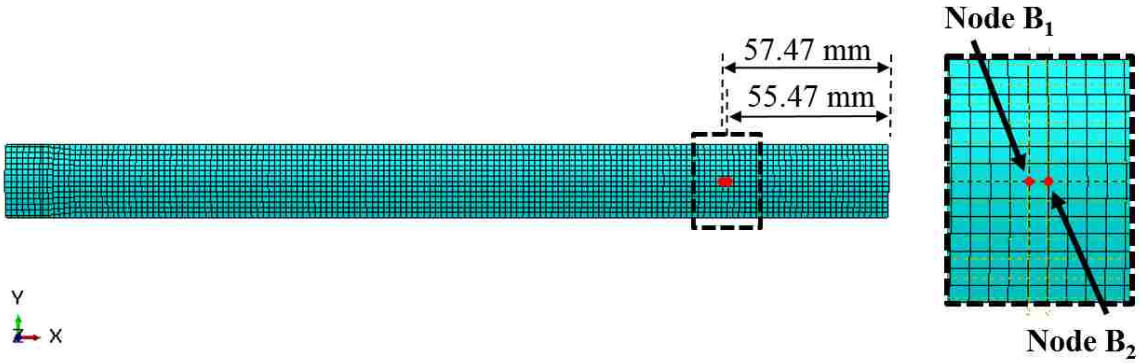

Figure 3.25: Nodes B_1 and B_2 used to represent screw placement in Abaqus.

The composite layup module was used to define three composite layers. The outer two were assigned the plain weave user-defined material (UMAT) definition, and the middle was assigned the unidirectional material definition. The overall thickness of the tape spring was 0.48 mm, and the plain weave layers were assumed to be twice as thick as the unidirectional layers due to the overlap of fibers created by the fabric weave geometry. Therefore, the plain weave and unidirectional laminae thicknesses were defined as 0.192 mm and 0.096 mm, respectively. The rotation angle of the outer plain weave layers was 45°, as shown in Figure 3.26.

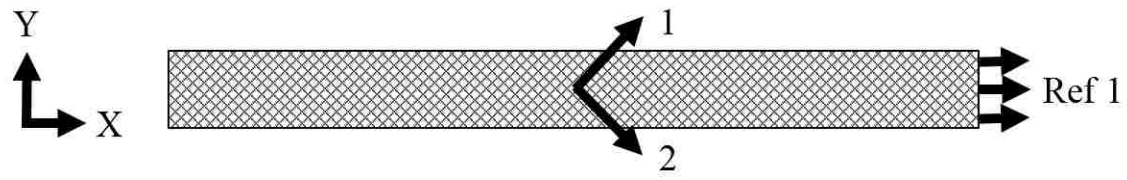

Figure 3.26: The plain weave plies material definition oriented $\pm 45°$ to the x-axis in Abaqus.

The rotation angle of the middle unidirectional layer was defined as 0°, as shown in Figure 3.27. The transverse shear stiffnesses, which are required for running the UMAT subroutine, were set to 919, 900, and 919 N/mm for K_{11}, K_{12}, and K_{22}, respectively.

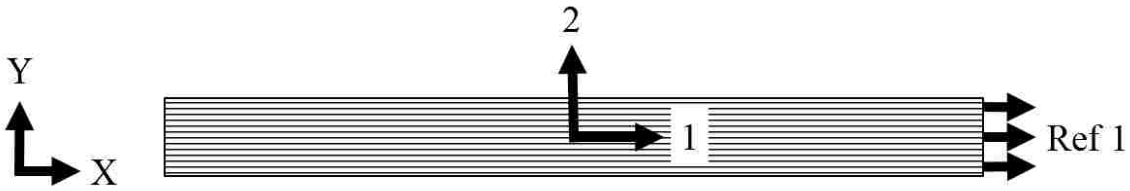

Figure 3.27: The unidirectional ply material definition orientated 0° to the x-axis in Abaqus.

The plain weave laminae material was created as a UMAT with six mechanical constants (the elastic modulus of the fibers in the *1* and *2* directions, the elastic modulus of the matrix, Poisson's ratio of the fibers and the matrix, and the fiber volume fraction of the composite) and 17 solution-dependent state variables (local lamina stresses in three directions, local lamina strains in three directions, the elastic and shear moduli of the matrix, the laminate elastic modulus, shear modulus, Poisson's ratio, the global lamina stresses in three directions, the global lamina strain in the x-direction, and the global strain energy density in the lamina). The unidirectional lamina material was defined as an *elastic lamina* with Rayleigh damping coefficients alpha (the mass proportional damping

coefficient) equal to the default value of 0.05 and beta (the stiffness proportional damping coefficient) equal to 0.0029 and a density of 1.5×10^{-9} tonne/mm^3. The stiffness proportional damping coefficient cannot be defined in user-defined materials, so only alpha was defined in the plain weave laminae.

In the initial step, the clamping of the tape spring with a natural diameter of 101.6 mm to an aluminum cylinder with a diameter of 50.8 mm was simulated. This was done by defining a node set consisting of the lower 12.9 mm of the tape spring to be used as *control points* and by constraining them to the outer face of the aluminum cylinder defined as the *surface* using the *adjust points* option in Abaqus.

The folding, stowage, and deployment phases took place over eight simulation steps. The folding was done over four quasi-static steps. First, Node A was displaced 30 mm in the negative z-direction, shown in Figure 3.28. Throughout all steps, Node A was fixed from translation in the y-direction, rotation around the x-axis, and rotation around the z-axis, referred to herein as the roller boundary condition.

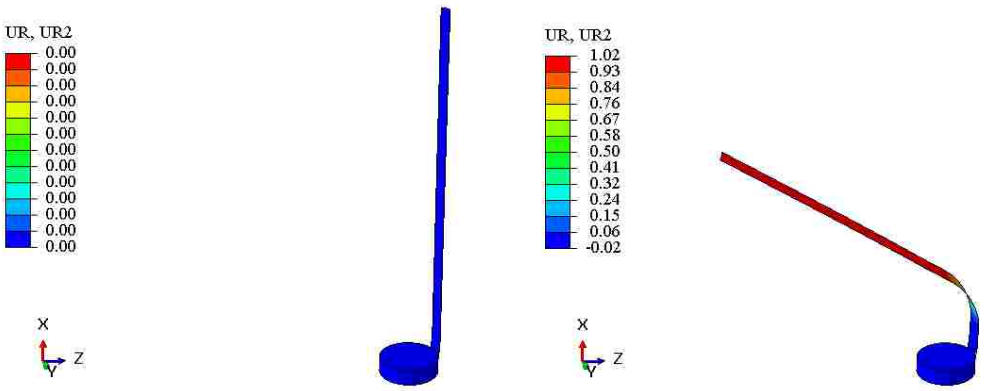

Figure 3.28: The first step of the folding sequence in Abaqus in which Node A was displaced 30 mm in the negative z-direction.

Second, Node A was displaced 150 mm in the negative x-direction, as shown in Figure 3.29(a). Once the general folded geometry had been achieved, Node B_1 could be positioned more specifically into place. In Step 3, Node B_1 was moved to a displaced location of 206 mm in the negative x-direction and 74 mm in the negative z-direction, as shown in Figure 3.29(b). This represented the natural geometry of the tape spring resting against the load cell plate.

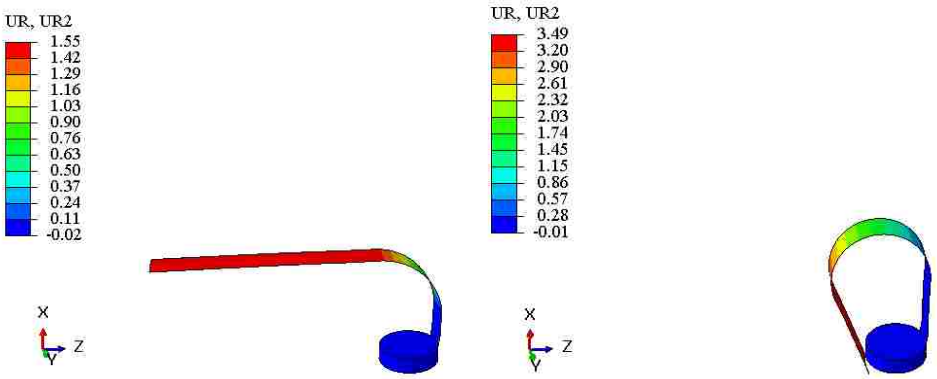

(a) (b)

Figure 3.29: (a) Step 2 of folding sequence in Abaqus with a displacement of Node A in the negative x-direction by 150 mm. (b) Step 3 of folding sequence with a displacement of Node A to a location of 206 mm in the negative x-direction and 74 mm in the negative z-direction.

Step 4 simulated the tightening of the head of the screw against the inner surface of the tape spring as it was screwed securely into the load cell boundary plate. As the head of the screw pushed against the lower edge of the tape spring hole in the negative z-direction, it caused the free end of the tape spring below the screw to become more vertical. To achieve this in the simulation, Node B_2 (representing the lower edge of the tape spring hole closer to the free end) was moved to the displaced position of 74 mm in the negative z-direction to produce the same bending curvature as that observed in the experimental specimen,

shown in Figure 3.30(a). The folded geometry was maintained throughout stowage. Stowage was simulated over one quasi-static step by holding Nodes B_1 and B_2 fixed at their current positions for 2.938×10^6 seconds (34 days). Then, the hold on Node B_2 was released to simulate the removal of the screw just prior to deployment, shown in Figure 3.30(b), allowing the tape spring to return to its natural bending configuration as it rested against the load cell plate ledge.

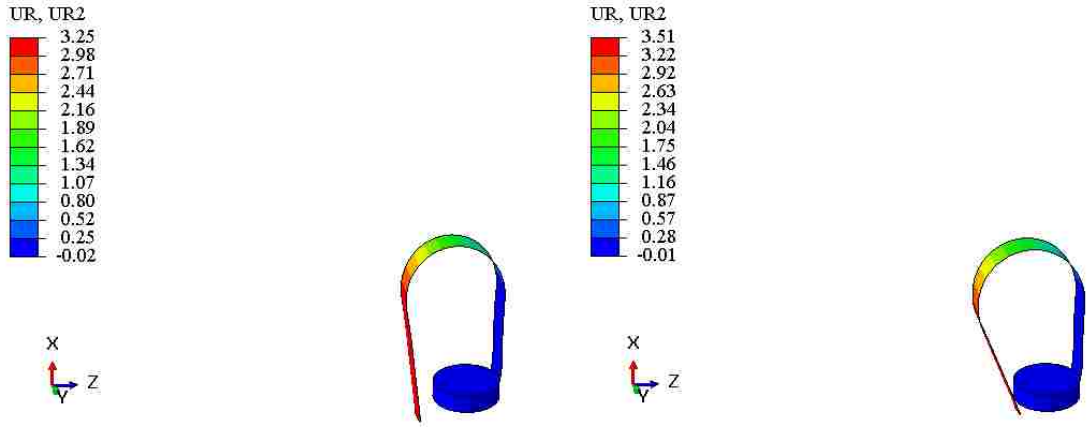

(a) (b)

Figure 3.30: (a) Step 4 of folding sequence in Abaqus representing the insertion of the securing screw to obtain the correct stowage geometry in preparation for the stowage Step 5. (b) Step 6 represented the removal of the screw just prior to deployment.

To avoid discrepancy between the model and experiment caused by the speed of travel of the load cell boundary condition during deployment, the deployment phase was broken into two steps. Step 7 represented a controlled deployment wherein Node A was displaced to a position of 280 mm in the negative x-direction and 170 mm in the negative z-direction. This was done to create the geometry that the tape spring achieved the moment the load cell plate cleared its path, shown in Figure 3.31(a), and was performed as a dynamic implicit analysis. Step 8 represented free deployment and was simulated over one dynamic

implicit step for 0.3 seconds by releasing all boundary conditions with the exception of the fixed end and the roller boundary condition. The final deployed geometry is shown in Figure 3.31(b). Throughout the simulation, a gravity load of 9,810 mm/s^2 was applied in the negative x-direction.

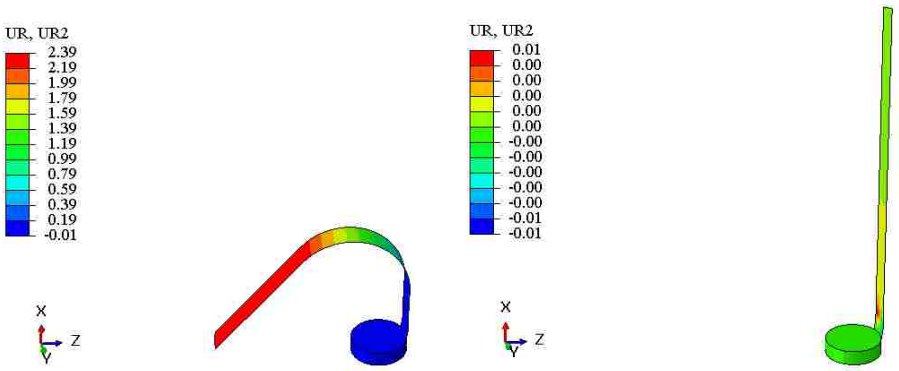

(a) (b)

Figure 3.31: (a) The geometry achieved after the controlled deployment of Step 7 in Abaqus. (b) The final deployed geometry after Step 8 of free deployment in Abaqus.

The screw boundary condition on the deployable end of the tape spring prevented the tape spring from sliding up slightly during stowage, and as such, a small force in the x-direction was expected. The reaction force in the x-direction at Node B_1 had a value of 0.133 N at the start of stowage, as shown in Figure 3.32, as expected.

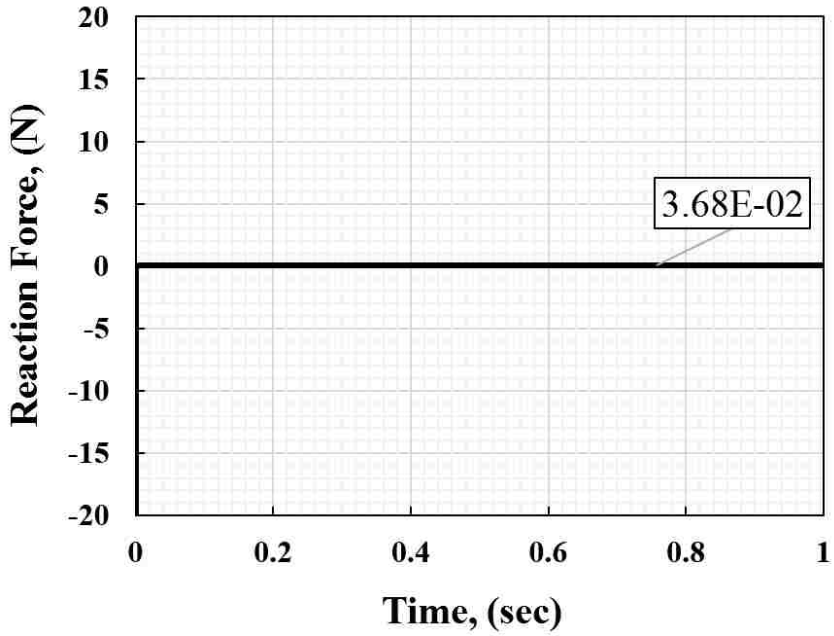

Figure 3.32. The reaction force in the x-direction at Node B_1 in the stowage configuration.

3.2.2 FINITE ELEMENT MODELING OF VISCOELASTICITY IN ABAQUS

The ability to model the viscoelastic stowage response and effect on deployment of a composite tape spring hinge is highly desired by the aerospace structures community, because large-scale, zero-gravity testing on deployable structures is not always possible. The commercially available finite element software package Abaqus has the capacity to model the viscoelastic properties of an isotropic material but not of more complex material types, such as orthotropic or anisotropic materials. In the FlexLam composite, it is assumed that the on-axis unidirectional middle ply does not contribute to the viscoelastic response of the tape spring, because the fibers do not experience stress relaxation. Therefore, viscoelasticity is only modeled in the outer plain weave plies. These plies are orthotropic

in nature, and their viscoelastic response can be model through the use of a UMAT subroutine.

3.2.2.1 User-Defined Material (UMAT) Subroutine

The time-dependent material properties of the outer plain weave plies were defined using a UMAT subroutine. The subroutine allowed for the plain weave laminae material properties to be calculated as a function of time and returned to ABAQUS at each analytical time increment to perform finite element analysis at the laminate level. This process, which simulated stress relaxation, is outlined in Figure 3.33.

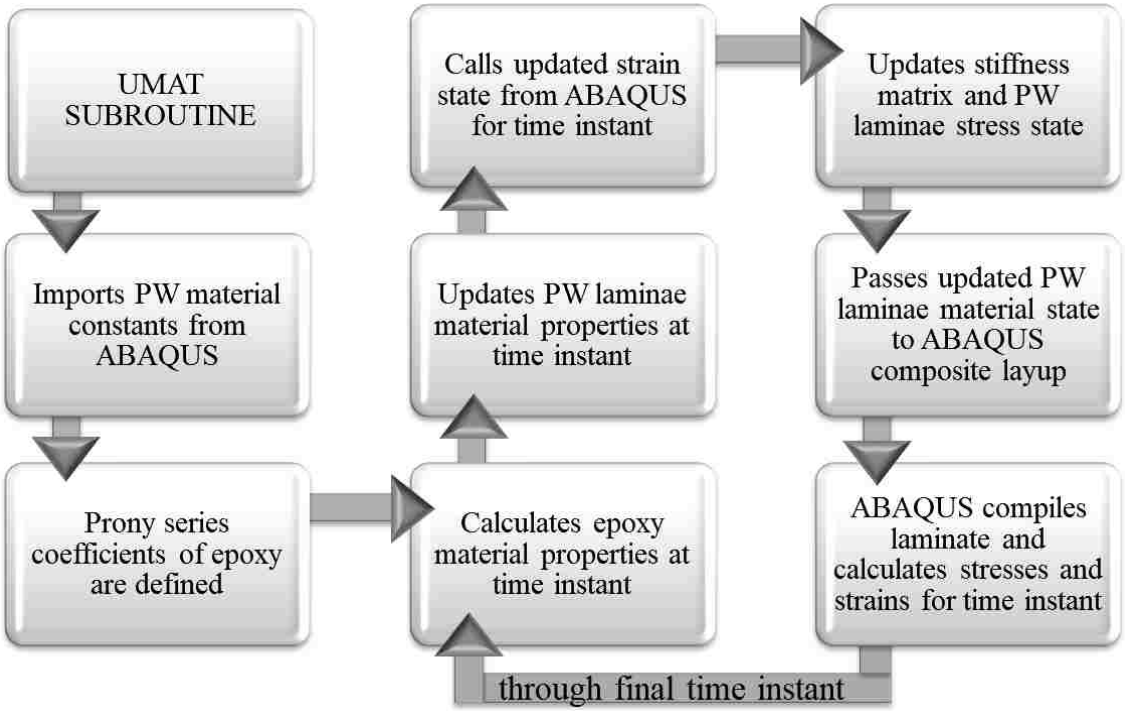

Figure 3.33: A flow chart of the UMAT process.

First, the Prony series terms b_i were calculated by defining the variables of time t_i, relaxation coefficient k_i, and relaxation time τ_i, where the decade increment is i and j is the analysis time increment:

$$b_i = k_i\left(1 - e^{-t_j/\tau_i}\right) \tag{3.6}$$

The relaxation modulus of the epoxy matrix with respect to time was defined in terms of the initial relaxation modulus of the epoxy matrix E_m, its initial elastic modulus E_{m0}, and the number of time decades *N*:

$$E_m(t) = E_{m0}\left(1 - \sum_{i=1}^{N} b_i\right) \tag{3.7}$$

The shear modulus of the epoxy matrix G_m with respect to time was defined in terms of a constant Poisson's ratio of the epoxy matrix ν_m:

$$G_m(t) = \frac{E_m(t)}{2(1+\nu_m)} \tag{3.8}$$

The constant shear modulus of the fibers G_f was defined in terms of the elastic modulus of the fibers in the principle fiber direction E_{1f} and a constant Poisson's ratio of the fibers ν_f:

$$G_f = \frac{E_{1f}}{2\left(1+\nu_f\right)} \tag{3.9}$$

The elastic modulus of the lamina in the *1*-direction (principle fiber direction) $E_1(t)$ and *2*-direction (transverse fiber direction) $E_2(t)$ were defined in terms of the fiber volume fraction V_f and the elastic modulus of the fibers in the transverse fiber direction E_{2f}:

$$E_1(t) = 0.5V_f\left(E_{1f} + E_{2f}\right) + E_m\left(1 - V_f\right) \tag{3.10}$$

$$E_2(t) = E_1(t) \tag{3.11}$$

The in-plane shear modulus of the lamina G_{12} was defined using the Chamis model (Younes, 2012):

$$G_{12}(t) = \frac{G_m(t)}{1 - \sqrt{V_f}\left(1 - \frac{G_m(t)}{G_f}\right)} \tag{3.12}$$

Poisson's ratio of the plain weave lamina when loaded in the major fiber direction ν_{12} was defined as:

$$\nu_{12} = (1 - V_f)\nu_m + V_f\nu_f \tag{3.13}$$

Poisson's ratio of the plain weave lamina when loaded perpendicular to the major fiber direction ν_{21} was defined as:

$$\nu_{21} = \nu_{12}\frac{E_2}{E_1} \tag{3.14}$$

The subroutine was written in FORTRAN, wherein the strain variable ε_l was the current log-strain and $\Delta\varepsilon_l$ was the incremental change in strain. Therefore, the local strain at each time increment ε_a was calculated as:

$$\varepsilon_a = \varepsilon_l + \Delta\varepsilon_l \tag{3.15}$$

where $a = 1{:}\,3$, representing the three principle directions. In order to update the stress, the Jacobian matrix needed to be defined, representing an incremental change in stress divided by an incremental change in strain. Recalling the *reduced stiffness matrix* from Eq. 2.55:

$$\begin{Bmatrix}\sigma_1\\ \sigma_2\\ \tau_{12}\end{Bmatrix} = \begin{bmatrix}Q_{11} & Q_{12} & 0\\ Q_{12} & Q_{22} & 0\\ 0 & 0 & Q_{66}\end{bmatrix}\begin{Bmatrix}\varepsilon_1\\ \varepsilon_2\\ \gamma_{12}\end{Bmatrix} \tag{3.16}$$

where:

$$Q_{11} = \frac{E_1}{1 - \upsilon_{12}\upsilon_{21}}$$

$$Q_{12} = \frac{\upsilon_{12}E_2}{1 - \upsilon_{12}\upsilon_{21}} \tag{3.17}$$

$$Q_{22} = \frac{E_2}{1 - \upsilon_{12}\upsilon_{21}} \tag{3.18}$$

$$Q_{66} = G_{12} \tag{3.19}$$

By multiplying the updated local strain by an incremental change in stress divided by an incremental change in strain, the resultant is the updated local stress. The reduced stiffness matrix was used to define the tangent stiffness matrix, *i.e.* the Jacobian matrix J_{ab} required for calculating the updated local stress state:

$$J_{ab} = \begin{bmatrix} \frac{E_1}{1-\upsilon_{12}\upsilon_{21}} & \frac{\upsilon_{12}E_2}{1-\upsilon_{12}\upsilon_{21}} & 0 \\ \frac{\upsilon_{12}E_2}{1-\upsilon_{12}\upsilon_{21}} & \frac{E_2}{1-\upsilon_{12}\upsilon_{21}} & 0 \\ 0 & 0 & G_{12} \end{bmatrix} \tag{3.20}$$

The local stress matrix was calculated by multiplying the updated local strain matrix by the reduced stiffness matrix, such that:

$$\sigma_1 = \varepsilon_1 J_{11} + \varepsilon_2 J_{12} \tag{3.21}$$

$$\sigma_2 = \varepsilon_1 J_{21} + \varepsilon_2 J_{22} \tag{3.22}$$

$$\tau_{12} = \gamma_{12} J_{33} \tag{3.23}$$

To investigate the global response of the lamina, the global stress and strain values had to be calculated using the *inverse transformation matrix* described in Eq. 2.57:

$$\begin{Bmatrix} \sigma_x \\ \sigma_y \\ \tau_{xy} \end{Bmatrix} = \begin{bmatrix} m^2 & n^2 & -2mn \\ n^2 & m^2 & 2mn \\ mn & -mn & m^2 - n^2 \end{bmatrix} \begin{Bmatrix} \sigma_1 \\ \sigma_2 \\ \tau_{12} \end{Bmatrix} \tag{3.24}$$

where $m = cos(\theta)$ and $n = sin(\theta)$. In this way, the local stress values were transformed to the global stress values specifically for a $\pm 45°$ plain weave lamina, such that:

$$\sigma_x = \frac{\sigma_1}{2} + \frac{\sigma_2}{2} - \tau_{12} \tag{3.25}$$

$$\sigma_y = \frac{\sigma_1}{2} + \frac{\sigma_2}{2} + \tau_{12} \tag{3.26}$$

$$\tau_{xy} = \frac{\sigma_1}{2} - \frac{\sigma_2}{2} \tag{3.27}$$

Then the local strain was transformed to the global strain in the x-direction for a $\pm 45°$ plain weave lamina in the same manner:

$$\begin{Bmatrix} \varepsilon_x \\ \varepsilon_y \\ \frac{1}{2}\gamma_{xy} \end{Bmatrix} = \begin{bmatrix} m^2 & n^2 & -2mn \\ n^2 & m^2 & 2mn \\ mn & -mn & m^2 - n^2 \end{bmatrix} \begin{Bmatrix} \varepsilon_1 \\ \varepsilon_2 \\ \frac{1}{2}\gamma_{12} \end{Bmatrix} \tag{3.28}$$

such that:

$$\varepsilon_x = \frac{1}{2}\varepsilon_1 + \frac{1}{2}\varepsilon_2 - \frac{1}{2}\gamma_{12} \tag{3.29}$$

Finally, the global strain energy density U was calculated in the plain weave lamina:

$$U = \frac{\sigma_x \times \varepsilon_x}{2} \tag{3.30}$$

In FORTRAN, $STATEV$ defines a solution-dependent state variable that is updated every time the UMAT is called and is used to define custom variables of interest to the user. In this UMAT subroutine, those variables included local stress, local strain, the elastic modulus of the matrix with respect to time, the shear modulus of the matrix with respect to time, the elastic modulus of the lamina, the shear modulus of the lamina, Poisson's ratio of the lamina, the global stress, the global strain in the x-direction, and the global strain energy density:

$$STATEV(1) = \sigma(1) \tag{3.31}$$

$$STATEV(2) = \sigma(2) \tag{3.32}$$

$$STATEV(3) = \sigma(3) \tag{3.33}$$

$$STATEV(4) = \varepsilon(1) \tag{3.34}$$

$$STATEV(5) = \varepsilon(2) \tag{3.35}$$

$$STATEV(6) = \varepsilon(3) \tag{3.36}$$

$$STATEV(7) = E_m(t) \tag{3.37}$$

$$STATEV(8) = G_m(t) \tag{3.38}$$

$$STATEV(9) = E_1 \tag{3.39}$$

$$STATEV(10) = E_2 \tag{3.40}$$

$$STATEV(11) = G_{12} \tag{3.41}$$

$$STATEV(12) = \nu_{12} \tag{3.42}$$

$$STATEV(13) = \sigma_x \tag{3.43}$$

$$STATEV(14) = \sigma_y \tag{3.44}$$

$$STATEV(15) = \tau_{xy} \tag{3.45}$$

$$STATEV(16) = \varepsilon_x \tag{3.46}$$

$$STATEV(17) = U \tag{3.47}$$

The state dependent variables were collected and reported as output for the user but were not used by Abaqus for any additional calculations. The stress and strain values continued to be passed between the UMAT and Abaqus at each time increment until the final time increment had been completed.

UMAT subroutines include some limitations. For example, to avoid convergence issues, the stress state at the start of each new analysis step is taken as that at the start of the previous analysis step. Therefore, a UMAT subroutine can calculate stress relaxation behavior for the duration of a single analysis step, such as the stowage step, but at the start of the following step, the material properties will be returned to their original values, as though time had been set back to zero. For that reason, the material properties for the deployment step were calculated using MatLab and were fed directly to Abaqus as an elastic lamina material definition for the final deployment analysis (Step 8). The flowchart

presented in Figure 3.34 outlines the use of the UMAT for the first seven analysis steps followed by a constant material definition calculated by MatLab for the correct analysis time applied for the analysis of the final deployment step.

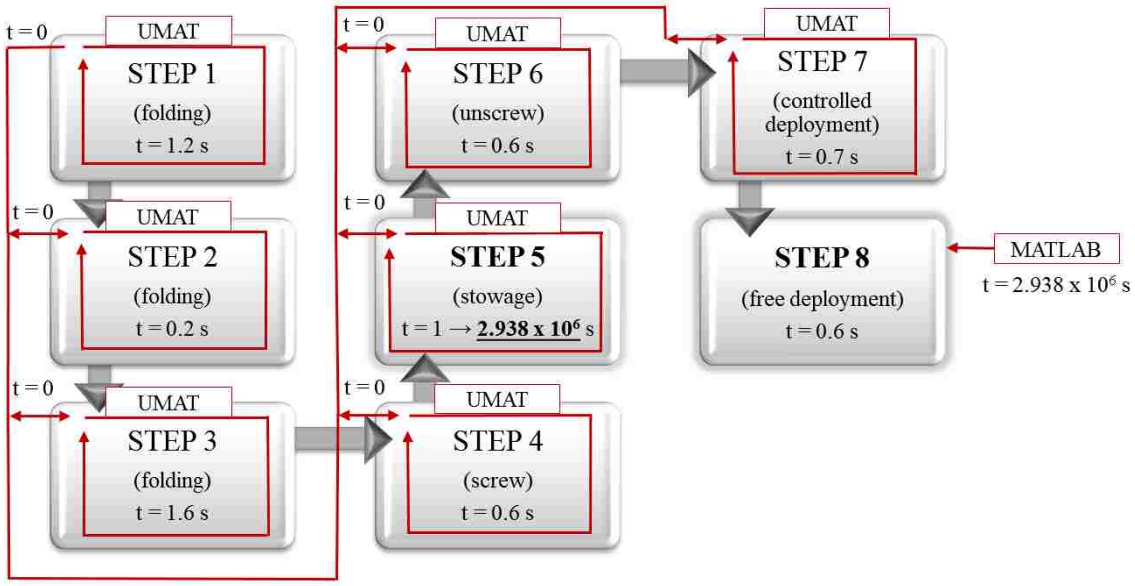

Figure 3.34. A flow chart showing the use of the UMAT for each of the first seven steps in Abaqus followed by a constant material definition calculated in MatLab and fed into Abaqus for the completion of Step 8.

If the UMAT calculated the relaxation modulus of the epoxy matrix for a stowage period of 2.938×10^6 seconds (34 days), the relaxation modulus would return back to its initial modulus value at the start of the next analysis step, as shown in Figure 3.35. For this reason, the UMAT can be used to analyze the effects of viscoelasticity throughout the stowage step, but in order to analyze the effects of viscoelasticity on deployment, the material properties for the time instant following the correct stowage time period must be calculated using the same equations as those defined in the UMAT and entered into Abaqus manually as constant material properties to complete the deployment analysis.

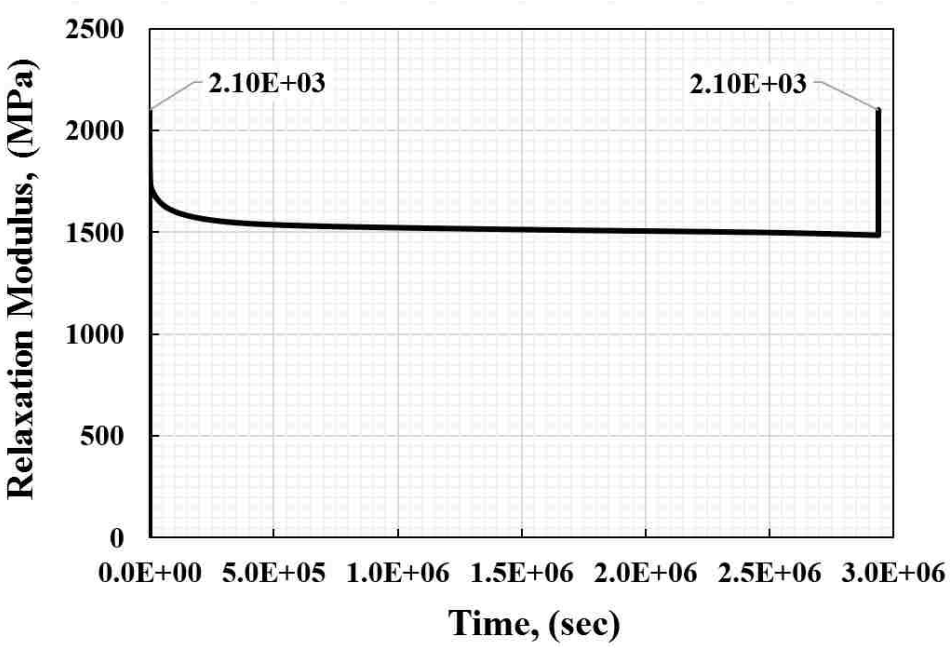

Figure 3.35. Example of the reset of relaxation modulus that occurs after the completion of stowage at the start of Step 6.

3.2.2.2 UMAT Verification

The UMAT subroutine verification is reported in a journal paper by Khan et al. (2017). The subroutine was used to simulate creep of a 45° off-axis unidirectional glass fiber lamina that had been experimentally tested in tension with an applied stress of 4.25 ksi to measure creep over 1,200 seconds by Haj-Ali and Muliana (2008). The numerical results using the subroutine matched the published experimental results with good accuracy. For more information, please refer to Khan et al. (2017).

CHAPTER 4 RESULTS AND DISCUSSION

4.1 MATERIAL CHARACTERIZATION RESULTS

Material characterization testing was completed for the unidirectional carbon fiber composite lamina, the plain weave carbon fiber composite laminae, and the epoxy component of the plain weave laminae. Material properties that were not determined experimentally were provided by the material manufacturers or obtained from the Autodesk Simulation Composite Design material library. The final material properties that were defined as inputs in the finite element simulation are consolidated and reported below.

4.1.1 TENSION TEST RESULTS

Through tension testing of the plain weave IM7 carbon fiber composite coupons, material properties, including strength, elastic and shear moduli, and Poisson's ratio, were determined. The resultant material properties are displayed in Table 3.

Table 3: Material properties of the plain weave IM7 composite coupon determined experimentally.

Plain Weave IM7						
Specimen	S_{11} *(MPa)*	S_{12} *(MPa)*	E_{11} *(GPa)*	E_{22} *(GPa)*	ν_{12}	G_{12} *(GPa)*
1	543.7	64.3	33.6	33.6		4.79
2	905.2	82.4	57.5	57.5		8.16
3	582.9	70.1	48.1	48.1	0.07	4.97
4	608.5	65.7	34.0	34.0	0.17	7.64
5	609.6	73.9	49.0	49.0	0.16	7.37
Average	**650.0**	**71.3**	**44.5**	**44.5**	**0.13**	**6.59**

The ultimate tensile strength S_{11} was determined from on-axis testing to be 650.0 MPa, and the ultimate in-plane shear strength S_{12} was found from off-axis testing to be 71.3 MPa. The elastic modulus in the fill tow E_{11} and the warp tow E_{22} directions were found to be

44.5 GPa from on-axis testing. The fill and warp directions were assumed to be equivalent, because the fibers were the same in both directions. A standard stress versus strain plot from which the elastic modulus was determined for the plain weave composite material is shown in Figure 4.1.

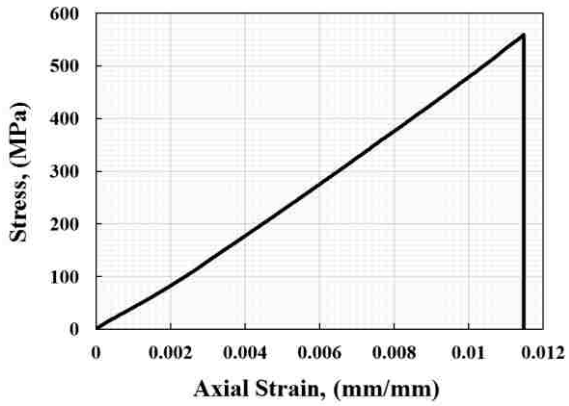

Figure 4.1: The stress versus strain results for the plain weave IM7 carbon fiber composite coupon (specimen #3) tested in on-axis tension.

Poisson's ratio ν_{12} was found to be 0.13 from on-axis testing, and a standard transverse strain versus axial strain plot from which Poisson's ratio was determined for the plain weave composite material is shown in Figure 4.2.

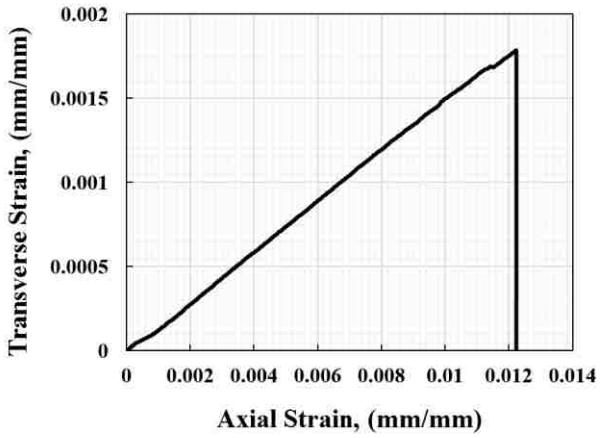

Figure 4.2: The transverse strain versus axial strain results for the plain weave IM7 carbon fiber composite coupon (specimen #5) tested in on-axis tension.

The in-plane shear modulus G_{12} was found to be 6.59 GPa from off-axis tension testing. A standard shear stress versus shear strain plot from which the shear modulus was determined for the plain weave composite material is shown in Figure 4.3.

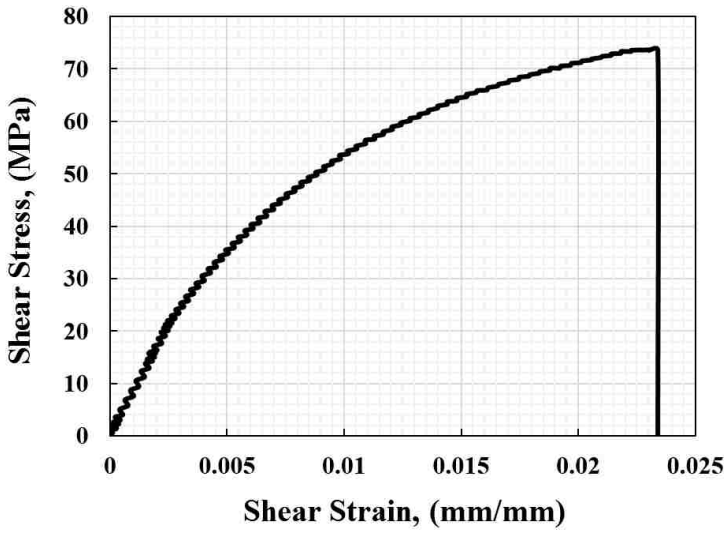

Figure 4.3: The shear stress versus shear strain results for the plain weave IM7 carbon fiber composite coupon (specimen #5) tested in off-axis tension.

Through tension testing of the unidirectional IM7 carbon fiber composite coupons, material properties, including tensile strength, elastic modulus, and Poisson's ratio, were determined. As a result of challenges preventing the cutting of the unidirectional carbon fiber coupons at any orientation other than on-axis (in the case of 90° orientation, the coupons came apart entirely during cutting due to separation between the fibers), only on-axis testing of the unidirectional material could be performed. The resultant material properties for the unidirectional IM7 carbon fiber composite are shown in Table 4.

Table 4: Material properties of the unidirectional IM7 composite coupon determined experimentally.

Unidirectional IM7						
Specimen	S_{11} *(GPa)*	S_{12}	E_{11} *(GPa)*	E_{22}	ν_{12}	G_{12} *(GPa)*
1	1.85		136.1			
2	1.34		136.6			
3	1.93		118.4			
4	2.00		113.6			
5	1.55		136.1			
7	1.36		131.2		0.29	
8	1.76		107.9		0.25	
Average	**1.67**		**122.2**		**0.27**	

The ultimate tensile strength S_{11} of the unidirectional composite material was found to be 1.67 GPa, about two and a half times that of the plain weave composite material. This was expected, because the unidirectional material had all of its fibers oriented in the direction of applied tension, while the plain weave material only had half. The elastic modulus of the unidirectional composite material in the fill tow direction was found to be 122.20 GPa, more than two and a half times that of the plain weave composite material. Slightly less axial strain was observed in the unidirectional composite material, and it was capable of achieving much higher stresses than the plain weave material, resulting in a higher elastic modulus. A typical stress versus strain plot from which the elastic modulus was determined for the unidirectional IM7 carbon fiber composite material is shown in Figure 4.4.

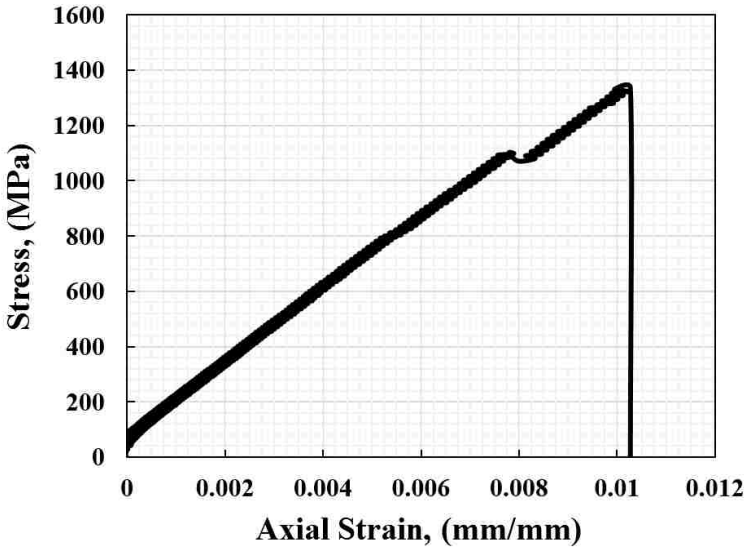

Figure 4.4: The stress versus strain plot for the unidirectional IM7 carbon fiber composite coupon (specimen #2) tested in on-axis tension.

Poisson's ratio ν_{12} of the unidirectional composite material was found to be 0.27. Due to challenges presented by the superglue and solder used to attach the strain gages and the limited availability of the material, only two unidirectional specimens were successfully tested for Poisson's ratio, both reporting similar values. The unidirectional material achieved higher transverse strain (likely due to the absence of transverse fiber reinforcement) and slightly less axial strain than the plain weave material, resulting in a higher Poisson's ratio. A typical transverse strain verses axial strain plot from which Poisson's ratio was determined for the unidirectional IM7 carbon fiber composite material is shown in Figure 4.5.

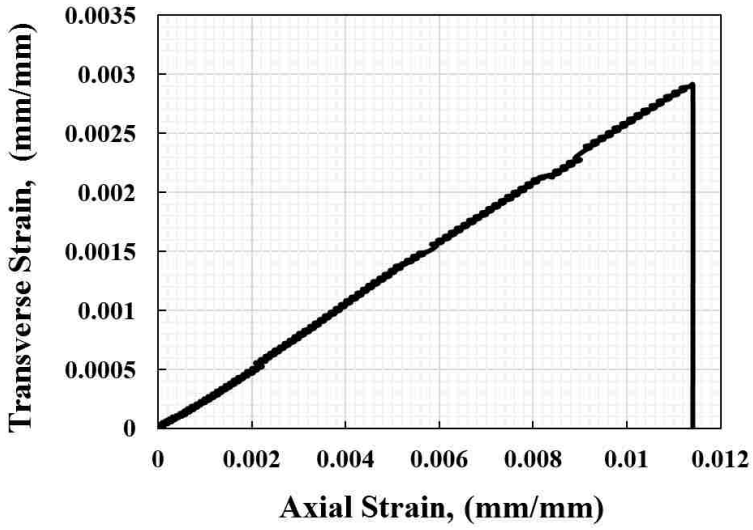

Figure 4.5: The transverse strain versus axial strain plot of the unidirectional IM7 carbon fiber composite coupon (specimen #8) tested in on-axis tension.

4.1.2 FIBER VOLUME FRACTION RESULTS

Fiber volume fraction tests were performed on the final tape spring laminate material following ASTM D3171–15. Results from the fiber volume fraction test are shown in Table 5, including the dimensions, volume, mass, density, and fiber volume fraction of each specimen. The testing results report an average fiber volume fraction of 0.53 for the three-ply FlexLam composite laminate.

Table 5: Fiber volume fraction results for FlexLam tape spring material.

Specimen	*l (mm)*	*w (mm)*	*t (mm)*	*V (mm^3)*	*M_i (g)*	*M_f (g)*	*ρ_c (g/mm^3)*	*ρ_f (g/mm^3)*	*V_r*
1	26	24	0.49	305.8	0.46	0.29	0.0015	0.00178	53.14
2	27	25	0.51	344.3	0.50	0.32	0.0014	0.00178	51.94
3	27	26	0.48	337.0	0.50	0.31	0.0015	0.00178	52.29
4	25	24	0.49	294.0	0.45	0.29	0.0015	0.00178	55.09
Average	**26**	**25**	**0.49**	**320.2**	**0.48**	**0.30**	**0.0015**	**0.00178**	**53.11**

4.1.3 VISCOELASTICITY TEST RESULTS

Stress relaxation testing using the DMA was performed on the Patz Materials & Technologies PMT-F7 epoxy resin. The results of the stress relaxation tests at each applied temperature after shifting to a reference temperature of $30°C$ in accordance with the TTSP are shown in Figure 4.6.

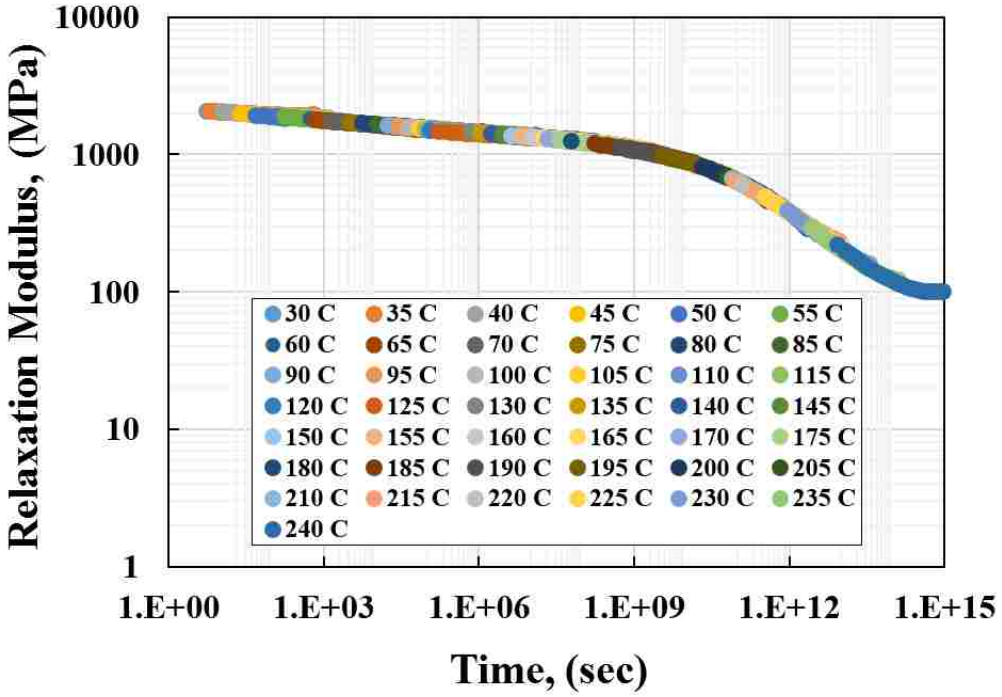

Figure 4.6: Master curve of Patz PMT-F7 epoxy resin at $30°C$. Results courtesy of Amy Garner (Garner et al., 2015).

The Prony series coefficients representing the stress relaxation of the Patz PMT-F7 epoxy resin were determined through curve fitting in MatLab. The fit is shown in Figure 4.7.

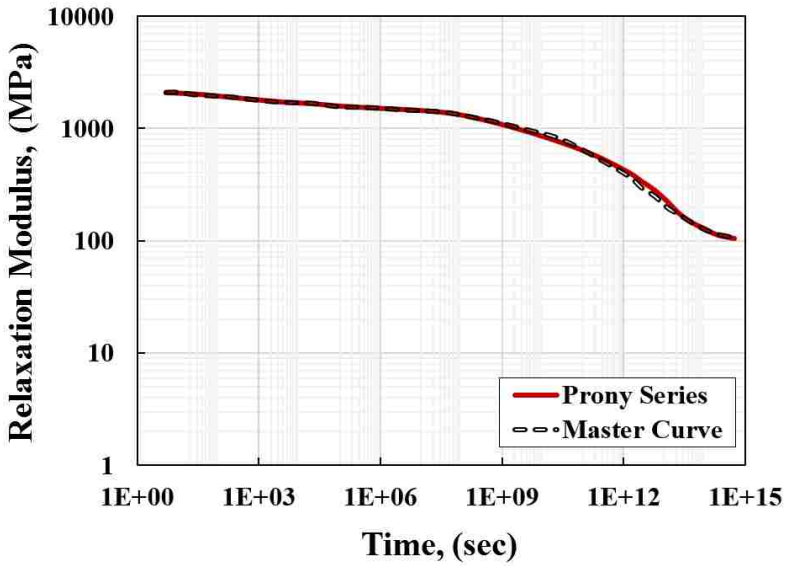

Figure 4.7: The Prony series curve fit to the Patz PMT-F7 epoxy resin master curve expanded to fourteen terms.

Fourteen relaxation coefficients k_i and fourteen relaxation times τ_i were determined to reflect the fourteen decades of time represented by the master curve. The resultant Prony series coefficients are shown in Table 6.

Table 6: Prony series relaxation coefficients k_i and relaxation times τ_i for the Patz Material & Technologies PMT-F7 epoxy resin.

k_1	0.025	τ_1	1.89 E+01
k_2	0.065	τ_2	1.00 E+02
k_3	0.085	τ_3	1.00 E+03
k_4	0.037	τ_4	2.00 E+04
k_5	0.053	τ_5	1.00 E+05
k_6	0.031	τ_6	1.95 E+06
k_7	0.024	τ_7	1.77 E+07
k_8	0.100	τ_8	1.74 E+08
k_9	0.100	τ_9	1.38 E+09
k_{10}	0.100	τ_{10}	1.00 E+10
k_{11}	0.100	τ_{11}	1.00 E+11
k_{12}	0.100	τ_{12}	1.00 E+12
k_{13}	0.100	τ_{13}	1.00 E+13
k_{14}	0.030	τ_{14}	1.00 E+14

4.1.4 RAYLEIGH DAMPING

Damping describes the decay in amplitude of oscillations due to energy dissipation (Chopra, 2012). In an oscillating tape spring, for example, possible energy dissipation mechanisms include a thermal effect resulting from repetitive elastic straining and small amounts of internal friction caused by repetitive deformation. Structurally, on a very small scale, there could be minor friction between the steel clamp, the aluminum cylinder, and the tape spring. Air resistance contributes to damping, as well. Without defining a damping mechanism in a finite element simulation, oscillations do not decay, and that does not represent reality. Unfortunately, damping coefficients cannot be calculated on a structure by structure basis, so determination of damping coefficients is often done by performing vibration experiments and through model calibration to achieve a rough estimate of the damping values. Although the UMAT is responsible for simulating the damping that occurs due to energy dissipation caused by stress relaxation during stowage, addition damping occurs in the first fraction of a second of deployment. This is due to the resistance of the material to rapid deformation. This type of energy dissipation is not represented by stress relaxation, which occurs over long periods of time in constant strain environments and is captured by the UMAT. Therefore, additional damping parameters needed to be defined in addition to the use of the UMAT subroutine. Bulk viscosity at the mesh element level was not defined.

In Abaqus, *structural* damping can only be defined if displacement and velocity are exactly 90° out of phase from one another for the entirety of the analysis. Since that was not an option for this analysis, Rayleigh damping was applied instead, although it is not an exact representation of the damping that occurred in the system. Rayleigh damping

coefficients alpha (the mass proportional damping coefficient) and beta (the stiffness proportional damping coefficient) were determined through model calibration. The default for alpha in Abaqus is 0.05 and for beta is zero. An alpha value of less than 2.5 is considered to represent minor damping.

In the finite element model, alpha was left as its default value, and beta was adjusted to calibrate the model to the Phase Two experimental deployment results, as shown in Figure 4.8. Very subtle changes in the beta value had a very noticeable effect on deployment behavior following the second rebound of the tape spring. A beta value of 0.0029 followed the trajectory of the tape spring during experimental deployment closely for the first 0.15 seconds of deployment, or until the fourth rebound, (longer than the surrounding beta values). Therefore, the beta value of 0.0029 was determined from composite model calibration.

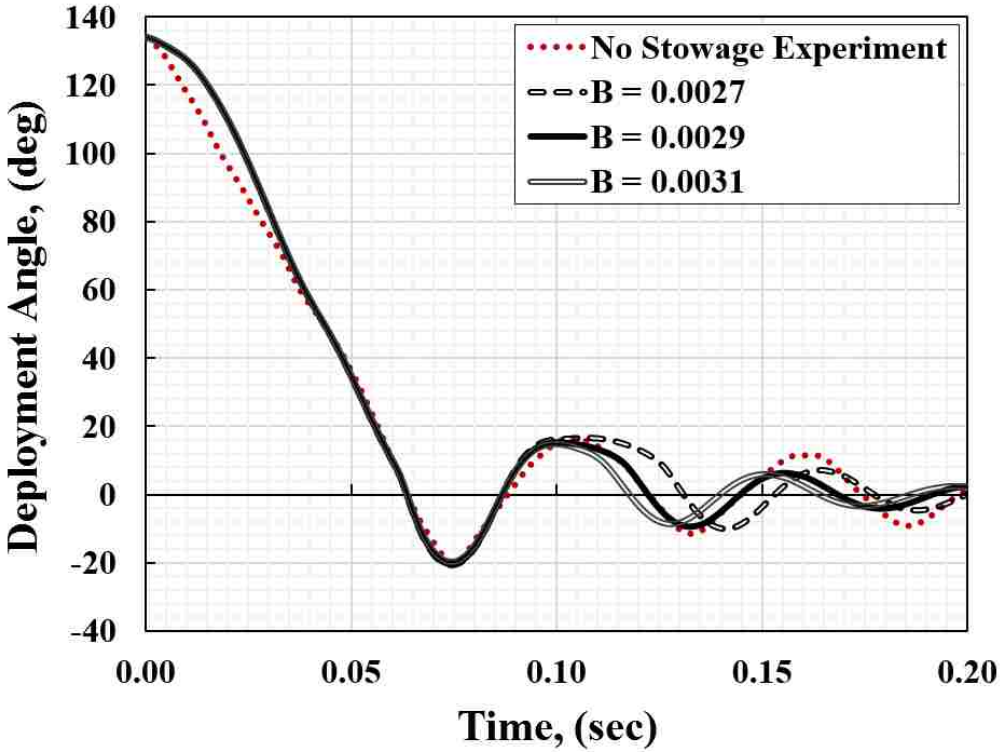

Figure 4.8: Finite element model calibration using Rayleigh damping coefficient beta.

For modal damping, the Abaqus manual reports the use of the following equation:

$$\xi_j = \frac{\alpha}{2\omega_j} + \frac{\beta\omega_j}{2} \tag{4.1}$$

where ξ is the viscous damping factor and ω is the natural frequency of vibration. The tape spring's natural vibration was determined by creating a linear perturbation frequency analysis in Abaqus. Figure 4.9 shows the first ten frequencies determined from the analysis.

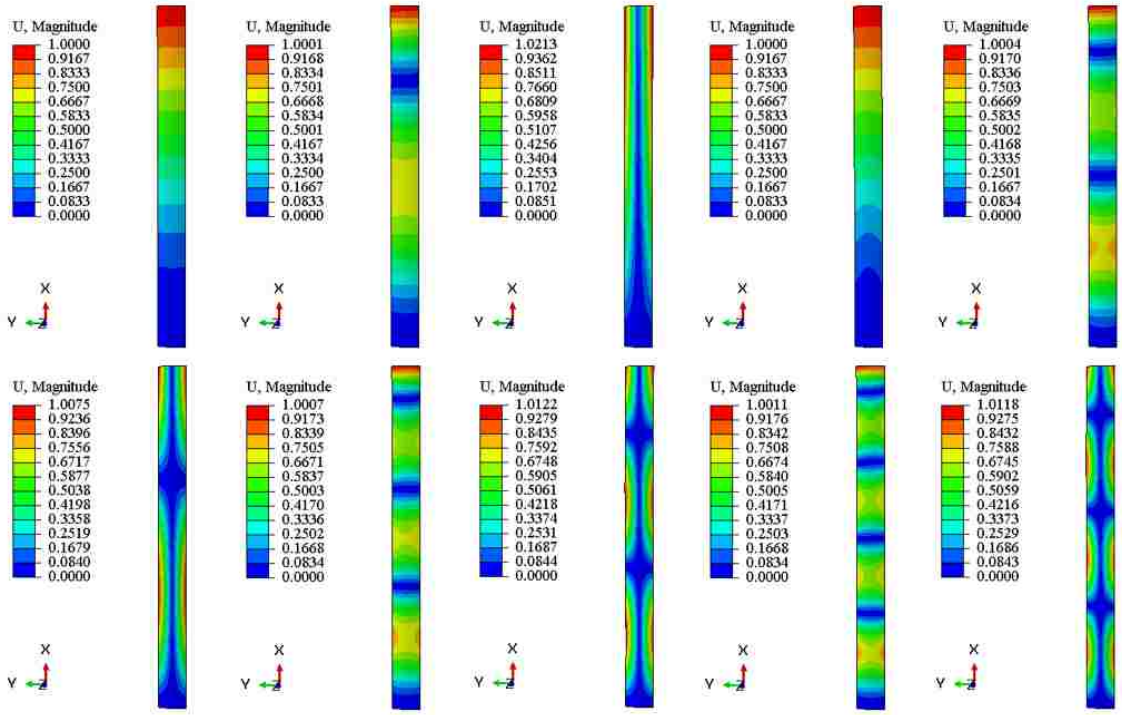

Figure 4.9. The first ten frequencies of the tape spring specimen without a hole determined in Abaqus.

A linear perturbation frequency analysis was also performed on a modeled tape spring with a 4.40 mm diameter hole representing the small hole that was present in the tape spring specimens tested experimentally to secure them with a screw during stowage. This additional analysis was completed to investigate whether or not the hole would have a

noticeable effect on the natural frequency of the tape spring. The results are shown in Figure 4.10.

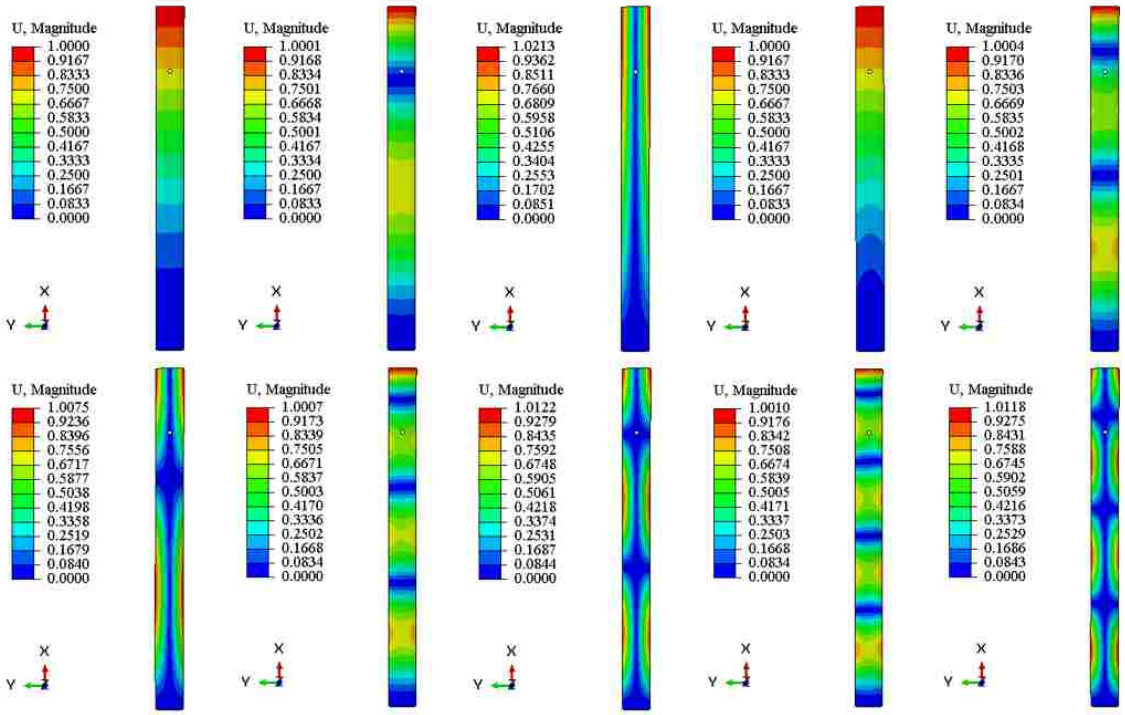

Figure 4.10: The first ten frequencies of the tape spring specimen with a hole determined in Abaqus.

Table 7 provides a comparison of the frequency values determined for the tape spring both without and with a hole. The results show a slightly higher value for the Mode I fundamental frequency of the tape spring with a hole (13.83 Hz versus 13.81 Hz), which might be explained by the slight decrease in mass of the specimen with a hole. Based on these results, a viscous damping factor of 0.02 was applied to the Abaqus finite element model. The alpha and beta values were determined through model calibration to be 0.05 and 0.0029, respectively.

Table 7. Linear perturbation frequency analysis results showing the case of the tape spring without a hole on the left and the case of the tape spring with a hole on the right.

Mode	Value	Frequency (cycles/s)
1	7.533 E+03	13.81
2	2.943 E+05	86.34
3	6.867 E+05	131.89
4	1.801 E+06	213.90
5	2.288 E+06	240.75
6	6.253 E+06	398.00
7	8.670 E+06	468.62
8	1.748 E+07	665.33
9	2.321 E+07	766.83
10	3.464 E+07	936.78

Mode	Value	Frequency (cycles/s)
1	7.551 E+03	13.83
2	2.928 E+05	86.12
3	6.867 E+05	131.89
4	1.806 E+06	213.90
5	2.267 E+06	239.62
6	6.236 E+06	397.44
7	8.572 E+06	465.96
8	1.737 E+07	663.34
9	2.298 E+07	762.98
10	3.453 E+07	935.21

One of the limitations of using a Rayleigh damping definition to represent damping of the tape spring during deployment is that it does not fully capture the material resistance to rapid deformation, which occurs early in the initial deployment stage when the fold in the tape spring travels slightly upward and during the slight inversion of the transverse curvature that occurs during snapback or overshoot. Rayleigh damping is, however, able to capture the effects of air resistance on tape spring deployment and the tendency of the tape spring stiffness to cause it to recover into its straight equilibrium position, but it does not fully capture the material resistance to rapid deformation.

The tape spring deployment behavior following a 34-day stowage period incorporating energy dissipation mechanisms of the UMAT subroutine and the Rayleigh damping definition is displayed in Figure 4.11. The results show that the Rayleigh damping definition does not have an effect on the initial deployment rate, but the UMAT subroutine

does. The UMAT determined the dissipation of stored energy during stowage caused by stress relaxation, which resulted in less available energy at the start of deployment. In this way, the deployment results incorporating the UMAT show deployment occurring at a slower rate, but after the first rebound, the UMAT does not offer any additional damping. This is because stress relaxation does not occur during the state of dynamic deployment wherein strain is constantly changing and which only lasts a few seconds. The Rayleigh damping definition does not affect the early deployment behavior (that occurring in the first 0.10 seconds), but by the second rebound (around 0.10 – 0.13 seconds), its effect become apparent. These results show the need of the Rayleigh damping definition to dissipate energy during deployment and to decay the oscillations of the deployed tape spring.

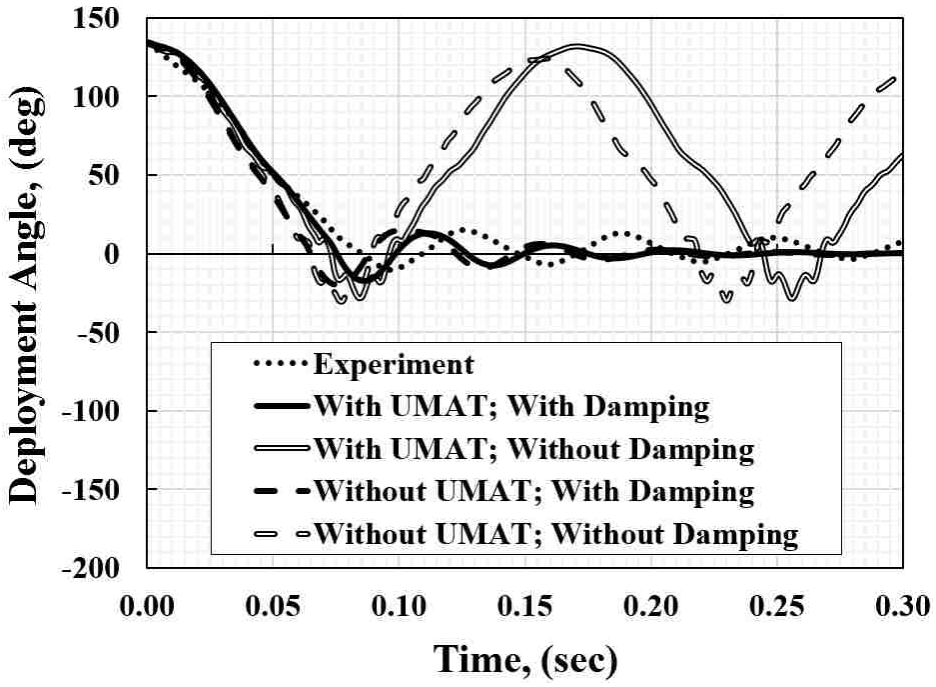

Figure 4.11: A comparison of tape spring deployment behavior after a stowage period of 34 days representing energy dissipation achieved with and without the UMAT subroutine and the Rayleigh damping definition in Abaqus.

4.1.5 SUMMARY OF FINAL MATERIAL PARAMETERS

The remaining properties were referenced from material datasheets and the material library provided by Autodesk Simulation Composite Design for an IM7 carbon fiber and a comparable epoxy resin. The Patz Materials & Technologies PMT-F7 epoxy resin was not included in the material library, and the necessary shear modulus values could not be identified on the available datasheets, so a comparable composite lamina IM7-8552 was considered, as well. For the epoxy itself, the 3501-6 epoxy defined in the Autodesk material library was deemed to be the most comparable option in the database for determining Poisson's ratio of the epoxy. The final material property values as defined in the finite element model are shown in Table 8.

Table 8: Material properties used in finite element model for plain weave and unidirectional composite materials.

Plain Weave		*Source*
Damping α	0.05	Default
Damping β	0	Default
Density (tonne/mm^3)	1.50 E-09	Testing
E_{1f} *(MPa)*	276,000	Hexcel datasheet
E_{2f} *(MPa)*	19,000	Autodesk: IM7
E_{m0} *(MPa)*	2,101	Testing
ν_m	0.34	Autodesk: 3501-6
ν_f	0.2	Autodesk: IM7
V_f	0.53	Testing

Unidirectional		*Source*
Damping α	0.05	Default
Damping β	0.0029	Model calibration
Density (tonne/mm^3)	1.50 E-09	Testing
E_1 *(MPa)*	122,204	Testing
E_2 *(MPa)*	12,220	Standard ratio
ν_{12}	0.27	Testing
G_{12} *(MPa)*	4,753	Autodesk: IM7-8552
G_{13} *(MPa)*	4,753	Autodesk: IM7-8552
G_{23} *(MPa)*	3,898	Autodesk: IM7-8552

4.2 RESULTS OF EXPERIMENTAL TESTING

4.2.1 RESULTS OF EXPERIMENTAL TESTING OF STOWAGE

4.2.1.1 Results of Phase One Experimental Testing of Stowage

The Phase One stowage testing lasted 28 days. During this time, the restoring force, strain, and temperature were recorded. At the beginning of the test, the original temperature data collection device was discovered to be faulty. The batteries were drained every few days, and the data was lost. Therefore, the first ten days of temperature data collection was inconsistent and not included in the results. Once the data collector was replaced with the Supco model, continuous data recording was achieved. The temperature data collection results are shown in Figure 4.12. Temperature fluctuations varied within the range of approximately $22°C$ to $27°C$ throughout the 28-day stowage period. Temperatures were observed to drop each night with the exception of weekends, during which the temperature would rise for two days uninterrupted. The continuous running of the data collection desktop computer in the small testing room may have contributed to some additional heat generation during the stowage period, but this was a consistent variable between all tests. The master curve used to depict the stress relaxation of the tape spring epoxy resin has a reference temperature of $30°C$, and the temperature throughout the stowage testing period remained within reasonable proximity to this temperature.

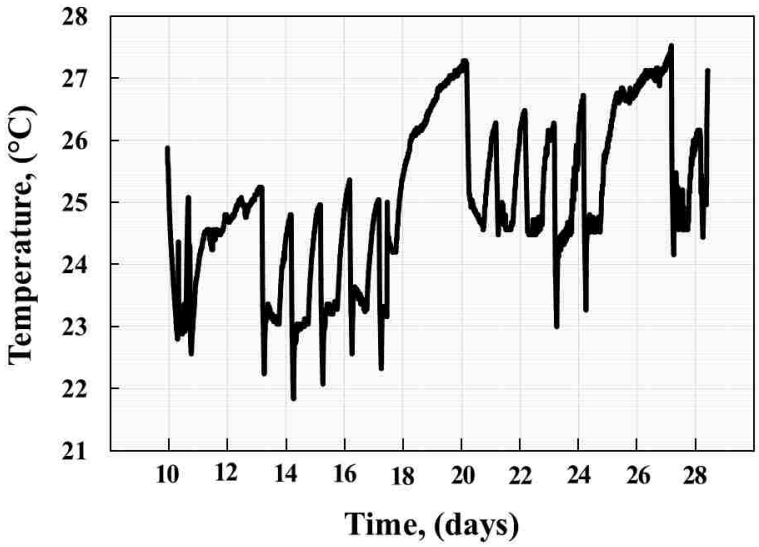

Figure 4.12: Temperature data from Phase One stowage testing.

Axial and transverse strains were measured throughout the 28-day stowage period of the Phase One testing. The intention of the strain gages was not to determine the exact value of strain generated in the tape spring but to track any change in strain over time. Therefore, the strain gages were not calibrated specifically to a CFRP laminate material. Tracking the *change* in strain was of interest, because an ideal stress relaxation experiment consists of a constant applied strain. The strain results are shown in Figure 4.13. The transverse strain remains relatively constant throughout the stowage testing. The axial strain results show a very slight increase over the first week or so of stowage testing. This is assumed to be a due to some settling of the experiment rather than a change in the material. These results show that strain remained considerably constant throughout stowage testing and confirmed the validity of the stress relaxation setup.

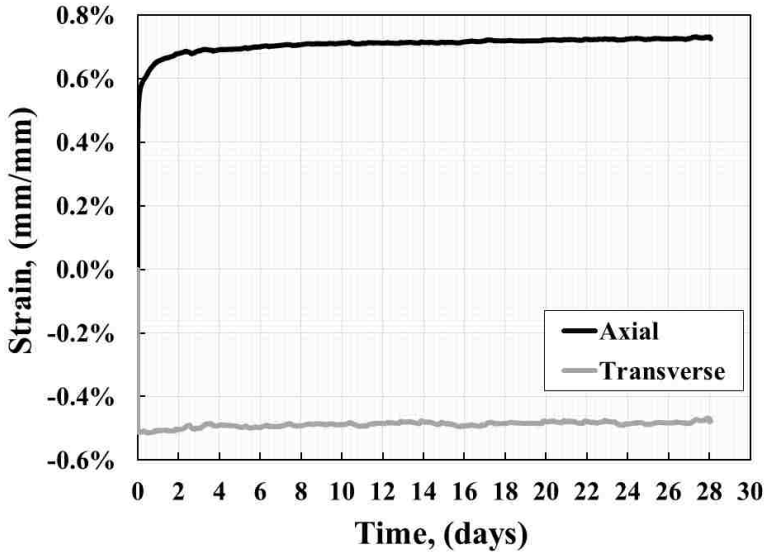

Figure 4.13: Strain results from Phase One stowage testing.

The *restoring force* of interest in this experimental setup was the force with which the folded tape spring pushed against the horizontally aligned load cell in an effort to return to its straight orientation to achieve equilibrium. This force was measured throughout the 28-day stowage period. Due to stress relaxation, the strain energy stored in the tape spring was expected to decrease with time. Therefore, the restoring force of the tape spring was also expected to decrease with time. The results of restoring force in the tape spring throughout the stowage testing are shown in Figure 4.14. Potentially due to temperature fluctuations, vibrations, low restoring force values, and/or the degree of sensitivity present in the load cell, some variation in the restoring force was observed over the 28-day stowage period of Phase One testing. Therefore, a linear trend line was used to represent the average relaxation in the specimen over the stowage testing period.

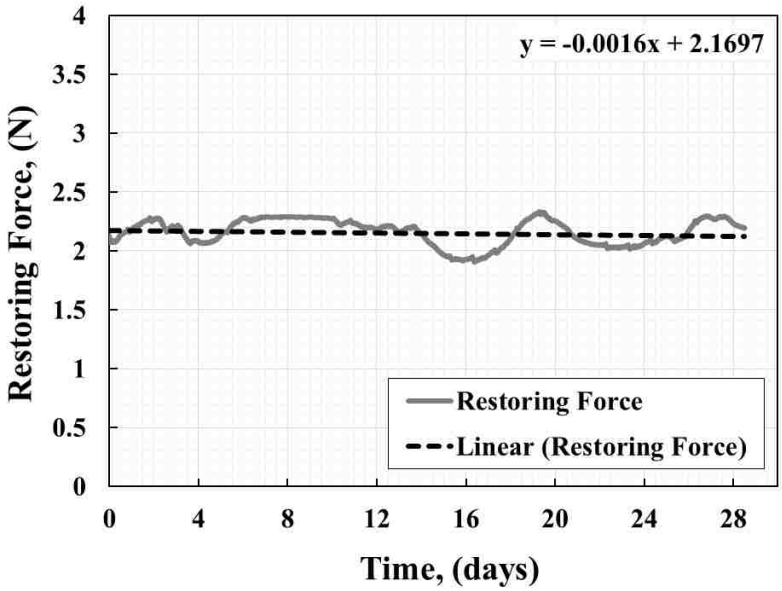

Figure 4.14: Restoring force results from Phase One stowage testing.

By plotting the restoring force and temperature data together for Phase One stowage testing, as shown in Figure 4.15, some insight might be gained regarding the effect of temperature on the rate of relaxation and the noise observed in the restoring force data. Over the weekends when the temperature steadily rose (*i.e.* days 11 – 13, 18 – 20, and 25 – 27), the restoring force decreased at an accelerated rate (*i.e.* the slope was more negative). This appears to be followed by an equilibration in restoring force, or a steady returned to the approximate restoring force value prior to the weekend stowage period. This observation in data seems to be less related to the magnitude of the temperature and more related to the occurrence of a steady rate of change in temperature.

To ensure the accuracy of the load cell, it was loaded with a dead weight and monitored for one day. Although some fluctuation in load readings was observed, it did not exceed 0.018 N (or 0.36% of the dead load value). In contrast, the variation in load readings over the experimental 28-day stowage period exceeded 20% of the original load reading. Therefore, the load variation observed in the long-term stowage experiment was

not due to experimental error. It was likely caused by the sensitivity of the load cell to the experimental environment, including temperature fluctuations and minor external vibrations. The decrease in restoring force from 2.16 N to 2.13 N over the 28-day stowage period is a reduction of 1.4%. This exceeds the precision of the load cell by a factor of four. Therefore, although minor, stress relaxation can be concluded from the long-term stowage experiment.

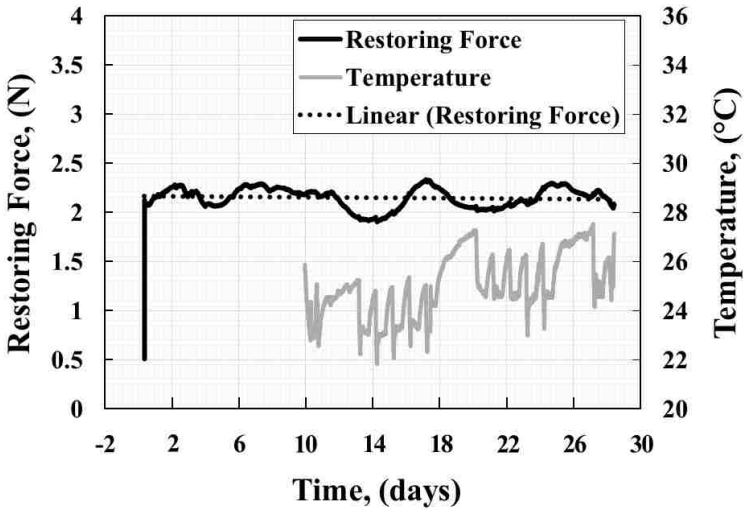

Figure 4.15: Restoring force and temperature data from Phase One stowage testing.

4.2.1.2 Results of Phase Three Experimental Testing of Stowage

Phase Three stowage testing was performed without the use of strain gages following the validation of constant strain in the test setup in Phase One testing. Phase Three stowage testing was carried out six days longer than the Phase One stowage testing for convenience, but the minor amount of stress relaxation observed over the 28-day stowage period of Phase One testing suggested that the difference in stowage period of one week should not have a noticeable effect on the deployment behavior of the tape spring.

The temperature during Phase Three stowage testing was recorded throughout the 34-day stowage period. The results are shown in Figure 4.16. The temperature during the

Phase Three stowage experiment ranged between approximately $23°C$ and $30°C$. As noted earlier, the reference temperature of the master curve used in this study was $30°C$, which was satisfactorily close to the experimental temperature range.

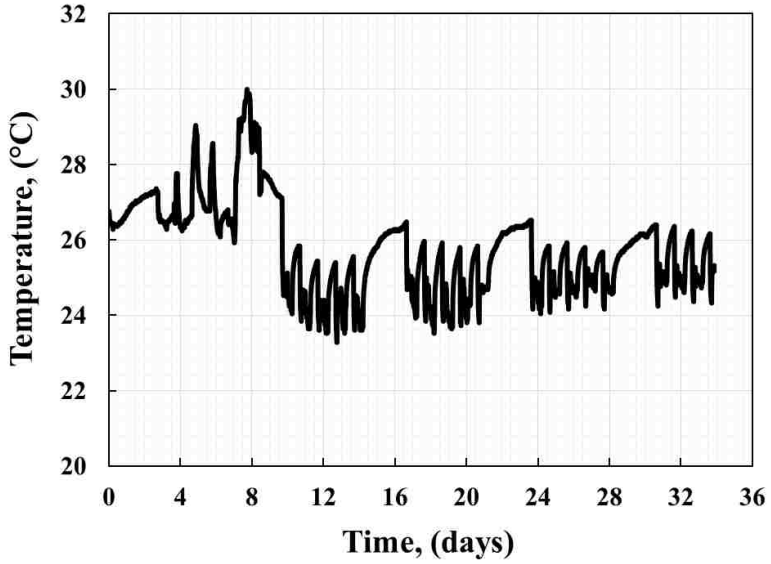

Figure 4.16: Temperature data from Phase Three stowage testing.

The restoring force of the tape spring was recorded over the 34-day stowage period of Phase Three testing. The results are shown in Figure 4.17. Again, due to fluctuations in the restoring force data, a linear trend line was used to represent the average relaxation in the specimen over the stowage period. The negative slope of the linear trend line was small. The Phase Three testing relaxation trend line was slightly steeper than that determined by Phase One stowage testing, which was expected, because the Phase Three stowage period was slightly longer, so the specimen had an additional week during which to relax. The gap in restoring force data collection between the seventh and tenth days was due to a power outage that occurred over one weekend during testing which resulted in a loss of data. This is not expected to affect the overall trend in relaxation behavior observed in the restoring force data. Despite the noise in the restoring force data, a drop in restoring force from 2.06

N to 1.98 N represents a reduction of 4%. This exceeds the precision of the load cell by a factor of 11. Therefore, stress relaxation can be concluded.

The long-term stowage experiment was performed to measure the stress relaxation that occurs in a tape spring stowed at ambient temperature for 34 days, because it was expected that the degree of stress relaxation observed would inform the degree of change observed in the deployment behavior of the tape spring following stowage. It was important to know whether the stress relaxation resulting from the experimental stowage conditions was representative of that resulting from realistic aerospace stowage applications. The results showed that during a 34-day stowage at ambient temperatures the tape spring had a very minor stress relaxation response. Therefore, longer experimental stowage periods, or the simulation of longer stowage periods achieved through increased stowage temperature, is recommended.

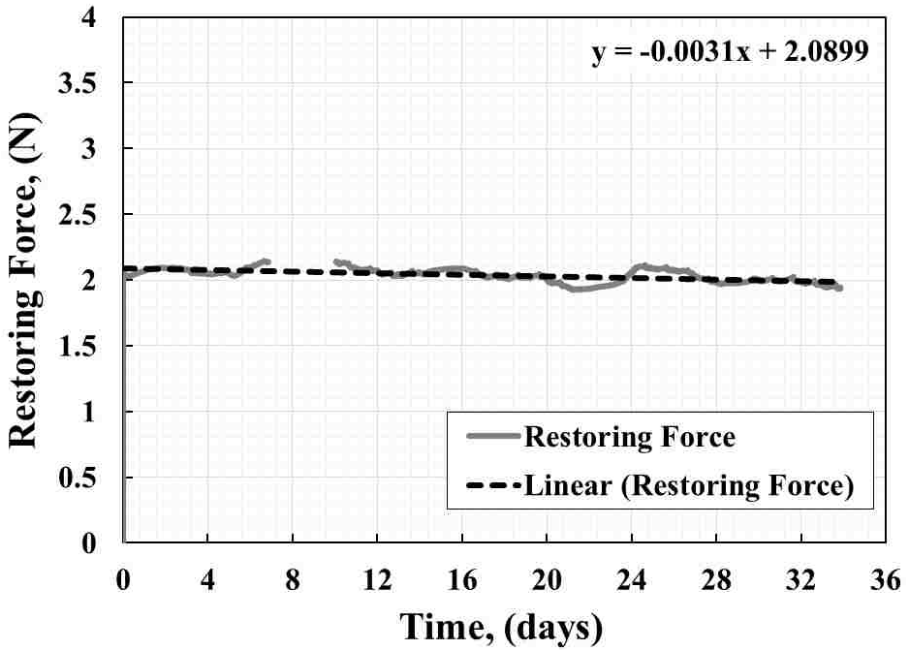

Figure 4.17: Restoring force results from Phase Three stowage testing.

By plotting the temperature and restoring force data together for Phase Three stowage testing, as shown in Figure 4.18, some correlation between temperature and restoring force may be examined. During Phase Three stowage testing, the increase in temperature over weekends did not result in a noticeable drop in restoring force as it did during Phase One stowage testing. In fact, between days 22 – 24, the restoring force was actually observed increasing. Therefore, no conclusion can be drawn from these findings alone on the immediate effect of temperature fluctuation on tape spring relaxation.

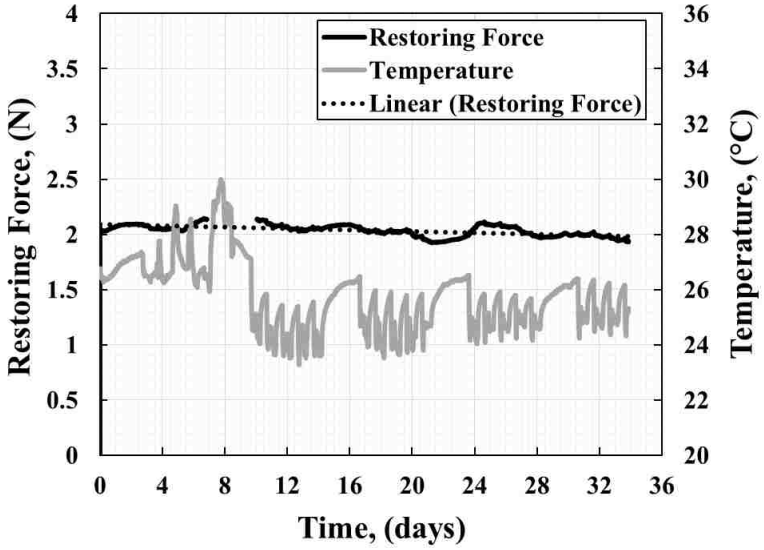

Figure 4.18: Temperature and restoring force data from Phase Three stowage testing.

4.2.2 RESULTS OF EXPERIMENTAL TESTING OF DEPLOYMENT

4.2.2.1 Results of Phase One Experiment Testing of Deployment

The results of Phase One deployment testing show the angular position of the tape spring in terms of degrees where zero degrees represents a completely vertical tape spring. The experimental deployment results for Phase One testing are shown in Figure 4.19. First, the deployable end of the specimen was rotated 190° to achieve the folded configuration. It can be observed in the Phase One deployment testing results that the specimen never

returned to zero degrees. Following initial deployment, the tape spring specimen stalled around 60°. It is believed that this was due to the attachment of strain gages to the tape spring surface. The two strain gages that were attached to the tape spring each required a bridge with six wires soldered onto them. Although the wires were cut close to the tape spring surface prior to deployment, the combined mass of the remaining wire edges, solder, and superglue used to secure the strain gages and bridges likely weighed down the tape spring. Although this is understandable considering that the thickness of the tape spring laminate itself was only 0.48 mm, this test sheds light on the extreme caution that must be used with tape springs, because small errors can result in incomplete deployment. The attachment of strain gages presented a flaw in the Phase One *deployment* test, but the Phase One *stowage* test findings remain insightful. It was valuable to perform the first stowage test with strain gages to ensure that strain remained constant throughout stowage. In the following images of tape spring deployment, the tape spring outline has been darkened for improved visibility. The deployment angles were read from the radial chart manually and were limited to a precision resolution of one degree.

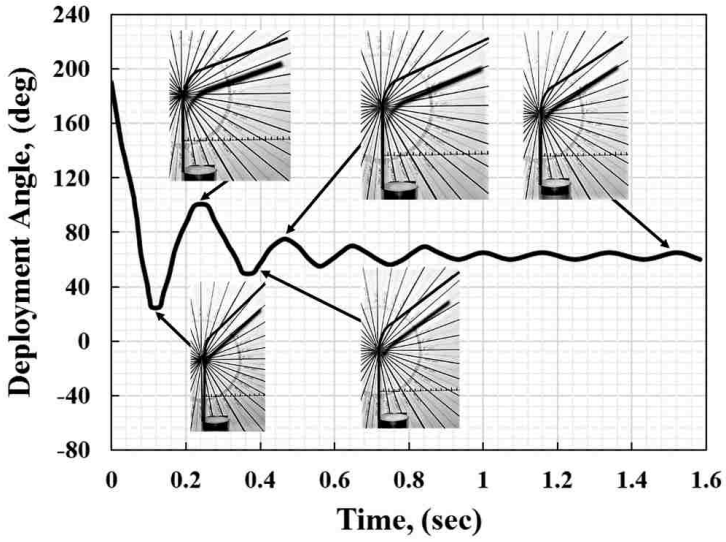

Figure 4.19: Results from Phase One deployment testing.

Perhaps an even more significant variable in the Phase One deployment testing anomaly was the stiffness of the superglued strain gages. When folded, the cross-sectional curvature of a tape spring becomes flat in the folded region. The transverse strain gage was secured precisely at this location and spanned the flattened cross-section for the duration of the 28-day stowage period. Consequently, when the tape spring deployed, it is suspected that the stiffness of the superglued transverse strain gage prevented the cross-section of the tape spring from snapping back into its natural curvature, and thus, prevented the tape spring from returning to its vertical orientation with ease. For this reason, deployment testing was repeated without strain gages in Phase Two and Phase Three deployment testing. Figure 4.20(a) shows that the folded region was unable to return to its straight configuration during initial deployment. This occurred at the exact region where the strain gages were attached. Figure 4.20(b) shows that some axial curvature still remained in the deployed tape spring even 48 hours after initial deployment.

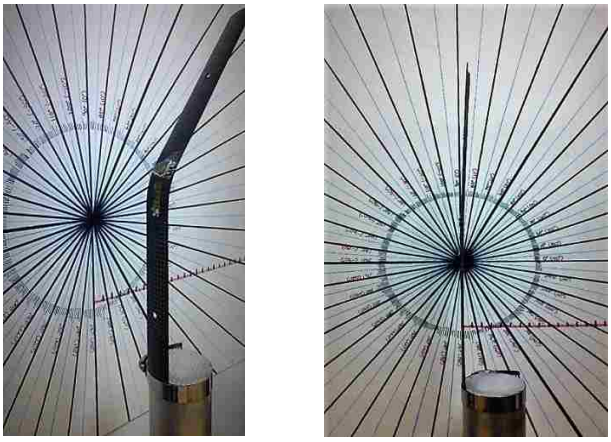

(a) (b)

Figure 4.20: Stalled tape spring during Phase One deployment testing. (a) At its initial stalled angle of 60°, the tape spring was unable to overcome the stiffness at the folded region resulting from strain gage attachment. (b) The remaining axial curvature in the tape spring specimen 48 hours after deployment.

The long-term recovery of the tape spring, shown in Figure 4.21, was recorded for two days following the initial deployment test. Long-term recovery happened steadily over the first 29 hours or so following initial deployment. Then upon achieving the deployment angle of 25°, the tape spring was able to quickly recover most of the remaining displacement distant and return to a slightly-shy-of-vertical position of 3°.

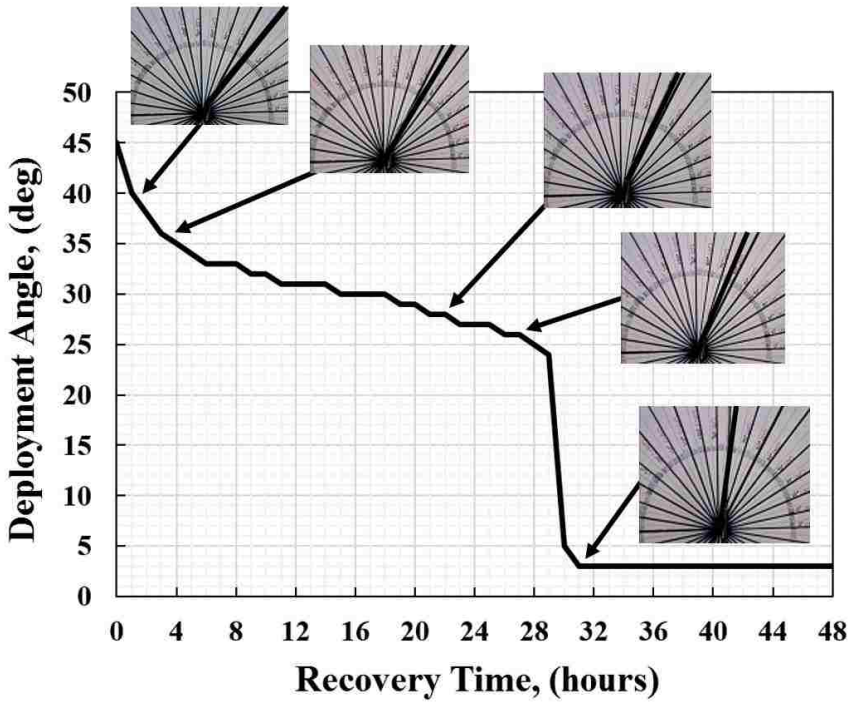

Figure 4.21: Long-term viscoelastic recovery of the tape spring specimen in Phase One deployment testing.

4.2.2.2 Results of Phase Two Experimental Testing of Deployment

Phase Two deployment testing was performed without a preceding stowage period. The results of the Phase Two deployment testing are shown in Figure 4.22. The initial fold angle was equal to that in Phase One testing at 190°. The tape spring first passed the vertical position at 0.11 seconds, and the initial overshoot was 20°.

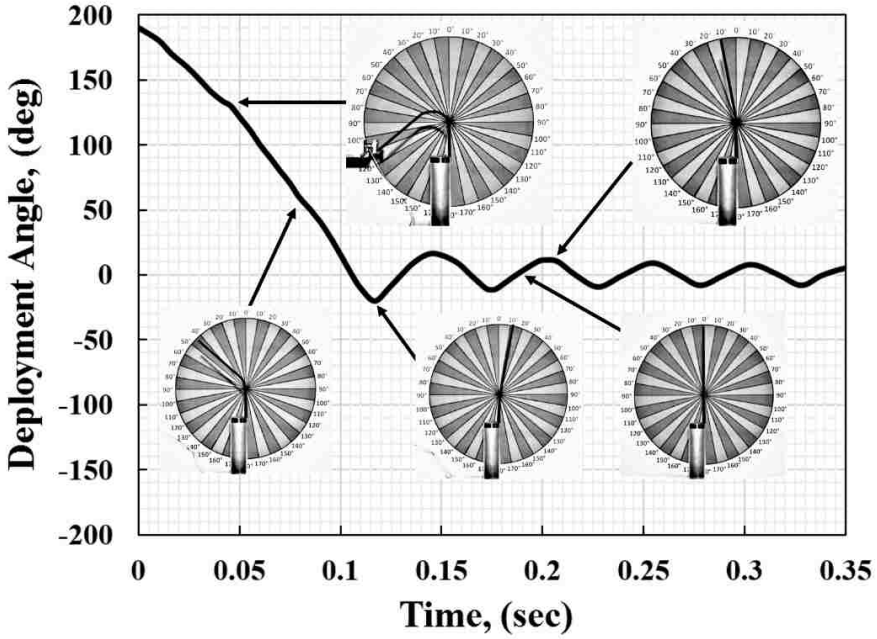

Figure 4.22: Results from Phase Two deployment testing.

4.2.2.3 Results of Phase Three Experimental Testing of Deployment

The results of Phase Three deployment testing are shown in Figure 4.23. Phase Three deployment did not display any premature stalling, likely due to the lack of strain gages used in this procedure. The initial folded angle was 190°. The deployed tape spring first passed the vertical position at 0.13 seconds. More overshoot was observed on the concave side of the tape spring (*i.e.* the positive angles) wherein the tape spring achieved equal sense bending, because the overshoot movement was limited in the opposite direction by having to overcome the cross-sectional curvature of the tape spring. Due to filming limitations and file size limitations, the deployment recordings were terminated before all tape spring oscillations were completely damped. The initial deployment behavior was of most interest in this study, because that is where any stalling behavior and the degree of initial overshoot are observed. A stalled deployment and an overly chaotic deployment are two extremes that need to be predicted, anticipated, or avoided to achieve safe and reliable

deployment of spacecraft components. Therefore, the long-term damping of the tape spring oscillations was not examined in this study.

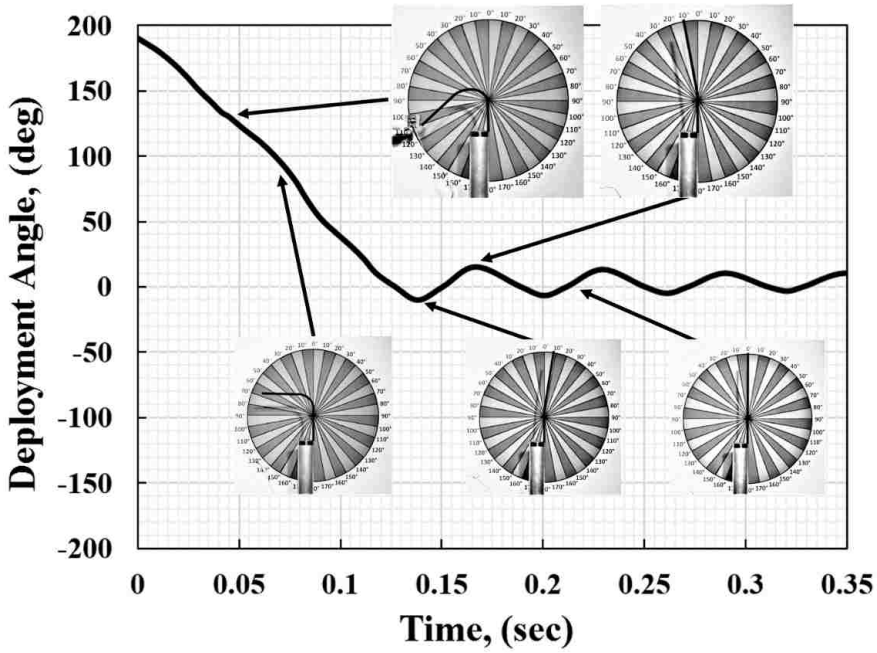

Figure 4.23: Results from Phase Three deployment testing.

The tape spring in the Phase Three stowage testing was folded in equal sense bending to the left of 0° against the radial chart, unlike in the Phase One testing where it was folded in equal sense bending to the right of 0° due to the TSSD fixture being rotated 180°. Despite the lack of deployment stalling in the Phase Three deployment testing, there was still a slight degree of noticeable long-term recovery in the tape spring specimen, as shown in Figure 4.24. Following its initial deployment, the tape spring stabilized at an angle of 2°. Over the next three hours, the tape spring achieved a deployment angle of 1°. Although the long-term recovery was tracked for a total of seven days, as shown in Figure 4.25, no additional recovery was observed.

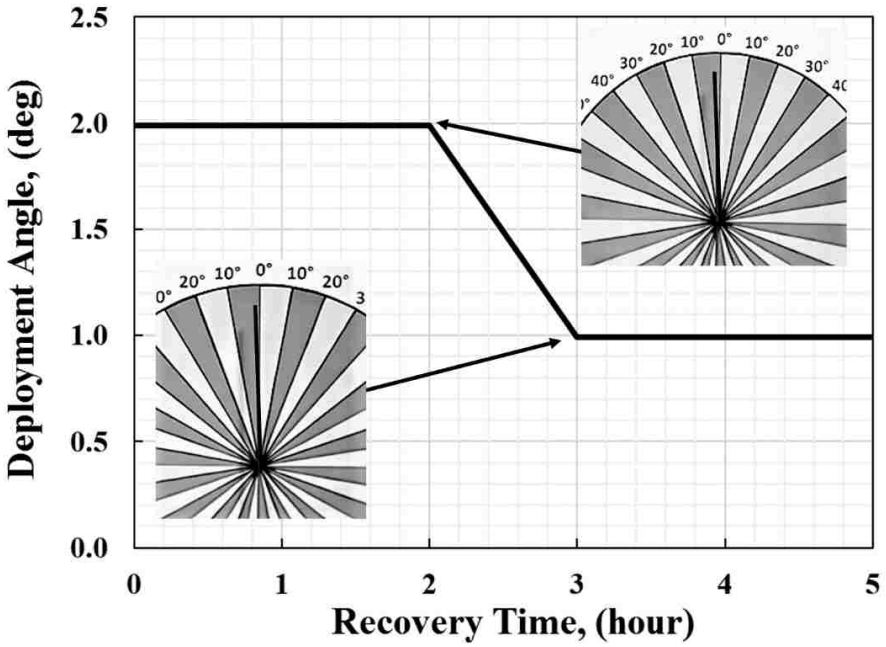

Figure 4.24: Long-term viscoelastic recovery in Phase Three deployment testing over five hours.

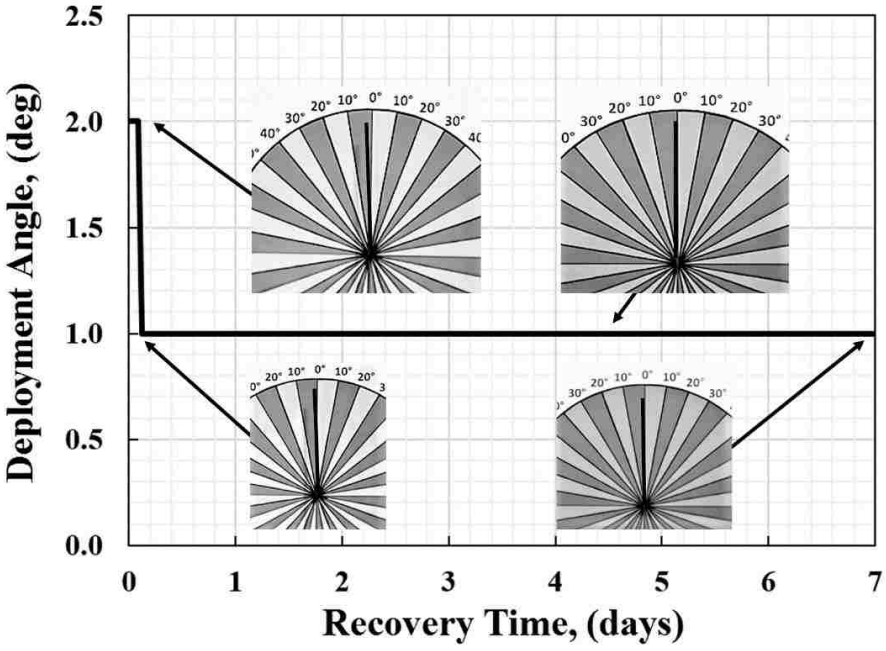

Figure 4.25: Long-term viscoelastic recovery in Phase Three deployment testing over seven days.

A comparison of the observed deployment behavior between the Phase Two deployment testing and Phase Three deployment testing is shown in Figure 4.26. The Phase Three specimen initially deployed more slowly (over 0.13 seconds compared to 0.11 seconds) and displayed less overshoot (-10° compared to -20°). These changes were the result of stowage effects on the Phase Three tape spring specimen.

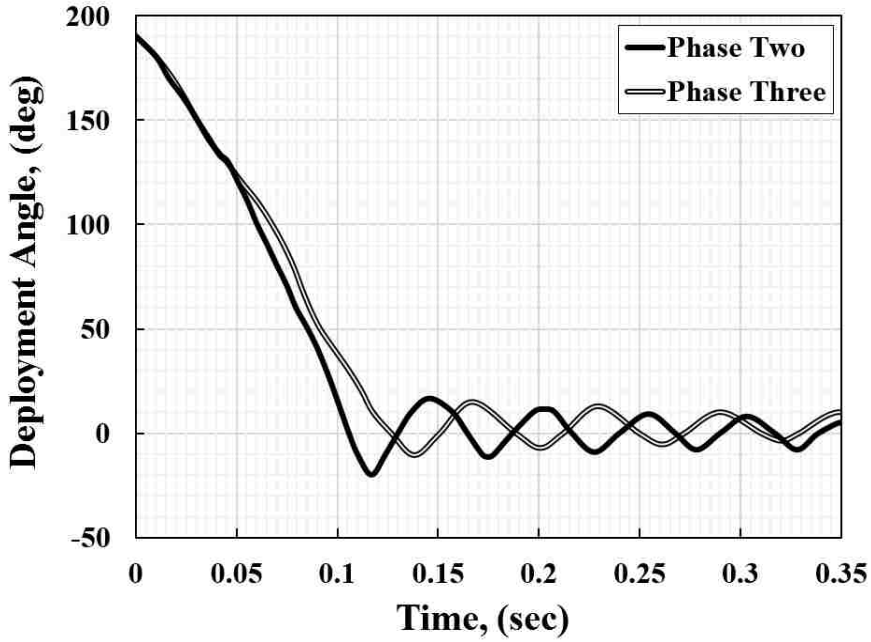

Figure 4.26: Results from Phase Two and Phase Three deployment testing.

4.3 RESULTS OF NUMERICAL SIMULATIONS

4.3.1 VALIDATION OF MODEL

4.3.1.1 Static Deflection Validation

To validate the tape spring model, the reaction force caused by a deflection of 40 mm was measured. The tape spring specimen was identical to those used in the stowage and deployment experiments. One end of the tape spring was clamped to the aluminum cylinder in the TSSD setup. The other end was deflected 40 mm manually. Reaction force

measurements were collected with a load cell for the duration of the deflection, as shown in Figure 4.27.

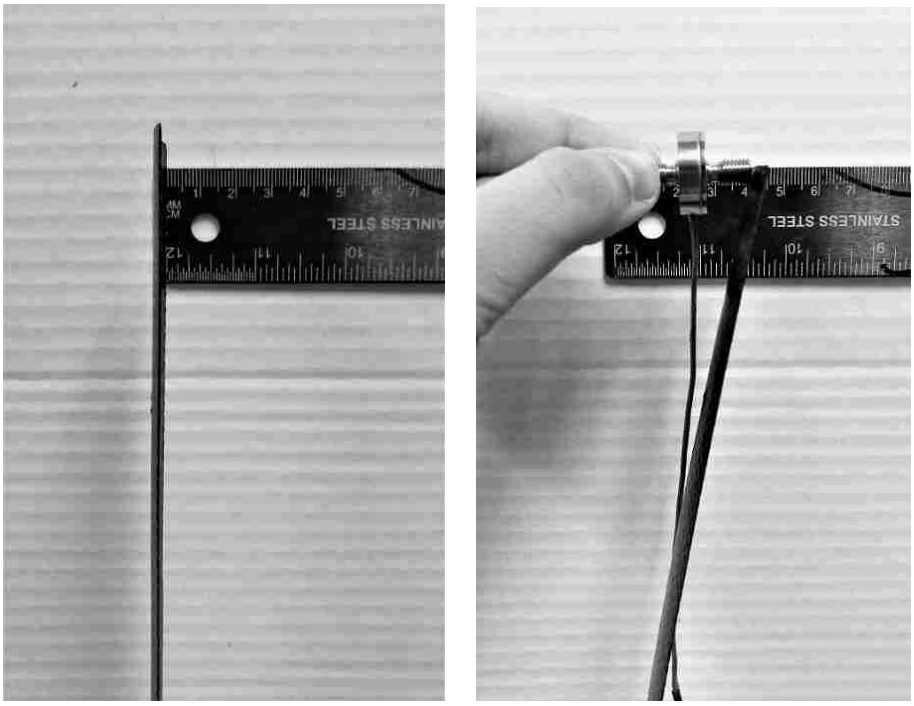

(a) (b)

Figure 4.27: (a) The tape spring in its original (fixed) configuration, and (b) the tape spring deflected 40 mm to the right with a compression load cell.

A comparison between the measured and simulated results is shown in Figure 4.28. The measured reaction force after a deflection of 40 mm was 0.63 N. The finite element model that had been developed for the stowage and deployment simulations was used to simulate the deflection measurements by displacing Node A 40 mm in the negative z-direction. The resultant reaction force in the simulation was 0.62 N. These results were in close agreement with the measured value and served to validate the model.

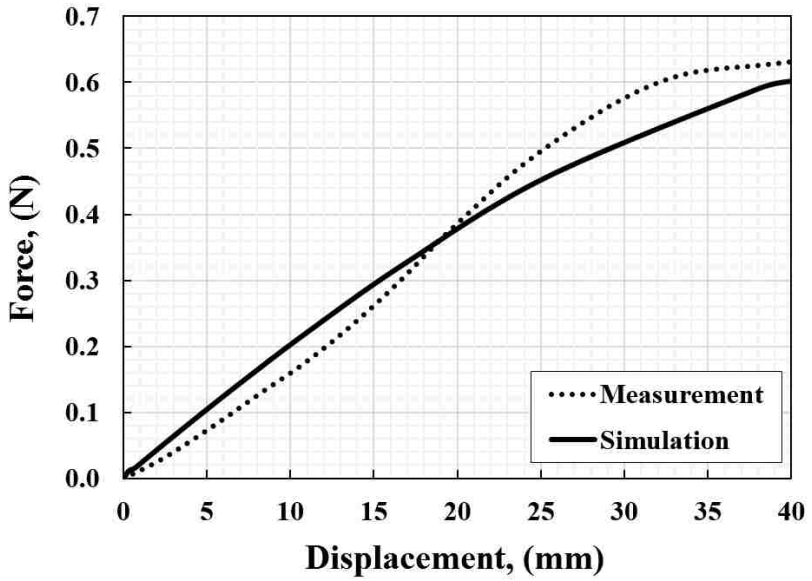

Figure 4.28: Measured and simulated results from the tape spring deflection.

4.3.1.2 Folding Validation

The folding sequence used to arrange the tape spring into its stowage configuration was performed by pushing the tape spring with a load cell at the location of the tape spring hole experimentally and at Node B_1 in the simulation. The reaction force measurements were collected by displacing the tape spring roughly 30 mm in the negative z-direction over 1.2 seconds, 150 mm in the negative x-direction over 0.2 seconds, and 68 mm in the negative z-direction over 1.6 seconds, and then adjusting it to the correct height just below its own clamped end by moving it 68 mm in the negative x-direction over 0.6 seconds. The folding sequence was done manually, as shown in Figure 4.29, and provided a rough estimate of the folding response of the tape spring. Most of interest was the final reaction force in the stowage configuration which was measured to be 2.58 N.

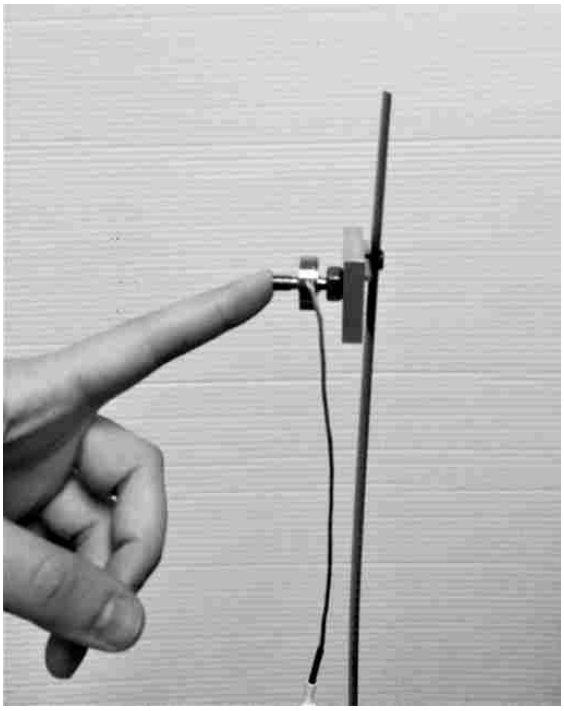

Figure 4.29: Setup for folding measurement.

The measurement of the reaction force during folding was compared to the results of the simulation, as shown in Figure 4.30. The simulation results were smoothed for comparison due to the occasional jump in the reaction force occurring at the start of a new analysis step. The overall shape of the folding reaction force curves were similar. Most importantly, the reaction force of the tape spring in the final folded stowage configuration was 2.24 N in the simulation, which was in close agreement with the measured value of 2.58 N. In the Phase Two stowage simulation, the measured initial reaction force value was 2.13 N, and in the Phase Three stowage simulation it was 2.07 N, which were both in close agreement with the simulation value of 2.24 N.

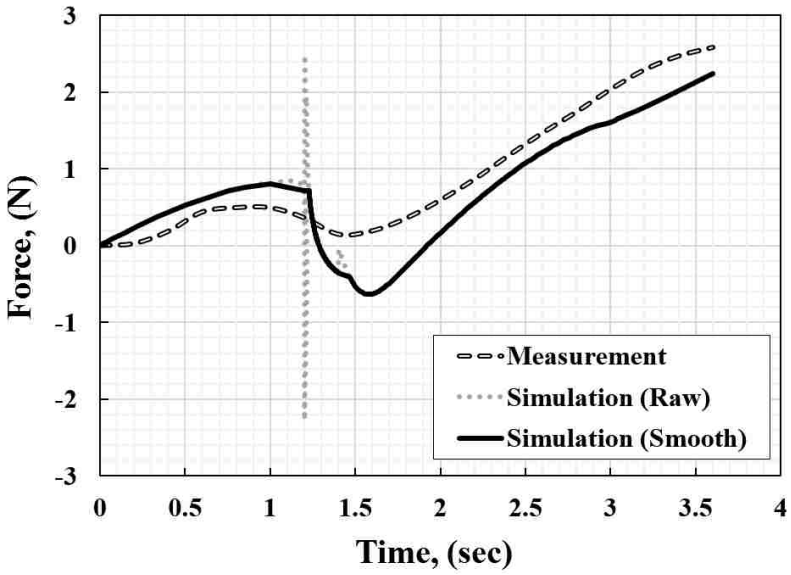

Figure 4.30: Measurement and simulation results from tape spring folding.

4.3.2 RESULTS OF NUMERICAL SIMULATION OF STOWAGE

4.3.2.1 Results of Phase One Numerical Simulation of Stowage

Phase One stowage testing was simulated in Abaqus/CAE by assigning the stowage step a run time of 28 days. The stowage geometry of the tape spring model matched that of the experiment, as shown in Figure 4.31.

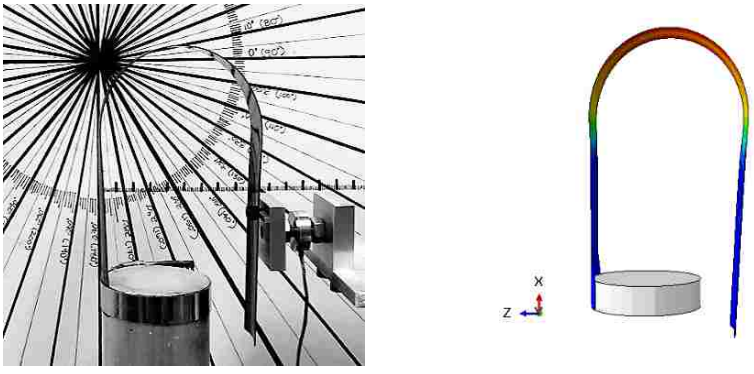

(a) (b)

Figure 4.31: Geometry of Phase One (a) stowage experiment and (b) finite element simulation in Abaqus.

In the simulation, Nodes B_1 and B_2 were defined as the locations of the tape spring in contact with the load cell plate and screw in the experiment. The restoring forces at these two nodes were reported and summed together to determine the restoring force during stowage from the simulation. The results are shown in Figure 4.32. While the overall restoring force of the simulation was slightly higher than that measured experimentally, the slopes of both lines are considerably parallel. Therefore, the relaxation calculated by the UMAT subroutine ran with Abaqus reasonably matched that measured experimentally. The slight differences in magnitude of the restoring force could be due in part to a minor miscalibration of the load cell or the mass of the aluminum plate and screws that were attached to the load cell after calibration and were not accounted for in the simulation.

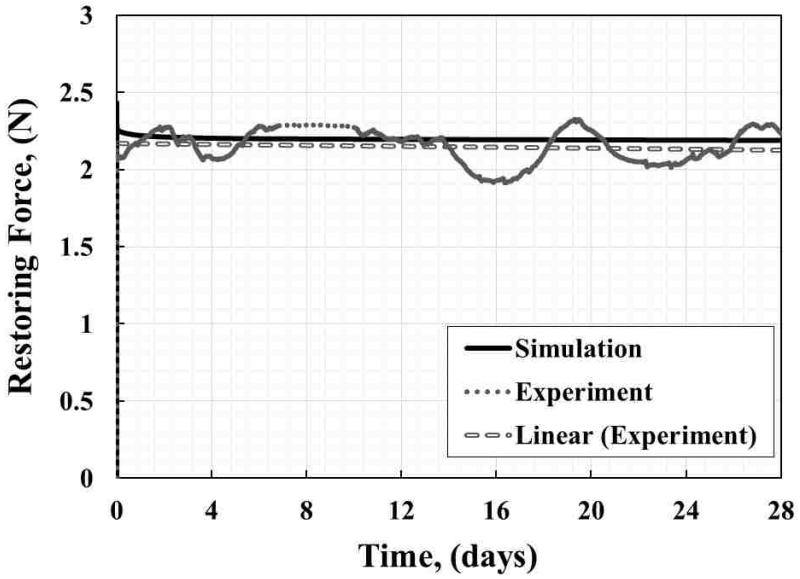

Figure 4.32: Restoring force results from the experiment and simulation for Phase One stowage testing.

The strain in the stowed tape spring was calculated at each time step using the UMAT subroutine. The axial and transverse strain results in the simulation are shown compared to those obtained experimentally in Figure 4.33. Since the strain gages had not

been calibrated prior to the stowage experiment and were used only to track changes in strain, a multiplier was applied to the experimental data to orient the experimental strain data close to that of the simulation on the plot. The simulation results confirm that strain should remain constant throughout stowage. The simulation results are similar to what was observed in the transverse strain experimentally. The axial strain measured experimentally displayed a slight increase at the beginning of the stowage experiment. It is believed that this was the result of settling in the experiment rather than a change in the material.

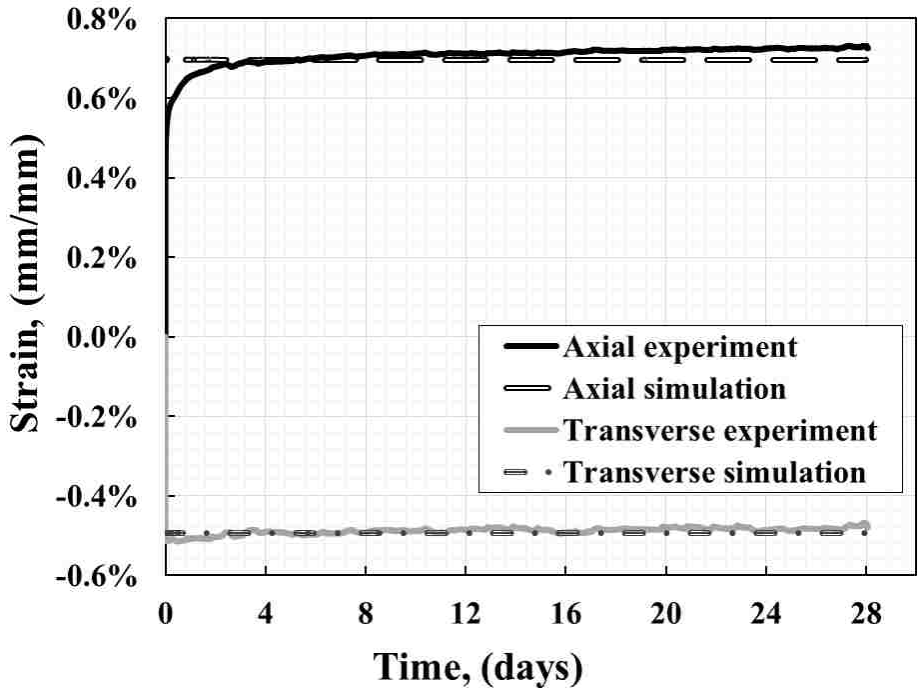

Figure 4.33: Strain results from the experiment and finite element simulation in Abaqus.

Although experimentally the strain was measured at the mid-length of the tape spring (along the folded region), the variation of shear strain in the tape spring specimen can be observed using the finite element simulation in Abaqus, shown in Figure 4.34. For example, peak shear strains can be found at the locations of changes in transverse curvature in the tape spring. These locations were not monitored for strain experimentally.

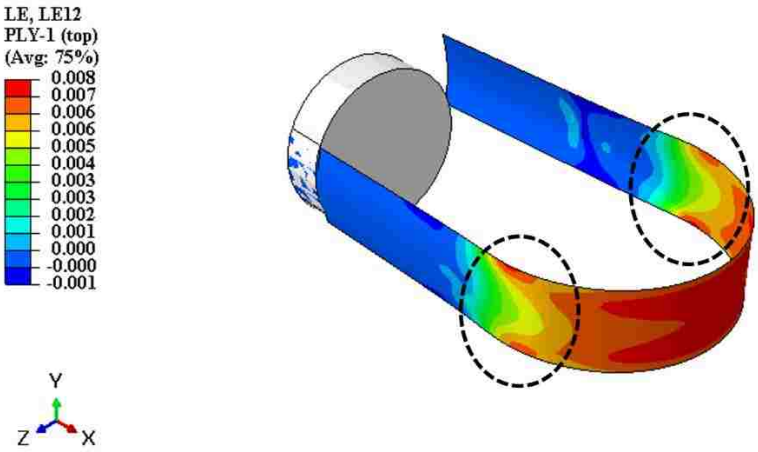

Figure 4.34: Shear strain distribution at locations of transverse curvature change in the stowage configuration in the finite element simulation using Abaqus.

4.3.2.2 Results of Phase Three Numerical Simulation of Stowage

Phase Three stowage testing was modeled identically to that of the Phase One stowage testing except that the stowage step was set to 34 days instead of 28. The folded tape spring geometry of the model matched that of the experiment, as shown in Figure 4.35.

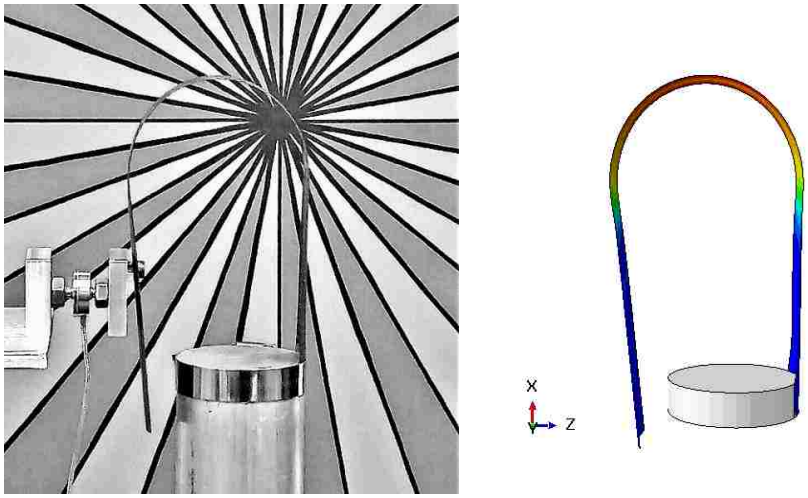

(a) (b)

Figure 4.35: Geometry of Phase Three stowage (a) experiment and (b) finite element simulation in Abaqus.

The restoring force of the simulation at Nodes B_1 and B_2 was compared to that measured experimentally during the 34-day stowage period. The results are shown in Figure 4.36. The overall magnitude of the restoring force was slightly different between the experiment and simulation, but the slopes of the two lines are similar. Therefore, the amount of relaxation predicted by the model was in close agreement to that measured experimentally. The differences in magnitude of the measured and simulated restoring force could be due in part to a slight miscalibration of the load cell or the mass of the aluminum plate and screw which were attached to the load cell after calibration and were not accounted for in the model.

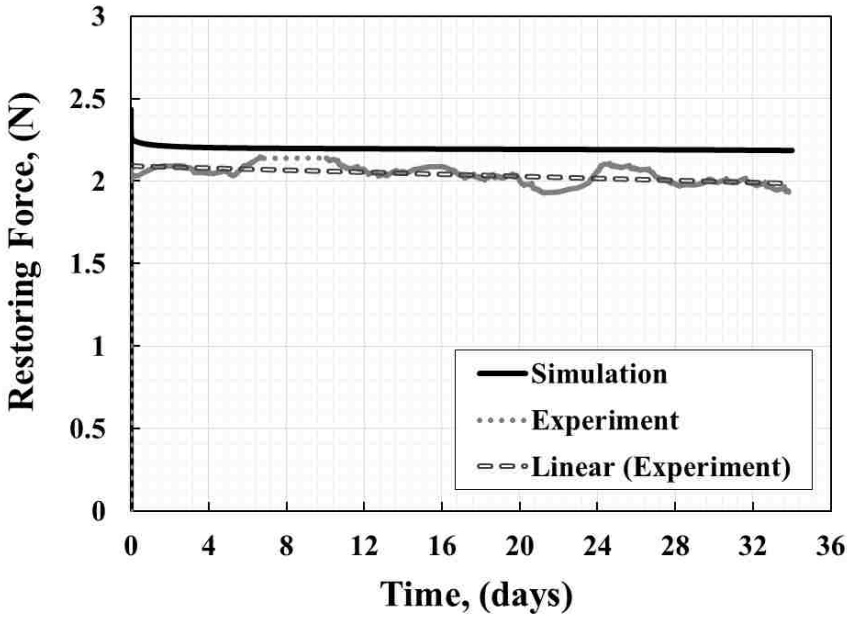

Figure 4.36: Restoring force results from the experiment and simulation of Phase Three stowage testing.

A comparison between the restoring force results from the Phase One and Phase Three stowage testing for both the experiment and simulation is shown in Figure 4.37. The restoring force determined by the simulation for Phases One and Three testing was identical

except that the data for Phase Three was collected for an additional six days. The slopes in all four cases match reasonably well, indicating that the relaxation behavior was simulated as intended.

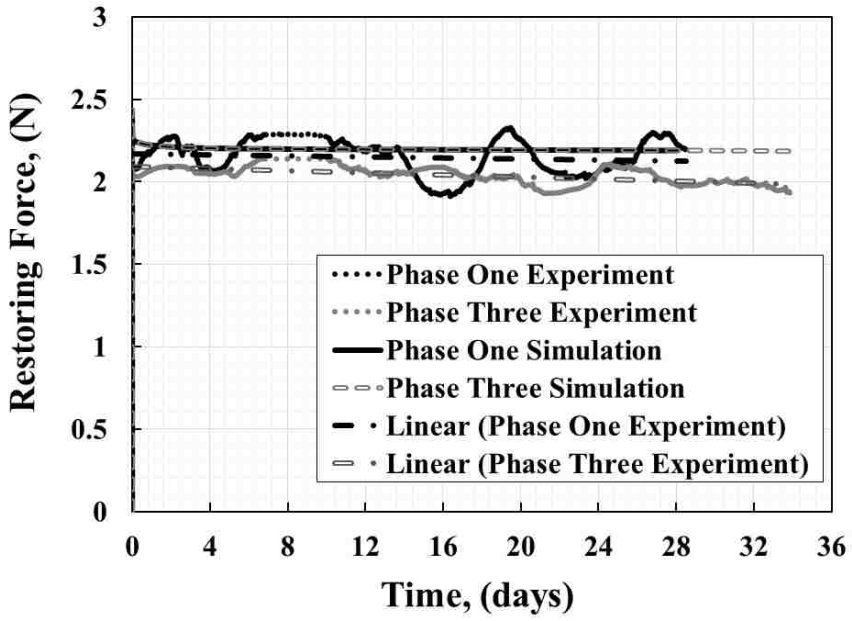

Figure 4.37: Restoring force results from the experiment and simulation of Phase One and Phase Three stowage testing.

4.3.3 RESULTS OF NUMERICAL SIMULATION OF DEPLOYMENT

4.3.3.1 Results of Phase Two Numerical Simulation of Deployment

Phase One deployment testing was not modeled due to the deployment anomaly caused by the use of strain gages. Phase Two deployment testing was simulated by suppressing the stowage step to simulate the lack of stowage in the Phase Two experimental deployment testing. To avoid any slowing down of the deployment caused by the speed of the moving load cell boundary condition, experimental and numerical simulation of deployment was compared starting at the moment the tape spring cleared the load cell boundary condition.

Therefore, the time axis was shifted in the following results such that the moment at which the tape spring cleared the load cell boundary condition was set to time zero. The Phase Two deployment testing results from the experiment and simulation are shown in Figure 4.38. The simulation results through the second oscillation matched the experimental results with good accuracy. Beyond that, the artificial damping in the simulation caused an early damping response in the tape spring. A comparison of Phase Two tape spring deployment geometry between the experiment and simulation is shown in Figures 4.39.

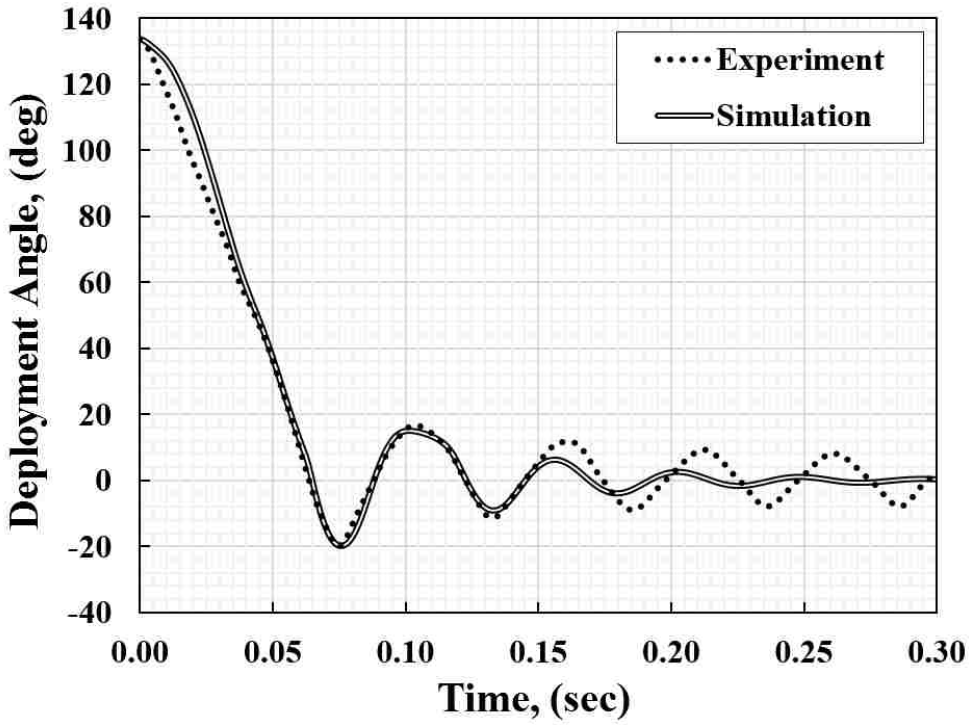

Figure 4.38: Results from the experiment and simulation of Phase Two deployment testing.

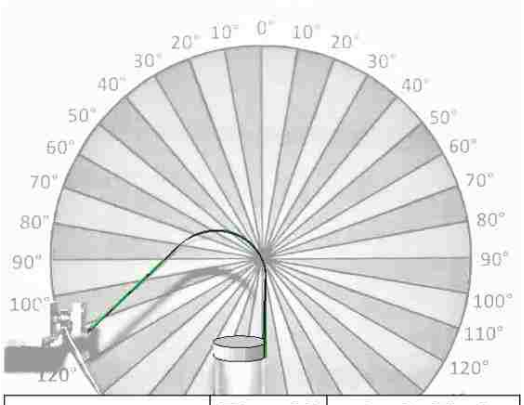

	Time [s]	Angle [deg]
Experiment	0	135
Simulation	0	134

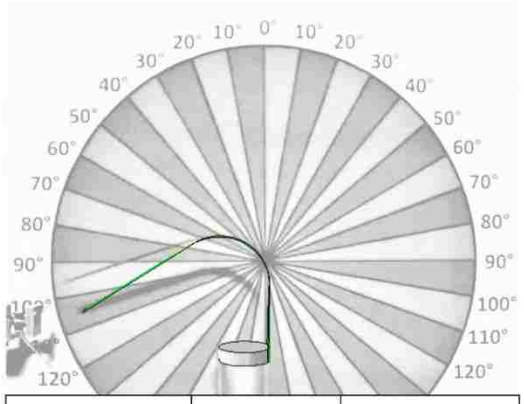

	Time [s]	Angle [deg]
Experiment	0.01375	110
Simulation	0.01377	130

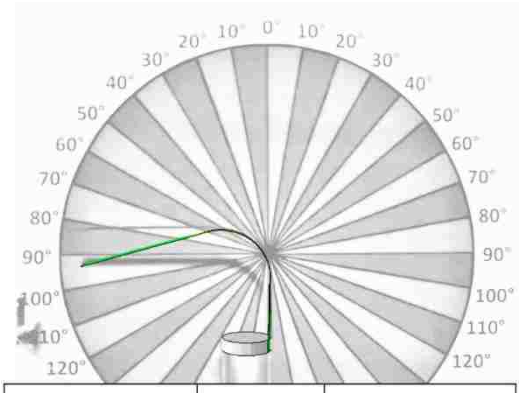

	Time [s]	Angle [deg]
Experiment	0.02188	90
Simulation	0.02184	105

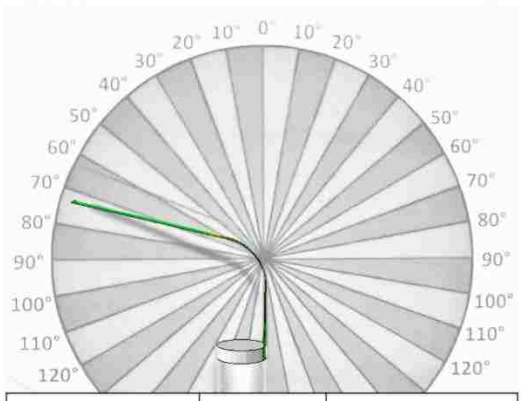

	Time [s]	Angle [deg]
Experiment	0.03125	70
Simulation	0.03261	74

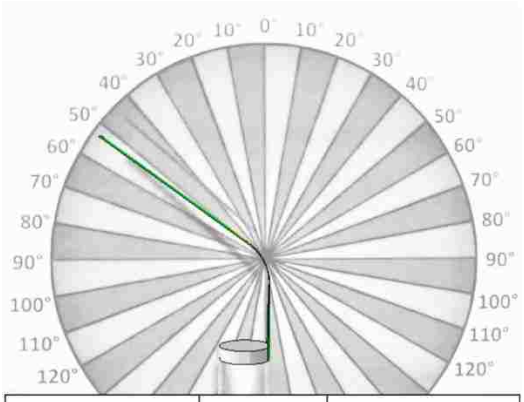

	Time [s]	Angle [deg]
Experiment	0.04250	45
Simulation	0.04244	50

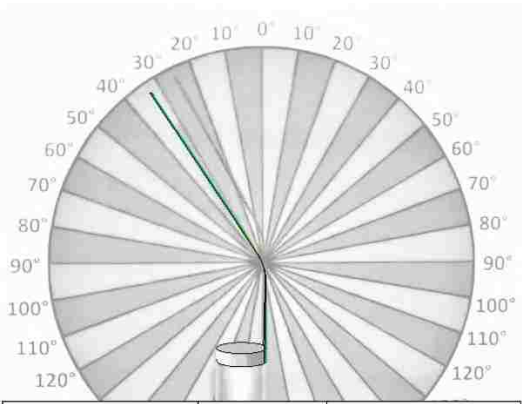

	Time [s]	Angle [deg]
Experiment	0.051875	30
Simulation	0.051610	34

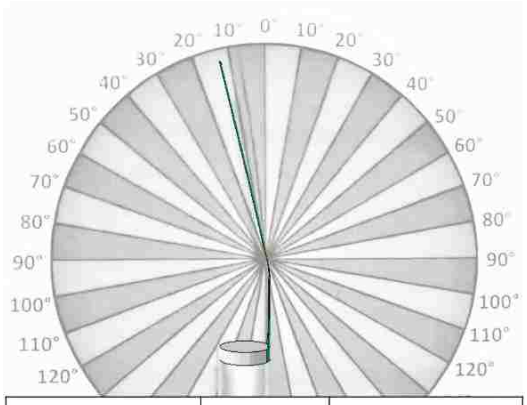

	Time [s]	Angle [deg]
Experiment	0.059374	10
Simulation	0.059782	13

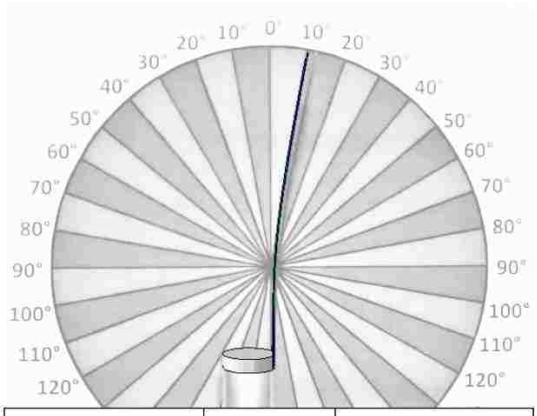

	Time [s]	Angle [deg]
Experiment	0.06813	-10
Simulation	0.06892	-11

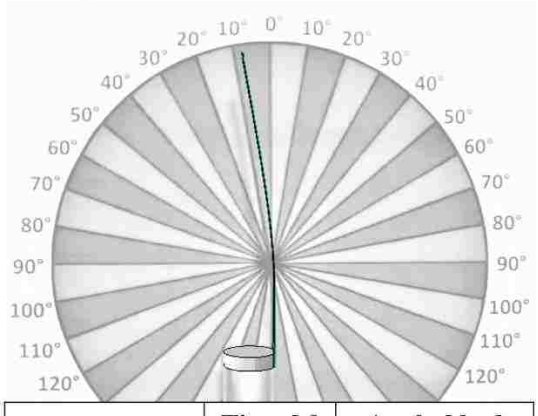

	Time [s]	Angle [deg]
Experiment	0.09438	10
Simulation	0.09436	10

.

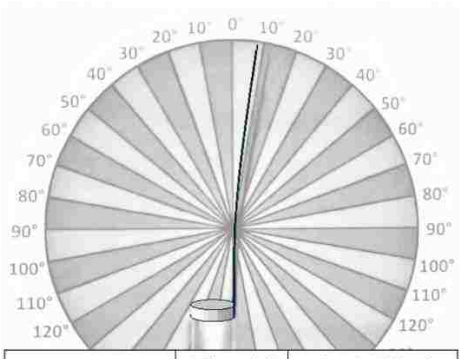

	Time [s]	Angle [deg]
Experiment	0.1300	-10
Simulation	0.1311	-9

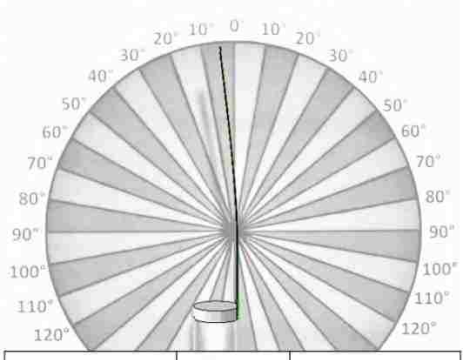

	Time [s]	Angle [deg]
Experiment	0.1550	10
Simulation	0.1552	7

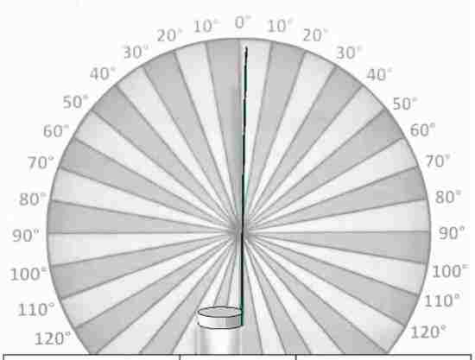

	Time [s]	Angle [deg]
Experiment	0.1731	-2
Simulation	0.1743	-1

Figure 4.39: An overlay comparison of deployment geometry between Phase Two experiment and simulation in Abaqus.

4.3.3.2 Results of Phase Three Numerical Simulation of Deployment

Phase Three deployment testing was simulated by setting the stowage step to 34 days and tracking the deployment of Node A as described in Section 3.2.1.3. The simulation results for Phase Three deployment testing are shown in Figure 4.40. It can be observed that the initial rate of deployment is in close agreement for the experiment and model. The model predicts initial deployment happening slightly faster than that measured experimentally (over 0.088 seconds compared to 0.095 seconds) and with slightly more overshoot (-17° compared to -10°). The artificial damping defined in the simulation caused the oscillations to damp out sooner than they did in the experiment.

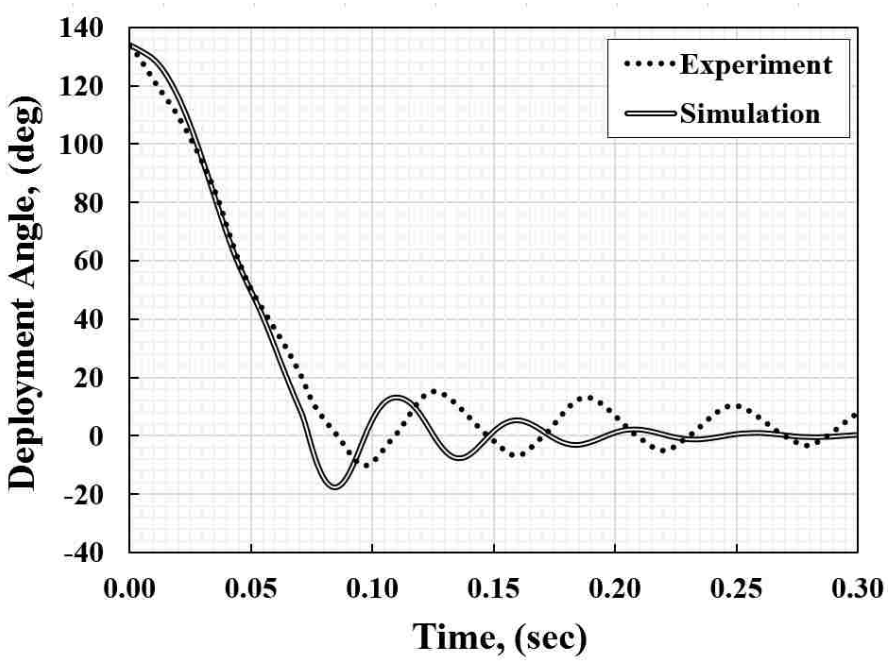

Figure 4.40: Results from experiment and simulation of Phase Three deployment testing.

The damping used was Rayleigh viscous damping at the material level, which is commonly used to define energy dissipation in direct steady state dynamic analysis. The other damping options available in Abaqus, *composite* and *structural*, could not be used for this application. The energy dissipation during deployment is due in large part to the

rapid deformation experienced by the tape spring as the fold region travels slightly up the length of the tape spring. Additional energy dissipation occurs during the snapback or overshoot of the tape spring which causes the transverse curvature of the tape spring to flatten or become inverted. Rayleigh damping depends on mass and stiffness at lower and higher frequencies, respectively. However, this is not an exact representation of the damping observed experimentally. The tape spring vibrational frequency during deployment oscillation begins low and then becomes high as the tape spring approaches stability in its straight configuration. By applying Rayleigh damping, it implies that the mass (which is quite low) has a stronger effect on damping early in the deployment analysis, and the stiffness (which is quite high) has a stronger effect on damping later in the deployment analysis. However, in reality, it is the stiffness of the tape spring that supports energy dissipation early in the deployment sequence, as it resists rapid material deformation. This effect is not entirely captured by the use of Rayleigh damping coefficients.

Furthermore, one of the challenges with the Rayleigh damping definition in Abaqus is that it allows for the assignment of a single alpha value and a single beta value per material. This assumes material isotropy. In the case of the FlexLam composite tape spring, each material is orthotropic, so its damping is not necessarily uniform in every direction. Although it was beyond the scope of this work, one potential solution to better address this limitation could be the development of a user-defined material subroutine that accounts for differences in damping in the x-, y-, and z- directions. A comparison of the Phase Three tape spring deployment geometry between the experiment and simulation is shown in Figure 4.41.

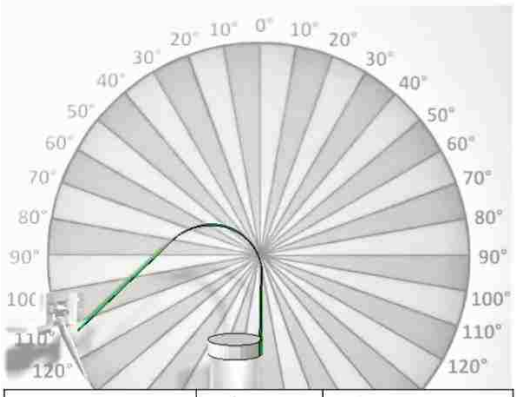

	Time [s]	Angle [deg]
Experiment	0	135
Simulation	0	134

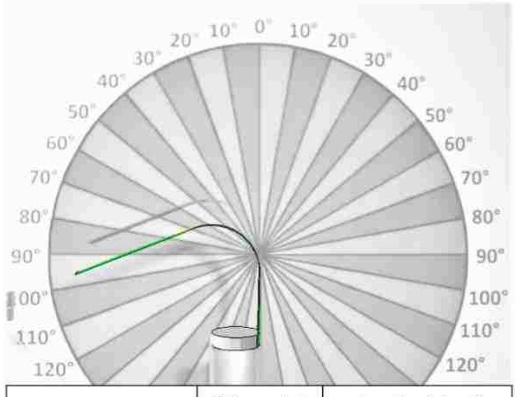

	Time [s]	Angle [deg]
Experiment	0.01938	110
Simulation	0.01927	117

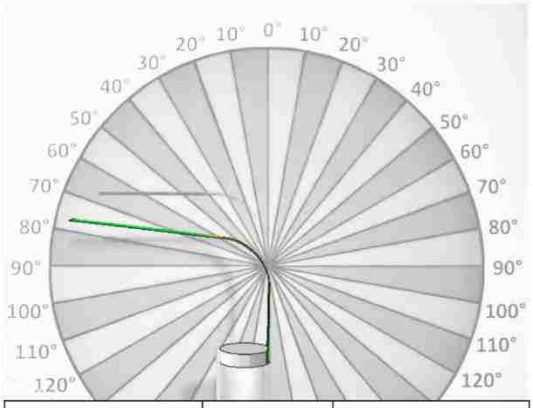

	Time [s]	Angle [deg]
Experiment	0.03000	90
Simulation	0.03019	88

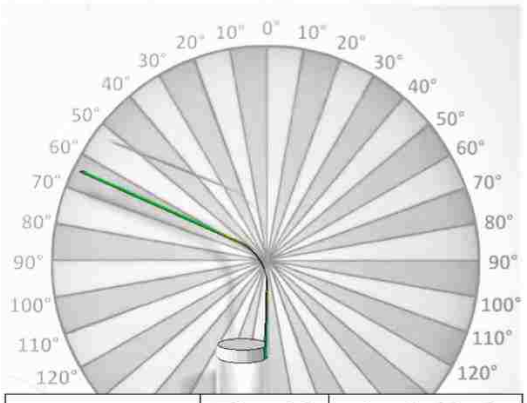

	Time [s]	Angle [deg]
Experiment	0.04062	70
Simulation	0.04044	59

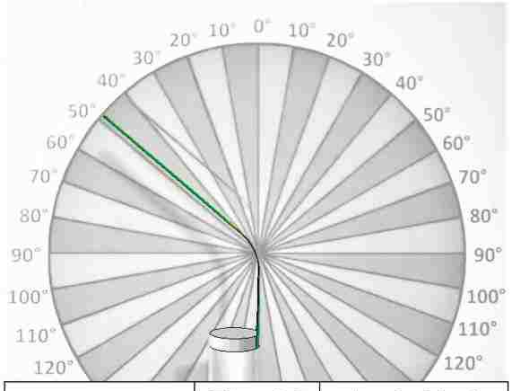

	Time [s]	Angle [deg]
Experiment	0.04500	60
Simulation	0.04440	63

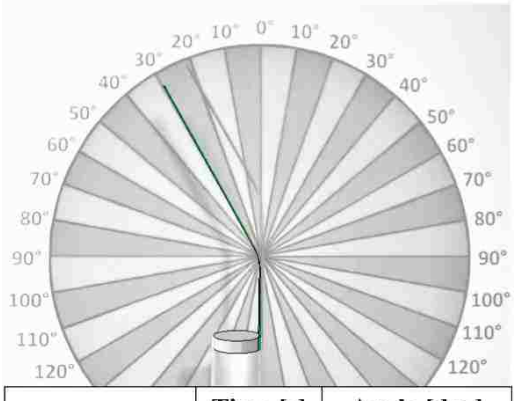

	Time [s]	Angle [deg]
Experiment	0.06250	30
Simulation	0.06239	29

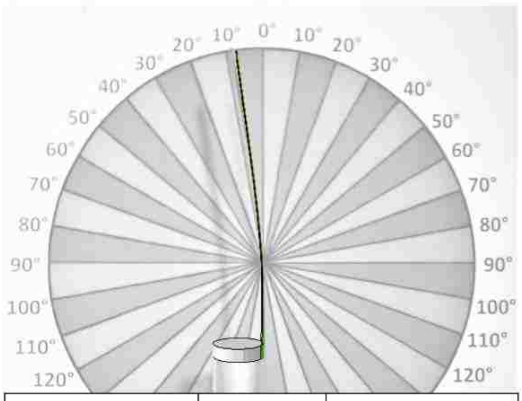

	Time [s]	Angle [deg]
Experiment	0.07375	8
Simulation	0.07400	8

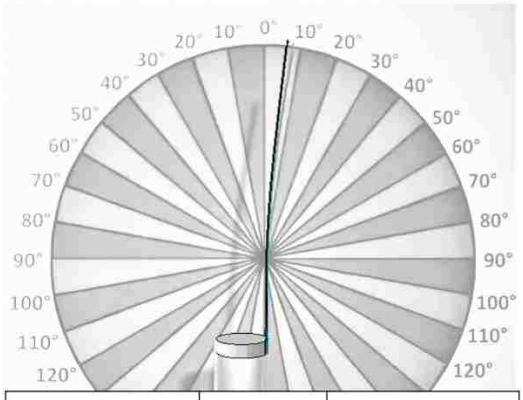

	Time [s]	Angle [deg]
Experiment	0.09625	-10
Simulation	0.09656	-7

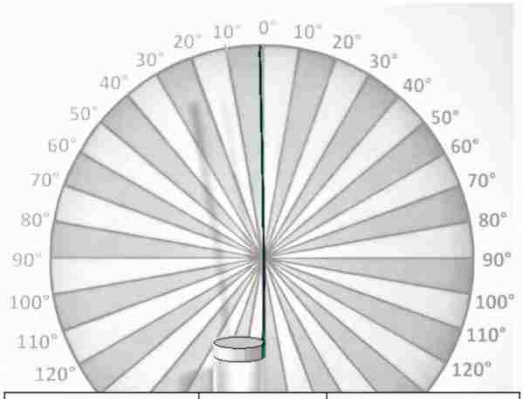

	Time [s]	Angle [deg]
Experiment	0.1275	15
Simulation	0.1273	13

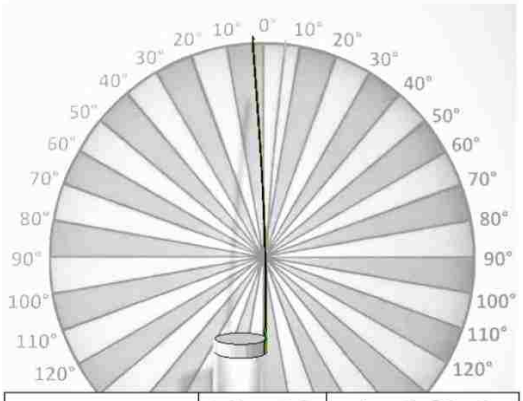

	Time [s]	Angle [deg]
Experiment	0.1575	-7
Simulation	0.1577	4

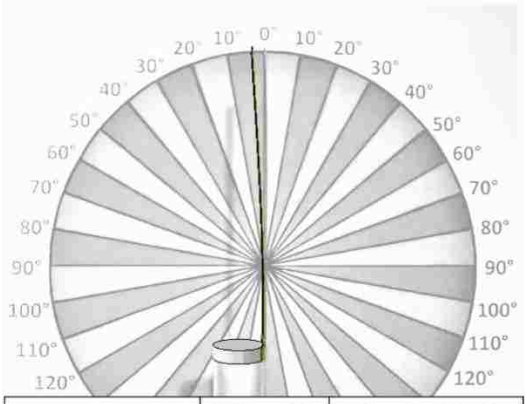

	Time [s]	Angle [deg]
Experiment	0.1688	0
Simulation	0.1698	3

Figure 4.41: An overlay comparison of deployment geometry between the Phase Three experiment and simulation in Abaqus.

A comparison between the experiment and simulation for Phases Two and Three deployment testing is shown in Figure 4.42. A closer match between the experiment and simulation is seen for Phase Two compared to Phase Three deployment testing. The increase in initial deployment time following stowage can be observed in both the experiment and simulation. However, the simulation results predict a slightly faster initial

deployment time than was observed experimentally and with slightly more initial overshoot.

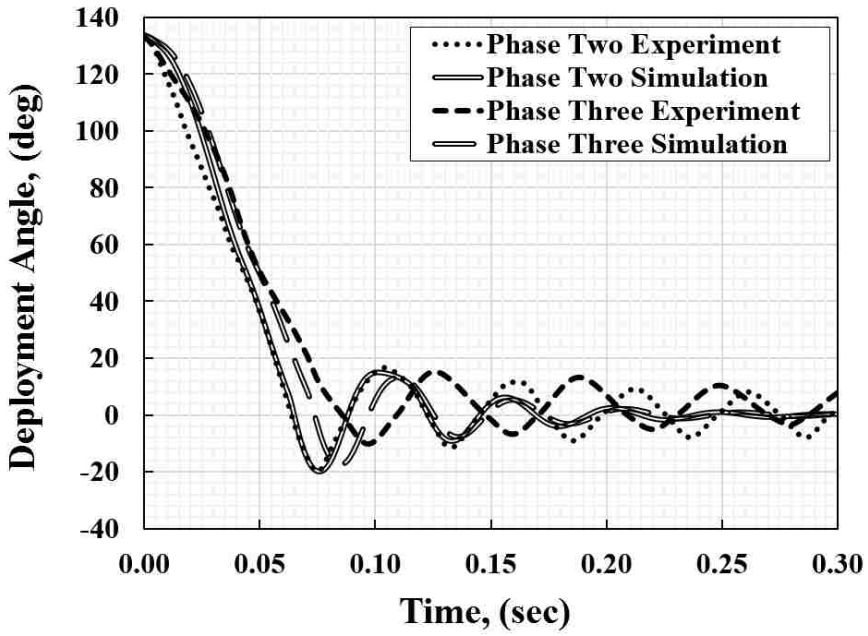

Figure 4.42: A comparison between experiment and simulation results of the Phases Two and Three deployment testing.

4.3.4 MESH SENSITIVITY ANALYSIS

A mesh sensitivity analysis was performed using the Phase Two deployment model. Mesh element sizes ranging from 0.5 mm to 4.0 mm were investigated. The results of the sensitivity analysis are shown in Figure 4.43(a). A close-up of the initial deployment and overshoot is shown in Figure 4.43(b), because these are the results of most interest in this study. The results display a slight shift to the right as mesh size decreases, but this does not have a considerable effect on the results. Therefore, a mesh size of 2.0 mm was used for all tape spring simulations presented herein.

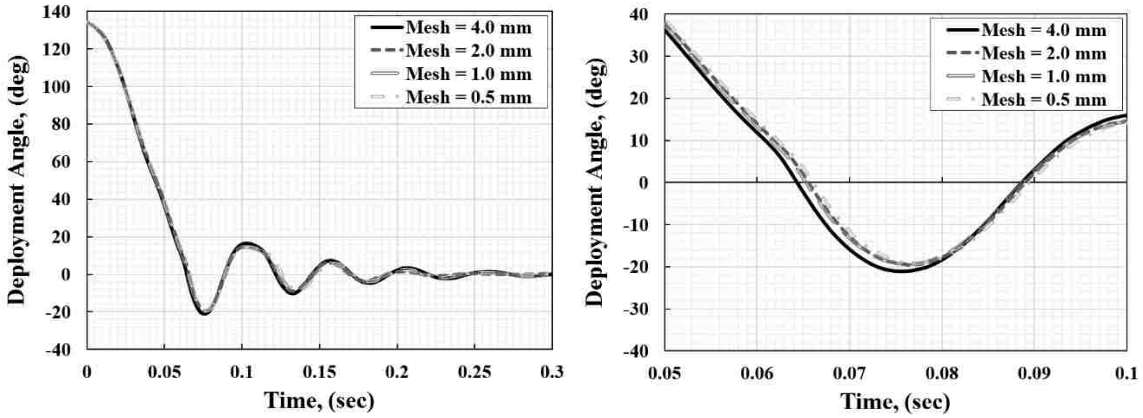

(a) (b)

Figure 4.43: (a) Mesh sensitivity results of Phase Two deployment in Abaqus. (b) Close-up of the first overshoot and rebound in the mesh sensitivity analysis.

4.3.5 EFFECT OF GRAVITY ON DEPLOYMENT

Although the intention of this research was to develop a model that could be verified and validated experimentally, meaning gravity was a necessary variable in the model, the final model was used to investigate the effects of gravity on deployment. For this purpose, the Phase Two model was ran without a defined gravity load, and the results are presented in Figure 4.44. The findings show that initially gravity slows deployment down slightly, as one might expect. However, likely due to the artificial damping, the simulated deployment response becomes identical both for the case of gravity and lack of gravity shortly after initial deployment. The results for the same investigation but without the damping definitions are shown in Figure 4.45. Without the artificial damping, it can be observed that the slowing down of the tape spring deployment response due to gravity actually becomes more prominent with time.

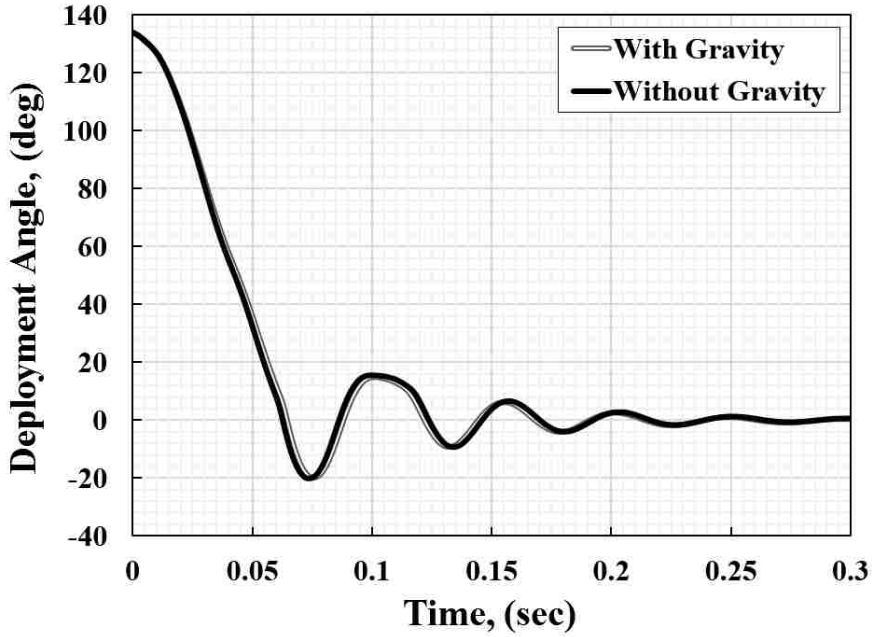

Figure 4.44. The effect of gravity on deployment in the Phase Two deployment model with damping.

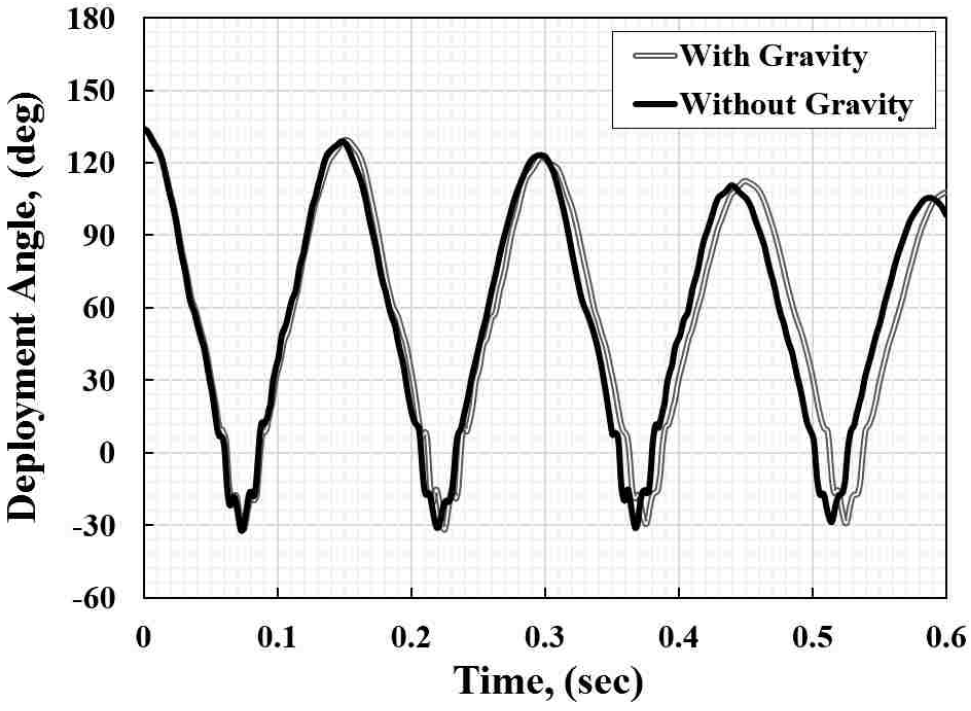

Figure 4.45. The effect of gravity on deployment in the Phase Two deployment model without damping.

4.4 APPLICATION OF MODEL

4.4.1 MASTER CURVES FOR HYPOTHETICAL EPOXIES

Once the tape spring stowage and deployment model had been validated and verified, it was used to investigate the effects of three hypothetical epoxies on the tape spring deployment. Epoxy A was based on a master curve for a 3501-6 epoxy resin provided by Kim and White (1996). The relaxation modulus of Epoxy A was 78% of its original modulus after six months. Epoxy B was generated by considering a relaxation modulus that was 50% of its initial modulus after six months, and Epoxy C was generated by considering a relaxation modulus that was 13% of its initial modulus after six months. The hypothetical master curves were sketched to depict the desired relaxation behaviors and then curve fit to find the Prony series coefficients for fourteen decades of time. The resultant master curves for the three hypothetical epoxies are shown in Figure 4.46. The Prony series coefficients for the three epoxies are shown in Table 9.

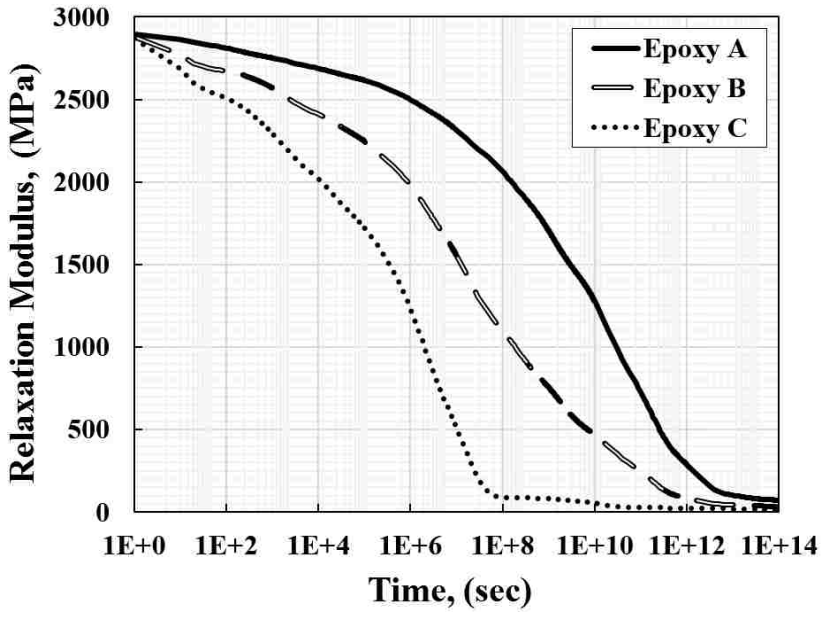

Figure 4.46: The master curves for three hypothetical epoxies depicting varying degrees of relaxation.

Table 9. The Prony series relaxation coefficients k_i and relaxation times τ_i for the three hypothetical epoxy resins.

	Prony A	**Prony B**	**Prony C**		**Prony A**	**Prony B**	**Prony C**
k_1	0.0191	0.0698	0.1138	τ_1	1.0 E+01	1.0 E+01	1.0 E+01
k_2	0.0207	0.0112	0.0352	τ_2	1.5 E+02	1.8 E+02	2.0 E+02
k_3	0.0202	0.0623	0.1026	τ_3	1.5 E+03	1.5 E+03	1.4 E+03
k_4	0.0232	0.0431	0.0921	τ_4	1.5 E+04	1.5 E+04	1.5 E+04
k_5	0.0200	0.0619	0.0901	τ_5	1.5 E+05	1.5 E+05	1.5 E+05
k_6	0.0432	0.1152	0.2510	τ_6	1.0 E+06	1.5 E+06	1.5 E+06
k_7	0.0723	0.1878	0.2844	τ_7	1.0 E+07	1.5 E+07	1.5 E+07
k_8	0.0857	0.1234	0.0000	τ_8	1.0 E+08	1.5 E+08	1.5 E+08
k_9	0.1482	0.1220	0.0034	τ_9	1.0 E+09	1.5 E+09	1.5 E+09
k_{10}	0.1902	0.0752	0.0183	τ_{10}	1.5 E+10	1.5 E+10	1.5 E+10
k_{11}	0.2038	0.0873	0.0003	τ_{11}	1.5 E+11	1.5 E+11	1.5 E+11
k_{12}	0.1100	0.0251	0.0004	τ_{12}	1.5 E+12	1.5 E+12	1.5 E+12
k_{13}	0.0168	0.0006	0.0026	τ_{13}	1.5 E+13	1.5 E+13	1.5 E+13
k_{14}	0.0033	0.0105	0.0054	τ_{14}	1.5 E+14	1.5 E+14	1.5 E+14

4.4.2 ENERGY DISSIPATION WITH HYPOTHETICAL EPOXIES

By entering the new Prony series coefficients into the UMAT and without changing anything else in the model, the energy dissipation over a stowage period of six months was examined for the three hypothetical epoxies. The results are shown in Figure 4.47. The difference in strain energy density in the plain weave lamina between the Epoxy A (0.52 J/mm^3) specimen and the Epoxy C (0.42 J/mm^3) specimen after six months of stowage was 0.1 J/mm^3.

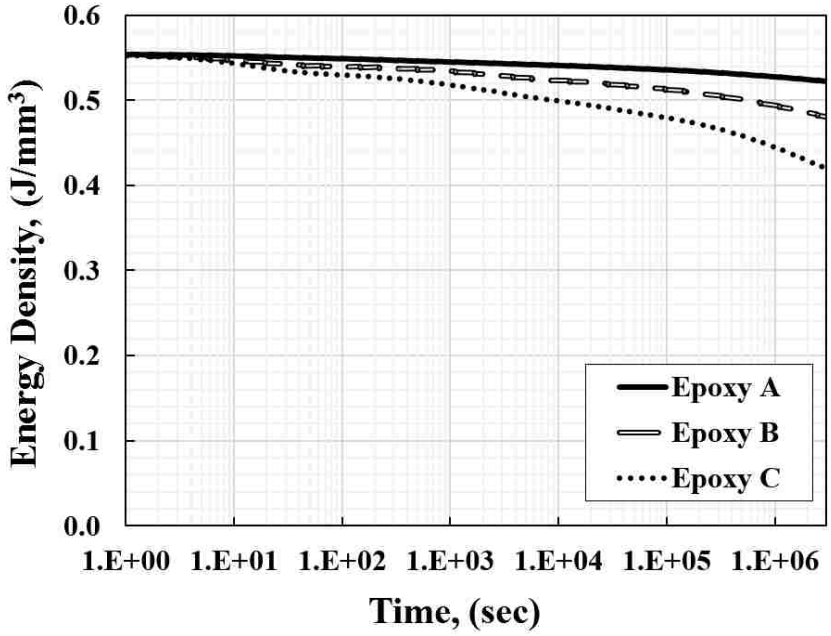

Figure 4.47. Comparison of strain energy density results between three hypothetical epoxies in a FlexLam tape spring stowed for six months using Abaqus.

4.4.3 DEPLOYMENT RESULTS WITH HYPOTHETICAL EPOXIES

The resultant change in deployment behavior for each of the three hypothetical epoxies was also compared. The results are shown in Figure 4.48. The difference in initial deployment time between Epoxy A and Epoxy C was 0.04 seconds, and the difference between the first overshoot for Epoxy A and Epoxy C was 6°. Since an aerospace-grade epoxy with a relaxation behavior as exaggerated as that depicted by hypothetical Epoxy C does not exist and would be extremely difficult to fabricate, these results portray an envelope of tailorable deployment behavior achievable by applying changes to the epoxy matrix alone in a FlexLam tape spring. If initial deployment were required to happen at a rate outside of this envelope, additional variables would need to be changed in the tape spring material and structural design to achieve the desired deployment speed.

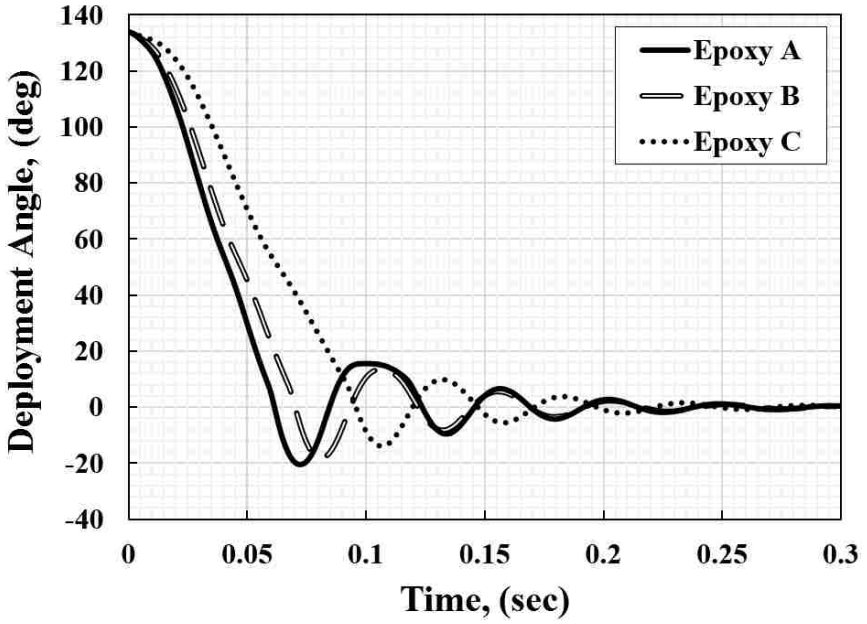

Figure 4.48: Comparison of deployment results between three hypothetical epoxies in a FlexLam tape spring after six months stowage using Abaqus.

4.4 DISCUSSION

For all three testing phases, considering restoring force, strain, and deployment angle, the finite element simulations were in good agreement with the experimental results. Strain was found to remain constant throughout the stowage period with gravity having an unperceivable effect. The restoring force during stowage was found to be in the range of 1.9 – 2.4 N with slight relaxation occurring over time. The simulation of tape spring deployment without stowage very closely matched the experimental results throughout the first two oscillations. The results of the deployment simulation following a 34-day stowage period suggest that more energy dissipation occurred than was predicted, likely due to the energy dissipation during initial deployment that was not completely captured by the Rayleigh damping definition. However, only one specimen was tested for each testing phase, so it is difficult to know the range of variability between tape springs for the same

stowage time duration. The difference between the deployment results of the experiment and simulation of Phase Three deployment testing could be within normal specimen testing variation. Aside from these minor differences, the relaxation predicted by the UMAT does result in a slower deployment with less overshoot following stowage as observed experimentally. In both models, the artificial damping quickly damped all oscillations in the tape spring which was not observed experimentally. This could be due to the limitations in Abaqus associated with using Rayleigh damping coefficients.

There are a few details of this study that stray somewhat from those defined in more traditional aerospace applications. For example, it is important to note that the cross-sectional curvature of the tape spring specimens used was considerably flat. Due to limited material availability, thin tape spring strips were cut from the CFRP slit tube boom for testing. In reality, a slit tube boom in its entirety would be used as a deployable spacecraft component with a cross-sectional curvature subtending nearly 360°. Such cross-sectional geometry requires a lot more energy to fold or roll than the energy required to overcome the small subtended angle of the tape spring specimens tested herein. Nevertheless, the purpose of this study was to develop a methodology for testing and simulating the effects of viscoelasticity on deployable composites. In achieving this aim, it is believed that this methodology could be scaled up and applied to different tape spring geometries.

It is also important to note that in aerospace applications stowed tape springs will likely undergo extreme thermal cycling. While the present investigation involved experimental testing and numerical simulations at ambient room temperatures, the model provides the option of defining various temperatures of interest. Master curves could be generated for an epoxy at temperatures of interest by assigning the necessary temperature

bounds during viscoelasticity testing and applying the appropriate TTSP shift factors to develop the master curves for future reference temperatures of interest.

An additional deviation in the experiment from traditional aerospace applications was the presence of gravity. Since gravity was present in the experiment, it was also included in the model. However, the model has the capability to simulate stowage and deployment without gravity. It is important to note, however, that the Rayleigh damping definition has the potential to mask the effects of gravity on deployment.

Comparing the experimental results of Phases Two and Three deployment testing, it can be observed that even a single month or so of stowage at room temperature has a noticeable effect on tape spring deployment response. However, this study remained within the range of mild stress relaxation. Higher temperatures or longer stowage periods would produce a more noticeable stress relaxation response. Although minor, the stress relaxation response was successfully captured using the novel TSSD fixture and was simulated numerically, fulfilling the intentions of this research. The stress relaxation predicted by the UMAT subroutine closely matched the relaxation measured experimentally.

The results of the hypothetical epoxy investigation suggest that applying changes to the epoxy matrix might not be enough to tailor deployment by a desired amount. The FlexLam tape spring design takes advantage of the viscoelastic material response of the epoxy resin matrix by orienting the outer woven plies off-axis. This allows for some stress relaxation to take place during stowage, resulting in a more controlled deployment compared to a composite tape spring entirely made up of on-axis fibers. Current ongoing research at UNM suggests that by altering the epoxy used in the off-axis plain weave layers of the tape spring, such as through the addition of nano-particles, it is possible to tailor the

relaxation response of the epoxy to some degree. However, the model developed herein predicts that even hypothetical epoxies with extreme relaxation responses do not have a considerable effect on tape spring deployment after approximately six months of stowage at room temperature for the tape spring geometry investigated. These results suggest that the consideration of additional means of tailoring tape spring deployment, in addition to the viscoelastic response of the epoxy matrix, would be beneficial.

CHAPTER 5 CONCLUSIONS AND RECOMMENDATIONS

5.1 CONCLUSIONS

The four main objectives of this research were fulfilled. First, material characterization of the FlexLam tape spring constituents was accomplished. The FlexLam tape spring consisted of three layers of carbon fiber reinforced polymer (CFRP) material. The outer layers consisted of a $\pm 45°$ plain weave (PW) lamina, and the middle layer was an on-axis $0°$ unidirectional (UD) lamina. This design provided dual benefits of flexibility in the outer layers to allow for high strain bending and of stiffness in the middle layer to contribute to successful deployment. However, the off-axis plain weave plies were prone to the effects of stress relaxation because of the high degree of strain experienced by the viscoelastic epoxy during stowage. Therefore, the development of a numerical simulation to predict the effects of viscoelasticity on tape spring deployment was deemed necessary to this investigation. The experimental testing required for this research included material and structural level testing. At the material level, material properties of the unidirectional composite material, plain weave composite material, and constituent epoxy resin were obtained through tension testing, fiber volume fraction testing, and stress relaxation testing using a dynamic mechanical analysis (DMA) machine. At the structural level, tape spring stowage and deployment testing was performed on small-scale tape spring hinges.

Second, a novel tape spring stowage and deployment (TSSD) fixture was designed and fabricated for the testing of long-term stowage and high-speed deployment of tape spring hinges. While experiments have been performed to investigate tape spring stowage or deployment independent of the other, this fixture is one of the first to combine both testing stages into a single testing fixture. In the TSSD fixture, the tape spring is folded and

held fixed for the required length of stowage time. During this time, temperature and restoring force data is continuously collected. A compression spring-loaded mechanism enables the instantaneous release of the boundary condition that maintains the tape spring's folded orientation, facilitating an undisturbed high-speed deployment. By recording the deployment with a high-speed digital camera, detailed investigation of the deployment behavior could be conducted. The TSSD testing was performed in three phases. Phase One involved a 28-day stowage period incorporating the use of strain gages. Phase Two lacked both a stowage period and strain gages. Lastly, Phase Three involved a 34-day stowage period without the use of strain gages. The three testing phases were performed to validate the testing setup and to investigate the effects of long-term stowage on deployment.

Third, a finite element model was developed that simulates and predicts the effects of viscoelasticity on deployment. This included the development of a user-defined material (UMAT) subroutine to model the viscoelasticity of an orthotropic CFRP composite. This work provided a necessary contribution to the realm of viscoelastic composites modeling. Presently, Abaqus finite element software is unable to model stress relaxation in materials other than those that are isotropic. Through the development of a UMAT subroutine, this research provides a methodology for simulating stress relaxation in a three-layer $[\pm 45° \; PW/0° UD/\pm 45° \; PW]$ CFRP tape spring to predict its effect on deployment.

Fourth, the validated and verified finite element model was used to predict the effects on deployment of using three hypothetical epoxies with varying degrees of stress relaxation. The results showed that even unrealistically high degrees of relaxation in an epoxy matrix did not result in very noticeable changes in tape spring deployment for a small-scale FlexLam tape spring stored at room temperature for six months. These results

suggest that it would be beneficial to consider changes to additional variables for the tailoring of tape spring deployment response.

5.2 LIMITATIONS OF STUDY

The limitations of this study include: (1) the research only investigated one tape spring geometry which was dimensionally smaller and had less transverse curvature than that commonly used in aerospace applications, (2) the stowage experiments were conducted solely at ambient room temperature while real aerospace applications involve thermal cycling and extreme temperature exposure, (3) the focus of this study was placed on the initial deployment behavior rather than the long-term deployment precision which would be important for space optics applications, (4) gravity was included in the experiments and simulations, (5) only a folded (concentrated strain) tape spring stowage configuration was considered rather than a rolled (distributed strain) configuration, (6) the tape spring was only stowed for approximately one month when in reality a tape spring may be stowed for anywhere between six months and several years, (7) only two stowage and two deployment tests were conducted, which were not enough to determine whether the results were statistically significant, and (8), in general, composite tape springs are designed to withstand high strains (approaching 10%) and high temperatures (around $100°C$), while this early investigation into deployable composite tape springs only begins to approach the full capacity of tape spring potential.

5.3 FUTURE WORK

The work conducted for this thesis has laid the foundation for tape spring stowage and deployment testing and modeling. Now that the methodology has been established, it will be important to guide it toward more realistic aerospace applications and conditions by applying thermal cycling, zero gravity conditions, and other aerospace conditions described in the limitations of this study.

The next step in this research is to simulate longer-term stowage through the increase in temperature of the stowage environment. Since the current investigation only begins to investigate the early effects of stress relaxation on tape spring deployment, deeper investigation into long-term stowage would be beneficial. By applying the TTSP principle, long-term stowage can be simulated by conducting short-term stowage experiments at higher temperatures. Although these investigations were beyond the scope the work presented herein, a detailed description of these future efforts is provided.

The first step will require the development of master curves for the PMT-F7 epoxy resin at higher temperatures, such as between $50°C$ and $70°C$. From these master curves, the required amount of time in stowage can be estimated. To see considerable relaxation, the "knee" of the master curve (or the significant drop in relaxation modulus that occurs as the epoxy approaches its glass transition temperature) should be reached. It is anticipated that only a few hours of stowage at a high temperature will results in a considerable and visually-observable effect on deployment. Due to the inability to place the instrumental equipment (such as the load cell) of the TSSD fixture in an oven, stowage can be replicated by running a long screw of length 74 mm through the folded tape spring and securing it was a washer and nut at each end. This will provide portability to the stowed tape spring,

allowing it to be stored in an oven for the desired length of time. Once removed from the oven, the tape spring can be secured to the TSSD fixture via the steel hose clamp and positioned against the load cell boundary condition while the nuts, washers, and screw are carefully removed without disturbing the stowage configuration. Then the quick release pin of the TSSD fixture could be pulled, and the tape spring deployment could be filmed as achieved in the work presented herein, maintaining the versatility of the TSSD fixture. This will allow for a comparison of tape spring deployment following different stowage temperatures and times for a more complete investigation into a wide range of stowage conditions. The deployment could be simulated using the same finite element model and user-defined material subroutine by curve fitting the new master curve with MatLab and defining the new Prony series coefficients in the UMAT subroutine. The hold time of the stowage step will also need to be updated in the finite element model. Once these two changes have been made, the model should simulate the deployment behavior observed experimentally with good accuracy.

The results of this research suggest that tailoring tape spring deployment might best be achieved through a multi-objective topological optimization of tape springs. Previously, it had been thought that tailoring the viscoelastic response of the epoxy matrix, such as through the inclusion of nano-particles, would be enough to tailor the deployment behavior of a tape spring to achieve any desirable controlled deployment speed. However, the results of this research suggest that the envelope of possible deployment speeds achievable through changes in the epoxy relaxation behavior is narrow. Increased opportunity for tailored deployment behavior is expected when considering multiple design variables and their effect on tape spring deployment behavior.

This research is intended as preparation for future research on optimization of tape spring structures through the developed framework for accurately designing, testing, and modeling viscoelastic orthotropic composite tape springs. In the future, this tool could be applied to multi-variable optimization of tape spring structures. Through a series of changes made to the material properties or geometric definitions in the finite element model, the effect of variable changes on stress relaxation and deployment could be identified. By automating the iterative optimization process, tape spring design could be tailored to meet specific deployment needs. Automated fabrication could be achievable through the 3D printing of optimized tape spring designs. Once fabricated, these optimized tape springs could then be tested in the TSSD fixture to verify the deployment response predicted by the model. This would provide insight into tape spring designs that minimize viscoelastic effects or exploit matrix viscoelasticity to benefit deployment depending on the needs of the specific deployment applications and the interests of the customer.

Future investigations into the effects of nano-constituents incorporated into CFRP tape spring fabrication promises to be a useful component in the tailoring of material properties to meet the design needs for deployable composite structures. Through the development of a seamless framework connecting stress relaxation testing of an epoxy matrix to structural level simulations of deployment, the resultant methodology has paved the way for researching the effects of nano-constituents on the viscoelasticity of epoxy constituent materials, and furthermore, the effect of that viscoelasticity on the deployment of a composite tape spring containing the nano-composite epoxy. The long-term goal, in which this research plays only a beginning role, is to enable an automated design and

fabrication process for tailoring deployable high strain composites to meet specific application needs.

An automated design and fabrication process will likely incorporate 3D printing technology. This would allow for multi-variable spatial optimization to consider gradient variable changes along all major axes, and the optimized tape spring designs could be fabricated by 3D printing. For example, Irisarri and Le Riche (2014) show gradient changes in thickness and ply distribution that is possible to fabricate in composite laminates using 3D printing following topology optimization of the tape spring design. To print FRP tape springs, a 3D printing apparatus with printheads for multi-material printing will be necessary for creating heterogeneous composites. Through layered printing methods, various FRP layup designs could be achieved. These may consist of on-axis unidirectional fibers with varying degrees of fiber spacing or incorporate some plies of on-axis and off-axis plain weave fiber fabrics, as well. Some examples of such possibilities are discussed further by Tymrak (2014).

In conclusion, the results of this study suggest that tailoring the relaxation response of the epoxy matrix is not enough to fully tailor the deployment response of a stored strain energy deployable composite tape spring. By applying multi-variable spatial optimization and 3D printing technology to the tape spring stowage and deployment testing and simulation framework developed herein, the possibilities for tailored tape spring deployment will be expanded. Such continuation of this work would enter the realm of automated design, fabrication, and testing of aerospace materials and structures for expedited research findings and technological progress.

APPENDIX A. ABAQUS INPUT FILE

```
*HEADING
*INCLUDE, INPUT=.inc
**
** Generated by: Abaqus/CAE 6.14-1
*Preprint, echo=NO, model=NO, history=NO, contact=NO
**
** PARTS
**
*Part, name=Cylinder
*End Part
**
*Part, name=TapeSpring
*Element, type=S4R
*Nset, nset=Fixed
*Nset, nset=Mid
*Nset, nset=NodeA
*Nset, nset=NodeB
*Nset, nset=NodeB_Below
*Nset, nset=Surfaces
**
** Region: (ConvShell-1: Generated From Layup)
*Elset, elset=ConvShell-1, generate
   1,  2156,     1
** Section: ConvShell-1
*Shell Section, elset=ConvShell-1, composite, layup=ConvShell
0.192, 3, PW-UMAT-34Day, 45., Ply-1
0.096, 3, UD, 0., Ply-2
0.192, 3, PW-UMAT-34Day, 45., Ply-3
*Transverse Shear
919., 919., 900.
*End Part
**
** ASSEMBLY
**
*Assembly, name=Assembly
**
*Instance, name=TS, part=TapeSpring
*End Instance
**
*Instance, name=Cyl, part=Cylinder
*Element, type=C3D8R
*Nset, nset=_PickedSet21, internal, generate
*Elset, elset=_PickedSet21, internal, generate
** Section: Aluminum
```

```
*Solid Section, elset=_PickedSet21, material=Aluminum
*End Instance
**
*Nset, nset=All, instance=TS
*Elset, elset=All, instance=TS
*Nset, nset=Mid, instance=TS
*Nset, nset=NodeA, instance=TS
*Nset, nset=NodeB, instance=TS
*Nset, nset=NodeB_Below, instance=TS
**
*Nset, nset=_PickedSet76, internal, instance=Cyl
*Elset, elset=_PickedSet76, internal, instance=Cyl
*Elset, elset=__PickedSurf75_S5, internal, instance=Cyl
*Elset, elset=__PickedSurf75_S4, internal, instance=Cyl
*Elset, elset=__PickedSurf75_S6, internal, instance=Cyl
*Elset, elset=__PickedSurf75_S3, internal, instance=Cyl
**
*Surface, type=ELEMENT, name=_PickedSurf75, internal
__PickedSurf75_S5, S5
__PickedSurf75_S4, S4
__PickedSurf75_S6, S6
__PickedSurf75_S3, S3
**
** Constraint: Constraint-1
*Adjust, node set=TS.Surfaces, surface=_PickedSurf75
*End Assembly
**
** MATERIALS
**
*Material, name=Aluminum
*Density
 2.7e-09,
*Elastic
69000., 0.33
**
*Material, name=PW-UMAT-34Day
*Damping, alpha=0.05
*Density
 1.5e-09,
*Depvar
     17,
*User Material, constants=6
276000.,19000., 1482.,  0.34,   0.2,  0.53
**
*Material, name=UD
*Damping, alpha=0.05, beta=0.0029
```

```
*Density
 1.5e-09,
*Elastic, type=LAMINA
122204.,12220.,  0.27, 4753., 4753., 3898.
**
** BOUNDARY CONDITIONS
**
** Name: Cylinder Type: Symmetry/Antisymmetry/Encastre
*Boundary
_PickedSet76, ENCASTRE
**
** Name: Fixed Type: Symmetry/Antisymmetry/Encastre
*Boundary
TS.Fixed, ENCASTRE
**
** ----------------------------------------------------------------
**
** STEP: Step-1_Z
**
*Step, name=Step-1_Z, nlgeom=YES, inc=1000000
*Dynamic,application=QUASI-STATIC,initial=NO
0.01,1.2,1e-08
**
** BOUNDARY CONDITIONS
**
** Name: BC-Z Type: Displacement/Rotation
*Boundary
TS.NodeB, 3, 3, -30.
**
** Name: Roller Type: Displacement/Rotation
*Boundary
TS.NodeA, 2, 2
TS.NodeA, 4, 4
TS.NodeA, 6, 6
**
** LOADS
**
** Name: Gravity   Type: Gravity
*Dload
, GRAV, 9810., -1., 0., 0.
**
** OUTPUT REQUESTS
**
*Restart, write, frequency=0
**
** FIELD OUTPUT: F-Output-1
```

```
*Output, field, frequency=1
*Node Output
RF, U
*Element Output, directions=YES
E, ENER, S, SDV
**
** FIELD OUTPUT: Lamina
*Element Output, elset=TS.ConvShell-1, directions=YES
2, 5, 8
E, ENER, S, SDV
**
** HISTORY OUTPUT: Energy
*Output, history, frequency=1
*Energy Output
ALLVD, ETOTAL
**
** HISTORY OUTPUT: Strain
** HISTORY OUTPUT: Stress
** HISTORY OUTPUT: RF_B
*Node Output, nset=TS.NodeB
RF1, RF3
**
** HISTORY OUTPUT: RF_Bbelow
*Node Output, nset=TS.NodeB_Below
RF1, RF3
*End Step
**
** ----------------------------------------------------------------
**
** STEP: Step-2_X
**
*Step, name=Step-2_X, nlgeom=YES, inc=1000000
*Dynamic,application=QUASI-STATIC,initial=NO
0.01,0.2,1e-08
**
** BOUNDARY CONDITIONS
**
** Name: BC-X Type: Displacement/Rotation
*Boundary, op=NEW
TS.NodeB, 1, 1, -150.
**
** Name: BC-Z Type: Displacement/Rotation
*Boundary, op=NEW
**
** Name: Cylinder Type: Symmetry/Antisymmetry/Encastre
*Boundary, op=NEW
```

```
_PickedSet76, ENCASTRE
**
** Name: FixSurface Type: Displacement/Rotation
*Boundary, op=NEW, fixed
TS.Surfaces, 1, 1
TS.Surfaces, 2, 2
TS.Surfaces, 3, 3
TS.Surfaces, 4, 4
TS.Surfaces, 5, 5
TS.Surfaces, 6, 6
**
** Name: Fixed Type: Symmetry/Antisymmetry/Encastre
*Boundary, op=NEW
TS.Fixed, ENCASTRE
**
** Name: Roller Type: Displacement/Rotation
*Boundary, op=NEW
TS.NodeA, 2, 2
TS.NodeA, 4, 4
TS.NodeA, 6, 6
**
** OUTPUT REQUESTS
**
*Restart, write, frequency=0
**
** FIELD OUTPUT: F-Output-1
*Output, field, frequency=1
*Node Output
RF, U
*Element Output, directions=YES
E, ENER, S, SDV
**
** FIELD OUTPUT: Lamina
*Element Output, elset=TS.ConvShell-1, directions=YES
2, 5, 8
E, ENER, S, SDV
**
** HISTORY OUTPUT: Energy
*Output, history, frequency=1
*Energy Output
ALLVD, ETOTAL
**
** HISTORY OUTPUT: Strain
** HISTORY OUTPUT: Stress
** HISTORY OUTPUT: RF_B
*Node Output, nset=TS.NodeB
```

```
RF1, RF3
**
** HISTORY OUTPUT: RF_Bbelow
*Node Output, nset=TS.NodeB_Below
RF1, RF3
*End Step
**
** ----------------------------------------------------------------
**
** STEP: Step-3_B
**
*Step, name=Step-3_B, nlgeom=YES, inc=1000000
*Dynamic,application=QUASI-STATIC,initial=NO
0.01,1.6,1e-08
**
** BOUNDARY CONDITIONS
**
** Name: BC-B Type: Displacement/Rotation
*Boundary, op=NEW
TS.NodeB, 1, 1, -206.
TS.NodeB, 3, 3, -74.
**
** Name: BC-Bbelow-Fold Type: Displacement/Rotation
*Boundary, op=NEW
TS.NodeB_Below, 3, 3, -73.7
**
** Name: BC-X Type: Displacement/Rotation
*Boundary, op=NEW
**
** Name: Cylinder Type: Symmetry/Antisymmetry/Encastre
*Boundary, op=NEW
_PickedSet76, ENCASTRE
**
** Name: FixSurface Type: Displacement/Rotation
*Boundary, op=NEW, fixed
TS.Surfaces, 1, 1
TS.Surfaces, 2, 2
TS.Surfaces, 3, 3
TS.Surfaces, 4, 4
TS.Surfaces, 5, 5
TS.Surfaces, 6, 6
**
** Name: Fixed Type: Symmetry/Antisymmetry/Encastre
*Boundary, op=NEW
TS.Fixed, ENCASTRE
**
```

```
** Name: Roller Type: Displacement/Rotation
*Boundary, op=NEW
TS.NodeA, 2, 2
TS.NodeA, 4, 4
TS.NodeA, 6, 6
**
** OUTPUT REQUESTS
**
*Restart, write, frequency=0
**
** FIELD OUTPUT: F-Output-1
*Output, field, frequency=1
*Node Output
RF, U
*Element Output, directions=YES
E, ENER, S, SDV
**
** FIELD OUTPUT: Lamina
*Element Output, elset=TS.ConvShell-1, directions=YES
2, 5, 8
E, ENER, S, SDV
**
** HISTORY OUTPUT: Energy
*Output, history, frequency=1
*Energy Output
ALLVD, ETOTAL
**
** HISTORY OUTPUT: Strain
** HISTORY OUTPUT: Stress
** HISTORY OUTPUT: RF_B
*Node Output, nset=TS.NodeB
RF1, RF3
**
** HISTORY OUTPUT: RF_Bbelow
*Node Output, nset=TS.NodeB_Below
RF1, RF3
*End Step
**
** ----------------------------------------------------------------
**
** STEP: Step-4_Tighten
**
*Step, name=Step-4_Tighten, nlgeom=YES, inc=10000000
*Dynamic,application=QUASI-STATIC,initial=NO
0.01,0.6,1e-09
**
```

```
** BOUNDARY CONDITIONS
**
** Name: BC-B Type: Displacement/Rotation
*Boundary, op=NEW
TS.NodeB, 1, 1, -202.
TS.NodeB, 3, 3, -74.
**
** Name: BC-B_Below Type: Displacement/Rotation
*Boundary, op=NEW
TS.NodeB_Below, 3, 3, -74.
**
** Name: BC-Bbelow-Fold Type: Displacement/Rotation
*Boundary, op=NEW
**
** Name: Cylinder Type: Symmetry/Antisymmetry/Encastre
*Boundary, op=NEW
_PickedSet76, ENCASTRE
**
** Name: FixSurface Type: Displacement/Rotation
*Boundary, op=NEW, fixed
TS.Surfaces, 1, 1
TS.Surfaces, 2, 2
TS.Surfaces, 3, 3
TS.Surfaces, 4, 4
TS.Surfaces, 5, 5
TS.Surfaces, 6, 6
**
** Name: Fixed Type: Symmetry/Antisymmetry/Encastre
*Boundary, op=NEW
TS.Fixed, ENCASTRE
**
** Name: Roller Type: Displacement/Rotation
*Boundary, op=NEW
TS.NodeA, 2, 2
TS.NodeA, 4, 4
TS.NodeA, 6, 6
**
** OUTPUT REQUESTS
**
*Restart, write, frequency=0
**
** FIELD OUTPUT: F-Output-1
*Output, field, frequency=1
*Node Output
RF, U
*Element Output, directions=YES
```

```
E, ENER, S, SDV
**
** FIELD OUTPUT: Lamina
*Element Output, elset=TS.ConvShell-1, directions=YES
2, 5, 8
E, ENER, S, SDV
**
** HISTORY OUTPUT: Energy
*Output, history, frequency=1
*Energy Output
ALLVD, ETOTAL
**
** HISTORY OUTPUT: Strain
** HISTORY OUTPUT: Stress
** HISTORY OUTPUT: RF_B
*Node Output, nset=TS.NodeB
RF1, RF3
**
** HISTORY OUTPUT: RF_Bbelow
*Node Output, nset=TS.NodeB_Below
RF1, RF3
*End Step
**
** ----------------------------------------------------------------
**
** STEP: Step-5_Hold
**
*Step, name=Step-5_Hold, nlgeom=YES, inc=1000000000
2.938e+6 is 34 days, 2.419e+6 is 28 days, 1.577e+7 is 6 months
*Dynamic,application=QUASI-STATIC,initial=NO
1e-05,2.938e+06,1e-15
**
** BOUNDARY CONDITIONS
**
** Name: BC-B Type: Displacement/Rotation
*Boundary, op=NEW
**
** Name: BC-B_Below Type: Displacement/Rotation
*Boundary, op=NEW
**
** Name: Cylinder Type: Symmetry/Antisymmetry/Encastre
*Boundary, op=NEW
_PickedSet76, ENCASTRE
**
** Name: FixSurface Type: Displacement/Rotation
*Boundary, op=NEW, fixed
```

```
TS.Surfaces, 1, 1
TS.Surfaces, 2, 2
TS.Surfaces, 3, 3
TS.Surfaces, 4, 4
TS.Surfaces, 5, 5
TS.Surfaces, 6, 6
**
** Name: Fixed Type: Symmetry/Antisymmetry/Encastre
*Boundary, op=NEW
TS.Fixed, ENCASTRE
**
** Name: Hold_B Type: Displacement/Rotation
*Boundary, op=NEW, fixed
TS.NodeB, 1, 1
TS.NodeB, 2, 2
TS.NodeB, 3, 3
TS.NodeB, 4, 4
TS.NodeB, 5, 5
TS.NodeB, 6, 6
**
** Name: Hold_Bbelow Type: Displacement/Rotation
*Boundary, op=NEW, fixed
TS.NodeB_Below, 1, 1
TS.NodeB_Below, 2, 2
TS.NodeB_Below, 3, 3
TS.NodeB_Below, 4, 4
TS.NodeB_Below, 5, 5
TS.NodeB_Below, 6, 6
**
** Name: Roller Type: Displacement/Rotation
*Boundary, op=NEW
TS.NodeA, 2, 2
TS.NodeA, 4, 4
TS.NodeA, 6, 6
**
** OUTPUT REQUESTS
**
*Restart, write, frequency=0
**
** FIELD OUTPUT: F-Output-1
*Output, field, frequency=1
*Node Output
RF, U
*Element Output, directions=YES
E, ENER, S, SDV
**
```

```
** FIELD OUTPUT: Lamina
*Element Output, elset=TS.ConvShell-1, directions=YES
2, 5, 8
E, ENER, S, SDV
**
** HISTORY OUTPUT: Energy
*Output, history, frequency=1
*Energy Output
ALLVD, ETOTAL
**
** HISTORY OUTPUT: Strain
** HISTORY OUTPUT: Stress
** HISTORY OUTPUT: RF_B
*Node Output, nset=TS.NodeB
RF1, RF3
**
** HISTORY OUTPUT: RF_Bbelow
*Node Output, nset=TS.NodeB_Below
RF1, RF3
*End Step
**
** ----------------------------------------------------------------
**
** STEP: Step-6_Unscrew
**
*Step, name=Step-6_Unscrew, nlgeom=YES, inc=100000000
*Dynamic,application=QUASI-STATIC,initial=NO
1e-05,0.6,1e-10
**
** BOUNDARY CONDITIONS
**
** Name: BC-B_Loosen Type: Displacement/Rotation
*Boundary, op=NEW
TS.NodeB_Below, 3, 3, -73.7
**
** Name: Cylinder Type: Symmetry/Antisymmetry/Encastre
*Boundary, op=NEW
_PickedSet76, ENCASTRE
**
** Name: FixSurface Type: Displacement/Rotation
*Boundary, op=NEW, fixed
TS.Surfaces, 1, 1
TS.Surfaces, 2, 2
TS.Surfaces, 3, 3
TS.Surfaces, 4, 4
TS.Surfaces, 5, 5
```

```
TS.Surfaces, 6, 6
**
** Name: Fixed Type: Symmetry/Antisymmetry/Encastre
*Boundary, op=NEW
TS.Fixed, ENCASTRE
**
** Name: Hold_B Type: Displacement/Rotation
*Boundary, op=NEW
**
** Name: Hold_Bbelow Type: Displacement/Rotation
*Boundary, op=NEW
**
** Name: Roller Type: Displacement/Rotation
*Boundary, op=NEW
TS.NodeA, 2, 2
TS.NodeA, 4, 4
TS.NodeA, 6, 6
**
** OUTPUT REQUESTS
**
*Restart, write, frequency=0
**
** FIELD OUTPUT: F-Output-1
*Output, field, frequency=1
*Node Output
RF, U
*Element Output, directions=YES
E, ENER, S, SDV
**
** FIELD OUTPUT: Lamina
*Element Output, elset=TS.ConvShell-1, directions=YES
2, 5, 8
E, ENER, S, SDV
**
** HISTORY OUTPUT: Energy
*Output, history, frequency=1
*Energy Output
ALLVD, ETOTAL
**
** HISTORY OUTPUT: Strain
** HISTORY OUTPUT: Stress
** HISTORY OUTPUT: RF_B
*Node Output, nset=TS.NodeB
RF1, RF3
**
** HISTORY OUTPUT: RF_Bbelow
```

```
*Node Output, nset=TS.NodeB_Below
RF1, RF3
*End Step
**
** ----------------------------------------------------------------
**
** STEP: Step-7_ContDeploy
**
*Step, name=Step-7_ContDeploy, nlgeom=YES, inc=1000000000
*Dynamic
1e-13,0.7,4e-16
**
** BOUNDARY CONDITIONS
**
** Name: BC-B_Loosen Type: Displacement/Rotation
*Boundary, op=NEW
**
** Name: ContDepX Type: Displacement/Rotation
*Boundary, op=NEW
TS.NodeA, 1, 1, -280.
**
** Name: ContDepZ_1 Type: Displacement/Rotation
*Boundary, op=NEW
TS.NodeA, 3, 3, -170.
**
** Name: Cylinder Type: Symmetry/Antisymmetry/Encastre
*Boundary, op=NEW
_PickedSet76, ENCASTRE
**
** Name: FixSurface Type: Displacement/Rotation
*Boundary, op=NEW, fixed
TS.Surfaces, 1, 1
TS.Surfaces, 2, 2
TS.Surfaces, 3, 3
TS.Surfaces, 4, 4
TS.Surfaces, 5, 5
TS.Surfaces, 6, 6
**
** Name: Fixed Type: Symmetry/Antisymmetry/Encastre
*Boundary, op=NEW
TS.Fixed, ENCASTRE
**
** Name: Roller Type: Displacement/Rotation
*Boundary, op=NEW
TS.NodeA, 2, 2
TS.NodeA, 4, 4
```

```
TS.NodeA, 6, 6
**
** OUTPUT REQUESTS
**
*Restart, write, frequency=0
**
** FIELD OUTPUT: F-Output-1
*Output, field, frequency=1
*Node Output
RF, U
*Element Output, directions=YES
E, ENER, S, SDV
**
** FIELD OUTPUT: Lamina
*Element Output, elset=TS.ConvShell-1, directions=YES
2, 5, 8
E, ENER, S, SDV
**
** HISTORY OUTPUT: Energy
*Output, history, frequency=1
*Energy Output
ALLVD, ETOTAL
**
** HISTORY OUTPUT: Strain
** HISTORY OUTPUT: Stress
** HISTORY OUTPUT: RF_B
*Node Output, nset=TS.NodeB
RF1, RF3
**
** HISTORY OUTPUT: RF_Bbelow
*Node Output, nset=TS.NodeB_Below
RF1, RF3
*End Step
**
** ----------------------------------------------------------------
**
** STEP: Step-8_FreeDeploy
**
*Step, name=Step-8_FreeDeploy, nlgeom=YES, inc=100000000
*Dynamic
0.0001,0.3,1e-12
**
** BOUNDARY CONDITIONS
**
** Name: ContDepX Type: Displacement/Rotation
*Boundary, op=NEW
```

```
**
** Name: ContDepZ_1 Type: Displacement/Rotation
*Boundary, op=NEW
**
** Name: Cylinder Type: Symmetry/Antisymmetry/Encastre
*Boundary, op=NEW
_PickedSet76, ENCASTRE
**
** Name: FixSurface Type: Displacement/Rotation
*Boundary, op=NEW, fixed
TS.Surfaces, 1, 1
TS.Surfaces, 2, 2
TS.Surfaces, 3, 3
TS.Surfaces, 4, 4
TS.Surfaces, 5, 5
TS.Surfaces, 6, 6
**
** Name: Fixed Type: Symmetry/Antisymmetry/Encastre
*Boundary, op=NEW
TS.Fixed, ENCASTRE
**
** Name: Roller Type: Displacement/Rotation
*Boundary, op=NEW
TS.NodeA, 2, 2
TS.NodeA, 4, 4
TS.NodeA, 6, 6
**
** OUTPUT REQUESTS
**
*Restart, write, frequency=0
**
** FIELD OUTPUT: F-Output-1
*Output, field, frequency=1
*Node Output
RF, U
*Element Output, directions=YES
E, ENER, S, SDV
**
** FIELD OUTPUT: Lamina
*Element Output, elset=TS.ConvShell-1, directions=YES
2, 5, 8
E, ENER, S, SDV
**
** HISTORY OUTPUT: Energy
*Output, history, frequency=1
*Energy Output
```

ALLVD, ETOTAL
**
** HISTORY OUTPUT: Strain
** HISTORY OUTPUT: Stress
** HISTORY OUTPUT: Rotation
*Node Output, nset=TS.NodeA
UR2,
**
** HISTORY OUTPUT: RF_B
*Node Output, nset=TS.NodeB
RF1, RF3
**
** HISTORY OUTPUT: RF_Bbelow
*Node Output, nset=TS.NodeB_Below
RF1, RF3
**
*End Step

APPENDIX B. UMAT SUBROUTINE

```
************************************************************************
*USER SUBROUTINE
          SUBROUTINE UMAT(STRESS,STATEV,DDSDDE,SSE,SPD,SCD,
     1 RPL,DDSDDT,DRPLDE,DRPLDT,
     2 STRAN,DSTRAN,TIME,DTIME,TEMP,DTEMP,PREDEF,DPRED,CMNAME,
     3 NDI,NSHR,NTENS,NSTATV,PROPS,NPROPS,COORDS,DROT,PNEWDT,
     4 CELENT,DFGRD0,DFGRD1,NOEL,NPT,LAYER,KSPT,KSTEP,KINC)
C
      INCLUDE 'ABA_PARAM.INC'
C
      CHARACTER*80 CMNAME
      DIMENSION STRESS(NTENS),STATEV(NSTATV),
     1 DDSDDE(NTENS,NTENS),DDSDDT(NTENS),DRPLDE(NTENS),
     2 STRAN(NTENS),DSTRAN(NTENS),TIME(2),PREDEF(1),DPRED(1),
     3 PROPS(NPROPS),COORDS(3),DROT(3,3),DFGRD0(3,3),DFGRD1(3,3)

      DIMENSION depsilon(NTENS), epsilonE(NTENS), sigmaE(NTENS)
      DIMENSION E(NTENS)
      DIMENSION CFULL(3,3)

C     DEFINE VARIABLES

      DOUBLE PRECISION:: t1,t2,t3,t4,t5,t6,t7,t8,t9,t10,t11,t12,t13,t14
      DOUBLE PRECISION:: k1,k2,k3,k4,k5,k6,k7,k8,k9,k10,k11,k12,k13,k14
      DOUBLE PRECISION:: b1,b2,b3,b4,b5,b6,b7,b8,b9,b10,b11,b12,b13,b14
      DOUBLE PRECISION:: EMT, GMT, EX, EY, NUYX
      DOUBLE PRECISION:: E1, E2, G12, NU12, GF, NU21
      DOUBLE PRECISION:: E1F, E2F, Em, NUm, NUf, VF
      DOUBLE PRECISION:: EPSILONX, EA, EB

C     MATERIAL CONSTANTS DEFINED IN ABAQUS
      E1F = PROPS(1)
      E2F = PROPS(2)
      Em  = PROPS(3)
      NUm = PROPS(4)
      NUf = PROPS(5)
      VF  = PROPS(6)

C     PRONY SERIES COEFFICIENTS
      k1  = 0.02475
      k2  = 0.06539
      k3  = 0.0845
      k4  = 0.03712
      k5  = 0.05312
      k6  = 0.03103
      k7  = 0.02424
      k8  = 0.09984
      k9  = 0.1
      k10 = 0.1
      k11 = 0.1
      k12 = 0.1
      k13 = 0.09999
      k14 = 0.03029
```

```
      t1  = 18.9
      t2  = 100
      t3  = 1000
      t4  = 2.00E+04
      t5  = 1.00E+05
      t6  = 1.95E+06
      t7  = 1.77E+07
      t8  = 1.74E+08
      t9  = 1.38E+09
      t10 = 1.00E+10
      t11 = 1.00E+11
      t12 = 1.00E+12
      t13 = 1.00E+13
      t14 = 1.00E+14

      b1  = k1*(1-EXP(-TIME(1)/t1))
      b2  = k2*(1-EXP(-TIME(1)/t2))
      b3  = k3*(1-EXP(-TIME(1)/t3))
      b4  = k4*(1-EXP(-TIME(1)/t4))
      b5  = k5*(1-EXP(-TIME(1)/t5))
      b6  = k6*(1-EXP(-TIME(1)/t6))
      b7  = k7*(1-EXP(-TIME(1)/t7))
      b8  = k8*(1-EXP(-TIME(1)/t8))
      b9  = k9*(1-EXP(-TIME(1)/t8))
      b10 = k10*(1-EXP(-TIME(1)/t10))
      b11 = k11*(1-EXP(-TIME(1)/t11))
      b12 = k12*(1-EXP(-TIME(1)/t12))
      b13 = k13*(1-EXP(-TIME(1)/t13))
      b14 = k14*(1-EXP(-TIME(1)/t14))

C     TIME-DEPENDENT MATERIAL PROPERTIES CALCULATION

      EMT  = EM-EM*(b1+b2+b3+b4+b5+b6+b7+b8+b9+b10+b11+b12+b13+b14)
      GMT  = EMT/(2*(1+NUm))
      GF   = E1F/(2*(1+NUf))
      E1   = 0.5*VF*(E1F+E2F)+EMT*(1-VF)
      E2   = E1
      G12  = GMT/(1-sqrt(VF)*(1-GMT/GF))
      NU12 = (1-VF)*NUm+VF*NUf
      NU21 = NU12*(E2/E1)

C     UPDATE LOCAL STRAINS

      DO I = 1,3
         E(I) = STRAN(I)+DSTRAN(I)
      END DO

C     UPDATE JACOBIAN

      DO i = 1,NTENS
         DO j = 1,NTENS
            DDSDDE(i,j) = 0.0
         END DO
      END DO

      DDSDDE(1,1) = E1/(1-NU12*NU21)
      DDSDDE(1,2) = E2*NU12/(1-NU12*NU21)
      DDSDDE(1,3) = 0D0
```

```
      DDSDDE(2,1) = DDSDDE(1,2)
      DDSDDE(2,2) = E2/(1-NU12*NU21)
      DDSDDE(2,3) = 0D0
      DDSDDE(3,1) = 0D0
      DDSDDE(3,2) = 0D0
      DDSDDE(3,3) = G12

C     UPDATE LOCAL STRESSES

      DO I=1,3
        STRESS(I)=0D0
         DO J=1,3
         STRESS(I)=STRESS(I)+DDSDDE(I,J)*(STRAN(J)+DSTRAN(J))
         END DO
      END DO

      sigmaE(1) = E(1)*DDSDDE(1,1)+E(2)*DDSDDE(1,2)
      sigmaE(2) = E(1)*DDSDDE(2,1)+E(2)*DDSDDE(2,2)
      sigmaE(3) = E(3)*DDSDDE(3,3)

C     GLOBAL COORDINATE STRESS AND STRAIN ANALYSIS

      SIGMAX  = (sigmaE(1)/2)+(sigmaE(2)/2)-sigmaE(3)
      SIGMAY  = (sigmaE(1)/2)+(sigmaE(2)/2)+sigmaE(3)
      SIGMAXY = (sigmaE(1)/2)-(sigmaE(2)/2)

      EPSILONX = (epsilonE(1)/2)+(epsilonE(2)/2)-(epsilonE(3)/2)

      ENERGY = 0.5*SIGMAX*EPSILONX

C     STATE DEPENDENT VARIABLES

      STATEV(1)   = sigmaE(1)
      STATEV(2)   = sigmaE(2)
      STATEV(3)   = sigmaE(3)
      STATEV(4)   = epsilonE(1)
      STATEV(5)   = epsilonE(2)
      STATEV(6)   = epsilonE(3)
      STATEV(7)   = EMT
      STATEV(8)   = GMT
      STATEV(9)   = E1
      STATEV(10)  = E2
      STATEV(11)  = G12
      STATEV(12)  = NU12
      STATEV(13)  = SIGMAX
      STATEV(14)  = SIGMAY
      STATEV(15)  = SIGMAXY
      STATEV(16)  = EPSILONX
      STATEV(17)  = ENERGY

      RETURN
      END
```

REFERENCES

Adams, D. S. and Mobrem, M., 2009, "Lenticular Jointed Antenna Deployment Anomaly and Resolution Onboard the Mars Express Spacecraft," *Journal of Spacecraft and Rockets*, Vol. 46, No. 2, March – April 2009, pp. 403 – 410.

Aridon, G., Blanchard, L., Allezy, A., Rémond, D., and Dufour, R., 2008, "On the Correction Capability of a Deployed Tape-Spring Hexapod," *Mechanism and Machine Theory*, 43(8), pp. 1009 – 1023.

ASTM Committee D-30 on Composite Materials, 2008, "Standard Test Method for Tensile Properties of Polymer Matrix Composite Materials," *ASTM International*.

ASTM D3171 – 15, 2011, "Standard Test Methods for Constituent Content of Composite Materials," *ASTM International*.

ASTM D3518/D 3518M-94, 2001, "Standard Test Method of In-Plane Shear Response of Polymer Matrix Composite Materials by Tensile Test of a ± 45 Laminate," *ASTM International*.

Autodesk Simulation Composite Design, 2014, Software Package, Ver. 2014, Autodesk, Inc., San Francisco, CA.

Barbera, D. and Laurenzi, S., 2015, "Nonlinear Buckling and Folding Analysis of a Storable Tubular Ultrathin Boom for Nanosatellites," *Composite Structures*, 132, pp. 226 – 238.

Black, J. T., Whetzal, J. A., deBlonk, B. J., and Massarello, J. J., 2006, "Deployment Repeatability Testing of Composite Tape Springs for Space Optics Applications," *47th AIAA/ASME/ASCE/AHS/ASC Structures, Structural Dynamics, and Materials Conference*, 1 – 4 May 2006, Newport, RI, pp. 1 – 15.

Boesch, C., Pereira, C., John, R., Schmidt, T., Seifart, K., Sparr, H., Lautier, J. M., and Pyttel, T., 2008, "Ultra Light Self-Motorized Mechanism for Deployment of Light Weight Spacecraft Appendages," *Proceedings of the 39th Aerospace Mechanisms Symposium*, NASA Marshall Space Flight Center, 7 – 9 May 2008, pp. 221 – 234.

Borowski, E., Khan, A., and Reda Taha, M. M., 2016, "Identifying Critical Design Variables and Domains for Design Optimization of Deployable Tape Springs for Controlled Deployment," *American Society for Composites 31st Technical Conference Proceedings*, Williamsburg, VA, pp. 1 – 10.

Brinkmeyer, A., Pellegrino, S., and Weave, P. M., 2016, "Effects of Long-Term Stowage on the Deployment of Bistable Tape Springs," *Journal of Applied Mechanics*, Vol. 83, No. 1, pp. 1 – 11.

Chopra, A. K., 2012, "Dynamics of Structures: Theory and Application to Earthquake Engineering (Fourth Edition)," Boston, MA: Prentice Hall.

Daton-Lovett, A., 1996, "An Extendible Member," *Patent Cooperation Treaty Application*, PCT/GB97/00839.

Dewalque, F., Collette, J. P., and Bruls, O., 2016, "Mechanical Behavior of Tape Springs Used in the Deployment of Reflectors around a Solar Panel," *Acta Astronautica*, Vol. 123, pp. 271 – 282.

Findley, W. N., Lai, J. S., and Onaran, K., 1976, "Creep and Relaxation of Nonlinear Viscoelastic Materials," Volume 18, Amsterdam: North-Holland Publishing Company.

Galletly, D. A., and Guest S. D., 2000, "Equilibrium and Stability Analysis of Composite Slit Tubes," *IASS-IACM Fourth International Colloquium on Computation of Shell & Spatial Structures*, Crete, Greece, pp. 1 – 18.

Garner, A., Khan, A. I., and Reda Taha, M. M., 2015, "Effect of MWCNTs on Creep of Epoxy for CFRP Deployable Composites," *American Society of Composite Technical Conference*, Michigan State University, East Lansing, MI, pp. 1 – 12.

Guest, S. D., and Pellegrino, S., 2006, "Analytical Models for Bistable Cylindrical Shells," *Proceedings of the Royal Society*, Vol. 462, No. 2067, pp. 839 – 854.

Haj-Ali, R. M., and Muliana, A. H., 2008, "A Micro-to-Meso Sublaminate Model for the Viscoelastic Analysis of Thick-Section Multi-Layered FRP Composite Structures," *Mechanics of Time-Dependent Materials*, Vol. 12, No. 1, pp. 69 – 93.

Herbeck, L., Eiden, M., Leipold, M., Sickinger, C., and Unckenbold, W., 2001, "Development and test of Deployable Ultra-Lightweight CFRP-Booms for a Solar Sail," *Spacecraft Structures, Material and Mechanical Testing*, Vol. 468, pp .107 – 112.

Hilton, H. H., and Yi, S., 1998, "The Significance of (An) Isotropic Viscoelastic Poisson Ratio Stress and Time Dependencies," *International Journal of Solids and Structures*, 35(23), pp. 3081 – 3095.

Hexcel. (2014, February 1). *HexTow IM7 Carbon Fiber* [Material Datasheet]. Retrieved from http://www.hexcel.com/Products/Carbon-Fiber/HexTow-Continuous-Carbon-Fiber www.hexcel.com/resources/datasheets/carbon-fiber-data-sheets/im7.pdf.

Hui, Y., Zongquan, D., Rongqiang, L., Yan, W., and Hongwei, G., 2014, "Optimizing the Quasi-Static Folding and Deploying of Thin-Walled Tube Flexure Hinges with Double Slots," *Chinese Journal of Mechanical Engineering*, Vol. 27, No. 2, pp. 279 – 286.

Hyer, M. W., 2009, *Stress Analysis of Fiber Reinforced Composite Materials*, DEStech Publications, Inc.

Iqbal, K., and Pellegrino, S., 2000, "Bi-Stable Composite Shells," *American Institute for Aeronautics and Astronautics*, pp. 1 – 8.

Irisarri, F. X., and Le Riche, R., 2014, "Multiscale Composite Optimization with Design Guidelines," *Journée d'étude: Optimisation des Composites*.

Jeon, S. K., and Murphey, T. W., 2011, "Design and Analysis of a Meter-Class CubeSat Boom with a Motor-Less Deployment by Bi-Stable Tape Springs," *52nd AIAA/ASME/ASCE/AHS/ASC Structures, Structural Dynamics and Materials Conference*, 4 – 7 April 2011, Denver, Colorado, pp. 1 – 11.

Keil, T. J., and Banik, J. A., 2011, "Stowage and Deployment Strength of a Rollable Composite Shell Reflector," *52nd AIAA/ASME/ASCE/AHS/ASC Structures, Structural Dynamics and Materials conference*, 4 – 7 April 2011, Denver, CO, pp. 1 – 12.

Khan, A., Borowski, E., and Reda Taha, M. M., 2016, "Dynamic Deployment of Composite Tape Springs," *American Society for Composites Technical Conference Proceedings*, Williamsburg, VA, pp. 1 – 9.

Khan, A., Borowski, E., Soliman, E., and Reda Taha, M. M., 2015, "Viscoelastic Energy Dissipation of Deployable Composite Structures," *Proceedings of the 10th International Conference on Composite Science and Technology*, Lisbon, Portugal, pp. 1 – 10.

Khan, A. I., Borowski, E., Soliman, E., and Reda Taha, M. M., 2017, "Examining Energy Dissipation of Deployable Aerospace Composites Using Matrix Viscoelasticity," *ASCE Journal of Aerospace Engineering*, In Press.

Kim, Y. K., and White, S. R., 1996, "Stress Relaxation Behavior of 3501-6 Epoxy Resin During Cure," *Polymer Engineering & Science*, Vol. 36, No. 23, pp. 2852 – 2862.

Kwok, K., 2012, *Mechanics of Viscoelastic Thin-Walled Structures*, Doctoral dissertation, California Institute of Technology, pp. 1 – 172.

Kwok, K., and Pellegrino, S., 2010, "Shape Recovery of Viscoelastic Deployable Structures," *51st AIAA/ASME/ASCE/AHS/ASC Structures, Structural Dynamics, and Materials Conference 18th AIAA/ASME/AHS Adaptive Structures Conference*, pp. 1 – 17.

Kwok, K., and Pellegrino, S., 2012, "Micromechanical Modeling of Deployment and Shape Recovery of Thin-Walled Viscoelastic Composite Space Structures," *53rd AIAA/ASME/ASCE/AHS/ASC Structures, Structural Dynamics and Materials Conference 10th AIAA/ASME/AHS Adaptive Structures Conference*, pp. 1 – 16.

Kwok, K., and Pellegrino, S., 2013, "Folding, Stowage, and Deployment of Viscoelastic Tape Springs," *AIAA Journal*, Vol. 51, No. 8, pp. 1908 – 1918.

Kwok, K., and Pellegrino, S., 2017, "Micromechanics Models for Viscoelastic Plain-Weave Composite Tape Springs," *AIAA Journal*, Vol. 55, No. 1, pp. 309 – 321.

Mallikarachchi, H. M. Y. C., and Pellegrino, S., 2008, "Simulation of Quasi-Static Folding and Deployment of Ultra-Thin Composite Structures," *Proceedings of 49th AIAA/ASME/ASCE/AHS/ASC Structures, Structural Dynamics, and Materials Conference, Schaumburg, Illinois*, pp. 1 – 15.

Mallikarachchi, H. M. Y. C., and Pellegrino, S., 2009, "Deployment Dynamics of Composite Booms with Integral Slotted Hinges," *50th AIAA/ASME/ASCE/ASC Structures, Structural Dynamics, and Materials Conference, Boston*, pp. 1 – 16.

Mallikarachchi, H. M. Y. C., and Pellegrino, S., 2011a, "Folding and Deployment of Ultra-Thick Composite Structures," *Proceedings of International Scientific Conference on Advanced Lightweight Structures and Reflector Antennas, Institute of Construction, Special Systems and Engineering Maintenance of the Georgian Technical University*, pp. 48 – 57.

Mallikarachchi, H. M. Y. C., and Pellegrino, S., 2011b, "Design and Validation of Thin-Walled Composite Deployable Booms with Tape-Spring Hinges," *52nd AIAA/ASME/ASCE/AHS/ASC Structures, Structural Dynamics and Materials Conference*, Vol. 2019, pp. 1 – 18.

Mallikarachchi, H. M. Y. C., and Pellegrino, S., 2011c, "Quasi-Static Folding and Deployment of Ultrathin Composite Tape-Spring Hinges," *Journal of Spacecraft and Rockets*, Vol. 48, No. 1, pp. 187 – 198.

Mallikarachchi, H. M. Y. C., and Pellegrino, S., 2014a, "Deployment Dynamics of Ultrathin Composite Booms with Tape-Spring Hinges," *Journal of Spacecraft and Rockets*, Vol. 51, No. 2, pp. 604 – 613.

Mallikarachchi, H. M. Y. C., and Pellegrino, S., 2014b, "Design of Ultrathin Composite Self-Deployable Booms," *Journal of Spacecraft and Rockets*, Vol. 51, No. 6, pp. 1811 – 1821.

Maqueda, I., Pellegrino, S., and Mejia-Ariza, J. M., 2012, "Characterization of a High Strain Composite Material," *53rd AIAA Structures, Structural Dynamics, and Materials Conference*, pp. 1 – 12.

Meyers, M. A., and Chawla, K. K., 2009, "Mechanical Behavior of Materials," Cambridge University Press, Cambridge, UK.

Mobrem, M., and Adams, D. S., 2009, "Deployment Analysis of Lenticular Jointed Antennas Onboard the Mars Express Spacecraft," *Journal of Spacecraft and Rockets*, Vol. 46, No. 2, pp. 394 – 402.

Murphey, T. W., 2009, "Large Strain Composite Materials in Deployable Space Structures," *17th International Conference on Composite Materials*, Vol. 28, Edinburgh, UK: The British Composite Soc., pp. 1 – 15.

Murphey, T. W., Jeon, S., Biskner, A., and Sanford, G., 2010, "Deployable Booms and Antennas Using Bi-Stable Tape-Springs," *24th Annual AIAA/USU Conference on Small Satellites*, pp. 1 – 7.

Murphey, T. W., and Pellegrino, S., 2004, "A Novel Actuated Composite Tape-Spring for Deployable Structures," *Proceedings of the 45th AIAA/ASME/ASCE/AHS/ASC Structures, Structural Dynamics & Materials Conference, Reston, Virginia*, pp. 1 – 11.

Patz Materials & Technologies. (2014, April 10). *PMT-F7* [Material Datasheet]. Retrieved from http://patzmandt.com/prepregs/advanced_composite_prepregs patzmandt.com/ yahoo_site_admin/assets/docs/PMT-F7_Rev2.152215524.pdf.

Peterson, M. E., and Murphey, T. W., 2013, "Large Deformation Bending of Thin Composite Tape Spring Laminates," *54th AIAA/ASME/ASCE/AHS/ASC Structures, Structural Dynamics, and Materials Conference*, pp. 1 – 15.

Pollard, E. L., and Murphey, T. W., 2006, "Development of Deployable Elastic Composite Shape Memory Alloy Reinforced (DECSMAR) Structures," *47th AIAA/ASME/ASCE/AHS/ASC Structures, Structural Dynamics, and Materials Conference*, pp. 1 – 19.

Pollard, E. L., Murphey, T. W., and Sanford, G. E., 2007, "Experimental and Numerical Identification of a Monolithic Articulated Concentrated Strain Elastic Structure's (MACSES's) Properties," *48th AIAA/ASME/ASCE/AHS/ASC Structures, Structural Dynamics, and Materials Conference*, Honolulu, HI.

Prigent, Y., Mallol, P., and Tibert, G., 2011, "A Classical Lamination Model of Bi-Stable Woven Composite Tape-Springs," *NSCM-24, Helsinki, Finland, 3-4 November 2011*, Department of Civil and Structural Engineering, Aalto University, pp. 1 – 4.

Rimrott, F. P. J., 1966, "Storable Tubular Extendible Members," *Engineering Digest*, September.

Sakovsky, M., Pellegrino, S., and Mallikarachchi, H. M. Y. C., 2016, "Folding and Deployment of Closed Cross-Section Dual-Matrix Composite Booms," *3rd AIAA Spacecraft Structures Conference*," pp. 1 – 18.

Sanford, G., Biskner, A., and Murphey, T., 2010, "Large Strain Behavior of Thin Unidirectional Composite Flexures," *51st AIAA/ASME/ASCE/AHS/ASC Structures, Structural Dynamics, and Materials Conference*, pp. 1 – 15.

Seffen, K. A., 2001, "On the Behavior of Folded Tape-Springs," *ASME Journal of Applied Mechanics,* Vol. 68(3), pp. 369 – 375.

Seffen, K. A., and Pellegrino, S., 1999, "Deployment Dynamics of Tape Springs," *Proceedings of the Royal Society of London A: Mathematical, Physical and Engineering Sciences,* Vol. 455, No. 1983, pp. 1003 – 1048.

Seffen, K. A., You, Z., and Pellegrino, S., 2000, "Folding and Deployment of Curved Tape Springs," *International Journal of Mechanical Sciences,* Vol. 42, No. 10, pp. 2055 – 2073.

Simulia, Dassault Systems, 2014, "Abaqus 6.14 Documentation," *Providence, RI, US.*

Soykasap, O., 2009, "Deployment Analysis of a Self-Deployable Composite Boom," *Composite Structures,* Vol. 89, No. 3, pp. 374 – 381.

Soykasap, O., 2011, "Analysis of Plain-Weave Composites," Mechanics of Composite Materials, Vol. 47, No. 2, pp. 161 – 176.

Tymrak, B. M., Kreiger, M., and Pearce, J. M., 2014, "Mechanical Properties of Components Fabricated with Open-Source 3-D Printers Under Realistic Environmental Conditions," *Materials and Design*, Vol. 58, pp. 242 – 246.

Yang, H., Liu, R., Wang, Y., Deng, Z., and Guo, H., 2015, "Experimental and Multiobjective Optimization Design of Tape-Spring Hinges," *Structural and Multidisciplinary Optimization,* Vol. 51, No. 6, pp. 1373 – 1384.

Yee, J. C. H., and Pellegrino, S., 2003, "Foldable Composite Structures," *Proceedings of IASSAPCS*, pp. 1 – 12.

Yee, J. C. H., and Pellegrino, S., 2005, "Folding of Woven Composite Structures," *Composites Part A: Applied Science and Manufacturing*, Vol. 36, No. 2, pp. 273 – 278.

Yee, J. C. H., Soykasap, O., and Pellegrino, S., 2004, "Carbon Fibre Reinforced Plastic Tape Springs," *45th AIAA/ASME/ASCE/AHS/ASC Structures, Structural Dynamics, and Materials Conference,* pp. 1 – 9.

Younes, R., Hallal, A., Fardoun, F., and Chehade, F. H., 2012, "Comparative Review Study on Elastic Properties Modeling for Unidirectional Composite Materials," *Composites and Their Properties*, pp. 391 – 408.